UNIVERSIDAD POLITÉCNICA DE CARTAGENA

Dpto. Electrónica, Tecnología de Computadoras y Proyectos.

PhD Thesis

Study of new vector-control algorithms for 3-phase inverters used in renewable agents connected to the low-voltage utility grid with disturbances

Néstor Francisco Guerrero Rodríguez

October 2014

UNIVERSIDAD POLITÉCNICA DE CARTAGENA

Dpto. Electrónica, Tecnología de Computadoras y Proyectos.

PhD Thesis

Study of new vector-control algorithms for 3-phase inverters used in renewable agents connected to the low-voltage utility grid with disturbances

Néstor Francisco Guerrero Rodríguez

Supervisor:

Dr. Alexis Bonifacio Rey Boué

October 2014

Universidad
Politécnica
de Cartagena

CONFORMIDAD DE SOLICITUD DEAUTORIZACIÓN DE DEPÓSITO DE TESIS DOCTORAL POR EL/LA DIRECTOR/A DE LA TESIS

D./Dª. **Dr. Alexis Bonifacio Rey Boué** Director/a de la Tesis doctoral **Study of new vector-control algorithms for 3-phase inverters used in renewable agents connected to the low-voltage utility grid with disturbances.**

INFORMA:

Que la referida Tesis Doctoral, ha sido realizada por D/Dª. **Néstor Francisco Guerrero Rodríguez**, dentro del programa de doctorado **Energías Renovables**, dando mi conformidad para que sea presentada ante la Comisión de Doctorado para ser autorizado su depósito.

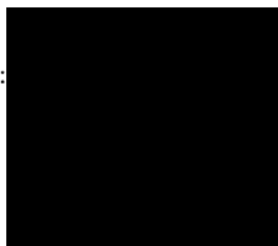La rama de conocimiento en la que esta tesis ha sido desarrollada es:

- ☐ Ciencias
- ☐ Ciencias Sociales y Jurídicas
- ☒ Ingeniería y Arquitectura

En Cartagena, a 09 de Julio de 2014

EL/LA DIRECTOR/A DE LA TESIS

Dr. Alexis Bonifacio Rey Boué

Fdo.:

COMISION DE DOCTORADO

CONFORMIDAD DE DEPÓSITO DE TESIS DOCTORAL
POR LA COMISIÓN ACADÉMICA DEL PROGRAMA

D/Dª. Dr. **Antonio Urbina Yeregui**, Presidente/a de la Comisión Académica del Programa de **Energías Renovables.**

INFORMA:

Que la Tesis Doctoral titulada, "**Study of new vector-control algorithms for 3-phase inverters used in renewable agents connected to the low-voltage utility grid with disturbances**", ha sido realizada, dentro del mencionado programa de doctorado, por D/Dª. **Néstor Francisco Guerrero Rodríguez**, bajo la dirección y supervisión del Dr/ Dra. **Alexis Bonifacio Rey Boué.**

En reunión de la Comisión Académica de fecha 10 de Junio de 2014, visto que en la misma se acreditan los indicios de calidad correspondientes y la autorización del Director de la misma, se acordó dar la conformidad, con la finalidad de que sea autorizado su depósito por la Comisión de Doctorado.

La Rama de conocimiento por la que esta tesis ha sido desarrollada es:

☐Ciencias
☐Ciencias Sociales y Jurídicas
☒Ingeniería y Arquitectura

En Cartagena, a 09 de Julio de 2014

EL PRESIDENTE DE LA COMISIÓN ACADÉMICA DEL PROGRAMA

Fdo: Dr. Antonio Urbina Yeregui

COMISIÓN DE DOCTORADO

Acknowledgements

Firstly, I would like to acknowledge to the Santander bank and the Universidad Politécnica de Cartagena for giving me the opportunity to realize my PhD studies through a scholarship. Greatly I appreciate the dedication and persistence shown by my supervisor Dr. Alexis Bonifacio Rey Boué who was marking step by step the guidelines to carry out this work and for being a great source of knowledge. I appreciate the assistance provided by the lab technicians Manolo and David and the staff of the Department of Electronics, Computers Technology and Projects (DETCP), especially to Mamen. Greatly I appreciate the professors of the Renewable Energy Master and notably to Antonio Urbina. I give thanks to my colleagues Gino, Paco, Fran Clemente and Lucia for making this work more pleasant. Thank to my Dominican colleagues Wilfredo, Faxas, Kadafis, Franklin, Wilson, Genris, Francisco Ramirez and Francisco Sanchez that together we have crossed an ocean for the purpose of obtaining further academic background and after five years we continue together as the first day.

During the course of this Thesis I have been involved with a large number of people that I have done collaborations and I cannot avoid mentioning some of them as in the case of Vasilis Kleftakis, Alexandros Rigas, Santiago de Pablo Gómez, Luis Carlos Herrero de Lucas and Fernando Martinez.

I am immensely grateful to my parents who despite the distance they have always been close to me; thank you very much. Thank brother, cousins, thanks to my grandparents, to my uncles and finally to my friends Oliver, Luis, Joel and Enyer.

I am especially grateful to Rocío Murcia for being my pillar of support to carry out this work and to be the most special person in my life.

Agradecimientos

Primeramente quiero agradecer a la Universidad Politécnica de Cartagena UPCT y al banco Santander por darme la oportunidad de realizar mis estudios de doctorado a través de una beca pre-doctoral.

Agradezco infinitamente la dedicación y el empeño mostrado por mi director de tesis para que este trabajo pudiera seguir adelante marcando paso a paso las estrategias a seguir y por ser para mí la mayor fuente de conocimiento. Gracias Alexis Bonifacio Rey Boué.

Aprecio en gran medida la asistencia ofrecida por el personal del departamento de Electrónica, Tecnología de Computadoras y Proyectos en especial a Mamen, Manolo y David. Felicito y agradezco al cuerpo de profesores del Máster de Energías renovables por el trabajo que están realizando y de manera especial a Antonio Urbina.

Agradezco a mis compañeros investigadores de la UPCT Gino, Paco, Lucia y Fran Clemente por haber hecho más llevadero este periodo.

A mis compañeros dominicanos Wilfredo, Faxas, Kadafis, Franklin, Wilson, Genris, Francisco Ramírez y Francisco Sánchez que juntos cruzamos un Océano para realizar nuestros estudios de posgrado y después de cinco años continuamos tan unidos como el primer día.

Durante el desarrollo de esta tesis me he estado relacionando con una gran cantidad de personas con las cuales he realizado colaboraciones de investigación y

Hay una fuerza motriz más poderosa que el vapor, la electricidad y la energía atómica: la voluntad.

Albert Einstein

Abstract

Throughout decades, the electric power demand has been rising due to the growth of the industrial sector and transportation, and the development of new technologies that require more energy together with the increase of the global population have led to a higher fuel demand needed for the electric energy generation. The global energy consumption in 2010 was 153,000 TWh and it is expected an increment to 184,600 TWh by 2020, the majority provided by fossil fuels, although the future of these trend is uncertain. Besides, greenhouse effect is causing environmental changes that concern mankind and the creation of new energetic policies is a fact.

An alternative for reducing the fossil fuel dependence and the reduction of the greenhouse gas emission is the use of clean and infinite renewable energy sources such as photovoltaic, wind, as well as fuel cells for energy storage, which have been installed in the energetic mix. In this context, new renewable agents are connected to the 3-phase utility grid and must be properly controlled according to power electrical legislations.

For this, new and sophisticated control algorithms are to be designed in order to control properly the line currents of the grid-connected inverter when variations of the nominal frequency, voltage unbalances and low-order harmonics are present in the 3-phase utility grid voltage.

This thesis is focused in the study of several control and synchronization algorithms used in grid-connected Voltage Source Inverters (VSI) working as the power conditioner circuits for renewable energy systems. The study of these

algorithms is carried out using a grid-connected photovoltaic system, but they can be extended to any renewable agent in any distributed generation system.

Resumen

La demanda de energía eléctrica se ha ido incrementando a través de los años debido al desarrollo que han tenido el sector industrial y de transporte, sumándose además el aumento de la población mundial y el desarrollo de nuevas tecnologías que requieren mayor cantidad de energía. Por ello, y con el propósito de generar la energía eléctrica necesaria para suplir a estos sectores, el consumo de combustible ha presentado un aumento significativo. Así, la energía consumida en el año 2010 fue de unos 153,000 TWh y se prevé que para el año 2020 esta cifra ascienda a 184,000 TWh, siendo la mayor parte de esta energía proveniente de combustibles fósiles, aunque el futuro de esta tendencia es incierto. Además, la población mundial se está concienciando cada vez más de los efectos negativos medioambientales que está provocando el llamado "efecto invernadero" y, como consecuencia, se están creando una serie de políticas energéticas con el fin de reducir la generación de gases y partículas contaminantes.

Una alternativa para reducir la dependencia de los combustibles fósiles y, a la vez, reducir las emisiones de los gases tóxicos causantes del efecto invernadero, es el uso de fuentes de energías renovables como la solar fotovoltaica y la eólica, así como el uso de pilas de combustibles para almacenamiento de energía, todas ellas a instalar en el mix energético. En este sentido, los nuevos agentes renovables que se conecten a la red eléctrica trifásica de baja tensión deben controlarse adecuadamente y cumpliendo con las legislaciones energéticas vigentes.

En este sentido, deben diseñarse nuevas y sofisticadas estrategias de control con el propósito de controlar adecuadamente las corrientes de línea de los inversores de

conexión a red utilizados en los agentes renovables cuando existan perturbaciones en la red eléctrica de baja tensión, tales como las variaciones de su frecuencia nominal, los desequilibrios en las tensiones trifásicas y la presencia de contaminación armónica de baja frecuencia.

Por todo lo anteriormente mencionado, esta tesis está enfocada en el estudio de varios algoritmos de control y sincronización utilizados en inversores en fuente de tensión (VSI) para conexión a red que operan como los acondicionadores de potencia para los sistemas renovables. Los estudios realizados se aplican a un sistema fotovoltaico, pero pueden extenderse a cualquier tipo de agente renovable utilizado en un sistema de Generación Distribuida.

Contents

List of Figures

List of Tables

Nomenclature and Units

v_p : output voltage of the PV Generator

i_p : output current of the PV Generator

P_{PV} : power in the PV generator

v_{CC} : dc bus voltage

v^*_{CC} : dc bus voltage reference

i_{CC} : current that will be injected into the inverter

C_{link} : dc-link capacitor

i_{clink} : current through the dc-link capacitor

θ : phase of the 3-phase utility grid voltages

ω: fundamental angular frequency

d: duty cycle of the DC/DC boost converter

L_{dc} and D: inductance and diode of the DC/DC boost converter

i_{IGBT} : current through the power switch of the DC/DC boost converter

i_u, i_v, i_w : 3-phase inverter line currents

i_r, i_s, i_t : 3-phase utility grid currents

DQ : in-quadrature signals

ω' : centre angular frequency

ω : angular frequency

k : gain of the SOGI block

PI_{id}, PI_{iq}: current PI regulators

PI_V: voltage PI regulator

v_r, v_s, v_t : 3-phase utility grid voltages

s_u, s_v, s_w : states of the power-switches of the inverter

u: inverter voltage space vector

i: inverter line current space vector

u$_{AC}$: utility grid voltage space vector

L: line inductance

R: resistance of the line inductance

v_α, v_β : $\alpha\beta$ components of space vector **u**

i_α, i_β : $\alpha\beta$ components of space vector **i**

$u_{ac\alpha}, u_{ac\beta}$: $\alpha\beta$ components of space vector **u$_{AC}$**

p: instantaneous active power

q: instantaneous reactive power

i_d, i_q: d-q components of space vector i

u_{acd}, u_{acq} : d-q components of space vector **u$_{AC}$**

i^*_d, i^*_q : d-q reference components of vector **i***

q^* : instantaneous reactive power reference

F_{sw} : switching frequency

t_s : settling time

τ : time constant of the first order system

$t_{s(FLL)}$: settling time of the FLL

Γ : gain to set $t_{s(FLL)}$

Btu: British thermal unit

GW: gigawatt (1 Watt x 10^9)

GWh: gigawatt-hour

kW: kilowatt (1 Watt x 10^3)

kWh: kilowatt-hour

MW: megawatt (1 Watt x 10^6)

MWh: megawatt-hour

TW: terawatt (1 Watt x 10^{12})

TWh: terawatt-hour

CHAPTER 1
Introduction

The constant increase of the generation of electrical energy from conventional sources, such as fossil and nuclear fuels, causes a high level of pollution due to CO_2 emissions, which also produce the greenhouse effect and the recent climate change. In addition, the availability of conventional world fuel reserves is not guaranteed because they are running out. In this scenario, the concept of Distributed Generation (DG), where small electrical generators (also known as agents) based mainly on renewable energy sources, are connected to the 3-phase low-voltage utility grid in order to supply the shortage of electrical energy in the energetic mix.

1.1 Motivation

Since renewable energy sources produce dc electric quantities and the industrial and residential loads consume ac electric currents, one of the main parts of a grid-connected renewable agent is the inverter. A Voltage Source Inverters (VSI), built with semiconductor devices operating in switch-mode, is commonly used as the power conditioner unit to interface renewable resources to the utility grid in a Distributed Generation (DG) structure.

The control of the grid-connected inverters is one of the main research lines in the field of the renewable energies in order to obtain the highest efficiency of the renewable installation. So, new and sophisticated control algorithms are to be designed in order to regulate properly its line currents when some perturbations such as variations of the nominal frequency, voltage unbalances and low-order harmonics arise in the low-voltage 3-phase utility grid, and for attaining a good power quality according to international standards.

On the other hand, it is necessary an appropriated control of the power factor (PF) of the inverter-grid connection so as to regulate the needed instantaneous reactive power according to load demands, with the highest efficiency. For this, a synchronization algorithm module is needed for detecting the phase angle of the perturbed 3-phase utility grid voltages with optimal dynamic response.

For these reasons, several synchronization and control algorithms for grid-connected inverters used in photovoltaic renewable agents under some perturbations in the utility grid are studied in this thesis.

1.2 The world energy scene

Throughout decades, the global energy demand has been rising due to the growth of the industrial sector and transportation, and the development of new

2

technologies that require more energy sources together with the increase of the global population have led to a higher fuel demand needed for the electric energy generation. The global energy consumption in 2010 was 524 quadrillion British thermal units (Btu) and it is expected it will increased to 630 quadrillion of Btu by 2020 and to 820 quadrillion of Btu in 2040 [1], being the majority of this energy provided by fossil fuels as it is shown in Figure 1.1.
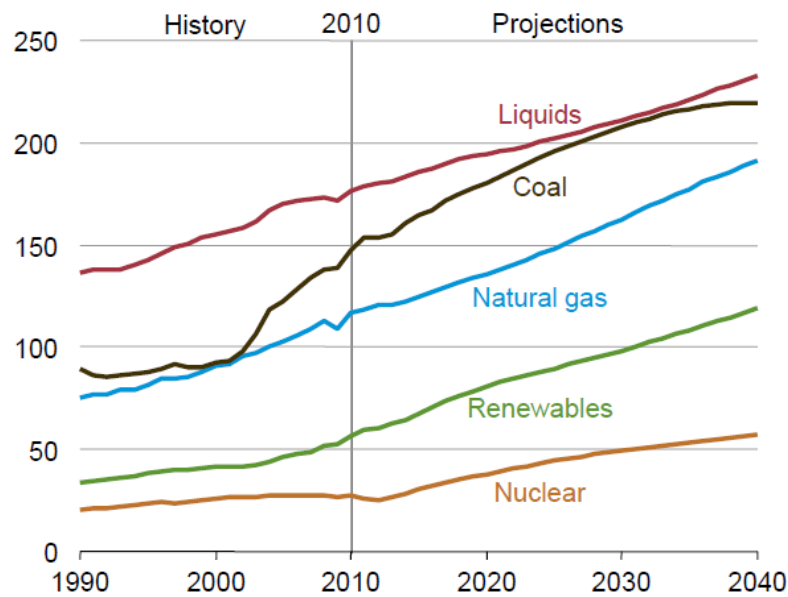
Figure 1.1. World energy consumption by fuel type, 1990-2040 (quadrillion Btu). Source: IEA (IEO2013).

However, it can be seen in the same Figure that renewable and nuclear powers are the energy sources with higher growth, having an increase of 2.5% per year, meanwhile fossil fuels will remain the largest supplier of used world energy with almost 80% in 2040: natural gas is the fossil fuel with fastest growing with a global consumption increase of 1.7% per year, meanwhile the coal use will grow faster than petroleum and other liquid fuels until 2030 [1].
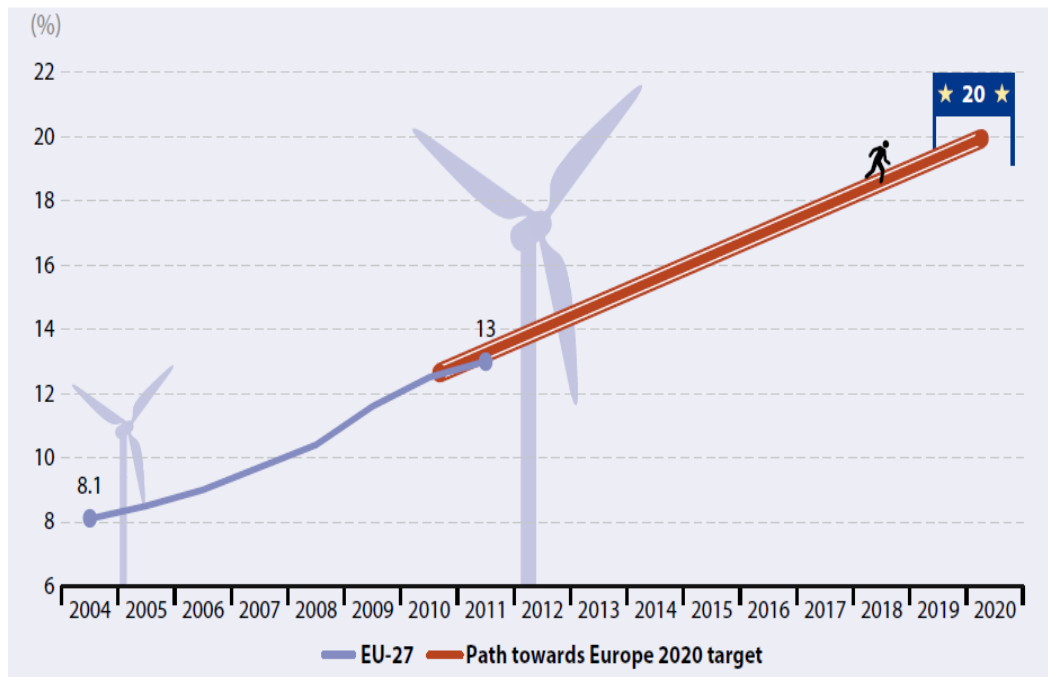
Figure 1.2. Renewable energy percentage points increase in the share of renewable in gross final energy consumption in the EU between 2004 and 2011. This favourable trend has put the EU on track to reach its 2020 target. Source: Eurostat.

Regarding to the renewable consumption in the European Union (EU), the share of renewable energy has been in continuous growth where a share of 14.1% in the gross of the final consumption was reached in 2012 representing an increasing of 4.9% compared to 2004 [2]. This increasing of the renewable consumption is due to the implementation of government subsidy policies and a decrease in the price of these technologies because they have achieved higher levels of maturity. This has led that the EU has become in the larger investor of renewable technologies. PV modules have presented the largest decrease in prices with a reduction of 76% between 2008 and 2012. In the second place are the wind turbines where a decrease in the price of 25% was presented between 2008 and 2012 [3]. Continuing with this trend, it is almost certainly that the EU will be able to fulfil its target for 2020 where a 20% of share is set for renewable energy [4] as can be observed in Figure 1.2 [2].

1.3 Global energy generation

According to the International Energy Outlook 2013 (IEO2013), the world electricity generation in 2010 was 20.2 trillion kilowatt-hours (kWh) and this figure will increased to 39.0 trillion kWh in 2040 as can be observed in Figure 1.3, which means an increase of 93% [1]. Renewable energy sources are the largest growing sources of electricity generation due to that the environmental consequences of greenhouse gas emissions is forcing to the creation of government policies to encourage the use of these renewable sources. In agreement with the IEO2013, the increasing will be of 2.8% per year from 2010 to 2040.
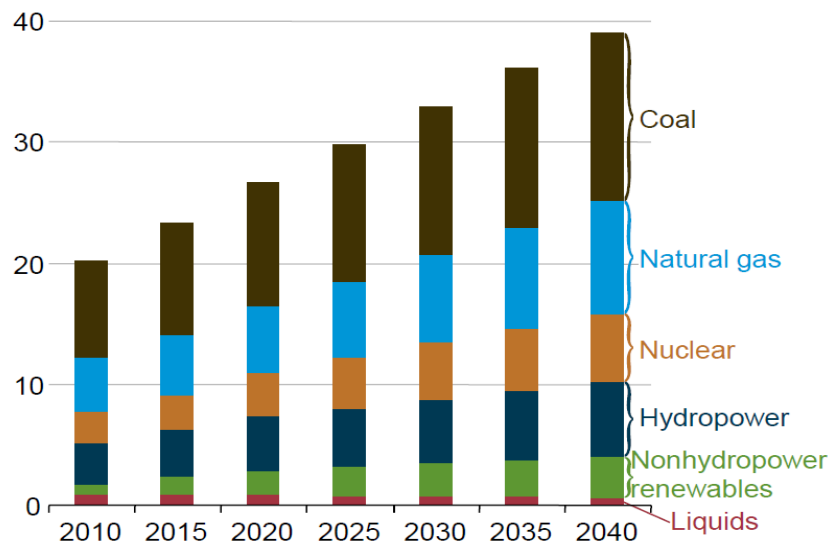
Figure 1.3. World electricity generation by energy source, 2010-2040 (trillion kilowatt-hours). Source: IEA (IEO2013).

It is expected that 80% of the electricity generation supplied by renewable energy sources will be from hydropower and wind power. In the case of the wind energy, it has a faster growing when it is compared with the past decade: the installed capacity of wind energy at the end of 2000 was 18GW reaching an installed

capacity of 183GW at the end of 2010 and is expected to continue with that trend [1].

According to IEO2013 [1], the generation from renewable energy in 2040 will be 5,400 billion kWh where 2,800 billion kWh will correspond to hydroelectric power and 1,500 billion kWh to wind (52% and 28%, respectively) as can be observed in Figure1.4.
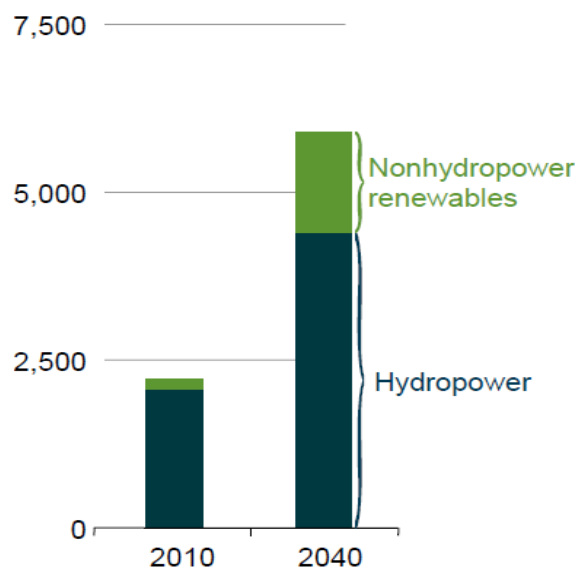
Figure 1.4. World electricity generation from renewables, 2010-2040 (billion kilowatt-hours). Source: IEA (IEO2013).

1.4 The role of renewable energy in the electricity generation

An overview of the main paths of energy available in the earth that can be used to obtain sustainable energies is presented in [5] where the main source for renewable energy is coming from the sun. As was mentioned previously, the global energy consumption in 2010 was 524 quadrillion Btu that converting to Terawatt-hours (TWh) this figure will be 153,000TWh. Dividing this quantity of energy by the number of hours in the year gives 17.46TW as the average rate of

world power consumption in 2010. As can be observed in Figure 1.5, the solar radiation intercepted by the surface of the earth is about 7,000 times the average global energy consumption of 2010, this mean that renewable energies are capable to supply all the energy needed. Energy from the sun can be used directly by thermal electric and photovoltaic, or can be used indirectly in form of wind, hydropower and biofuels [5].
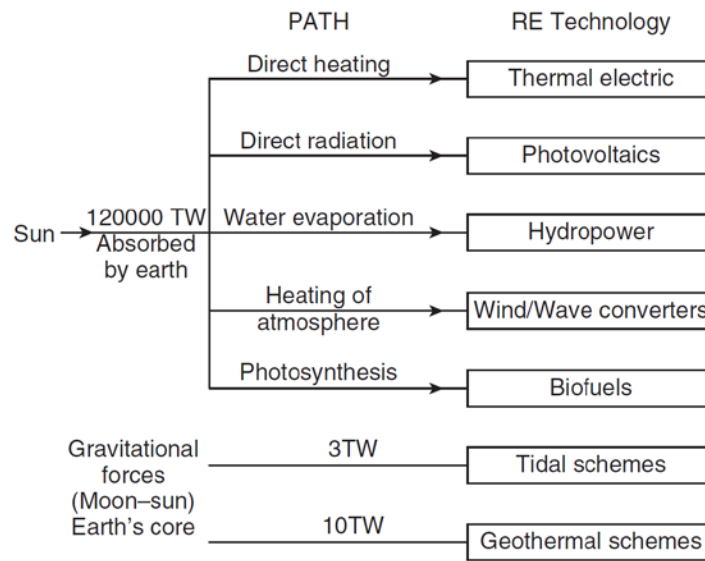
Figure 1.5. Renewable energy flow paths. Source: Renewable Energy in Power Systems book.

1.4.1 Installed Renewable energy

From 2007 to 2012 the global installed capacity of renewable energy has shown a rapid increase, being the power sector the main one [6]. According to Figure 1.6 from REN21, 19% of the global final energy consumption in 2011 was supplied by renewables. From this figure, 9.3% correspond to traditional biomass used in developing contries and 9.7% come from modern renewable energy. 4.1% of the energy from modern renewable was used in the form of thermal energy, 3.7% come from hydropower, 1.1% was provided by wind, solar, biomass, geothermal, and 0.8% was provided by biofuels [6].

In 2012 the global renewable power capacity was above 1,470GW [6], compared to 2011 this figure represents an increase of 8.5%.
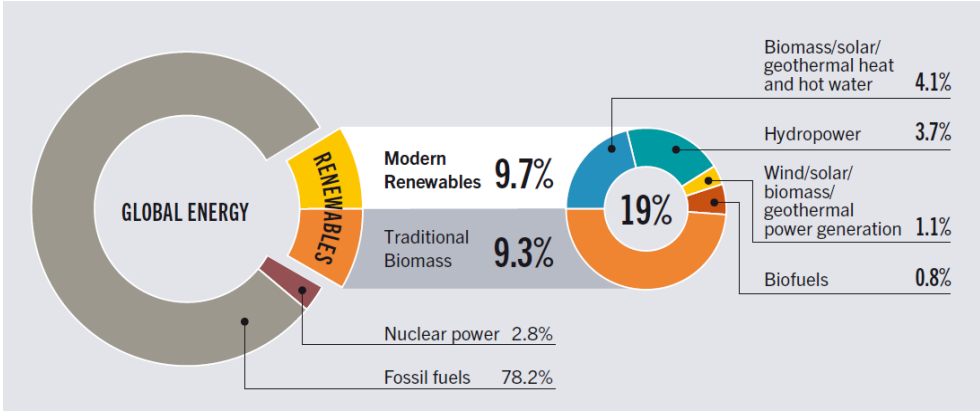
Figure 1.6. Estimated renewable energy share of global final energy consumption, 2011. Source: Renewables 2013, Global Status Report (REN21).

1.4.1.1 PV global capacity

In the particular case of photovoltaic, the total installed capacity in 2012 reached the figure of 100GW as can be observed in Figure 1.7 [6], being the main contributions from EU and Asia. In addition to subsidies, this figure of 100GW has been achieved due to the decreasing price of the PV modules and that new markets have been found as is the case of Latin America and Africa.
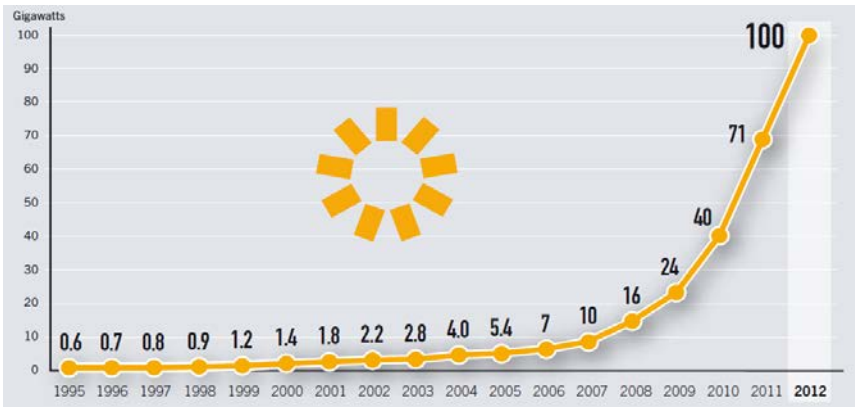
Figure 1.7. Solar PV Global Capacity, 1995–2012. Source: Renewables 2013, Global Status Report (REN21).

In 2012, several countries added more than 1GW of PV in their utility grids as it is shown in Table 1.1. Europe headed the global market where 17.7GW were installed, reaching the total capacity of almost 70GW (See Figure 1.8) [7], being Germany and Italy the leader countries with 7.6GW (reaching a total capacity of 32.4GW) and 3.3GW (reaching a total capacity of 16.4GW), respectively.
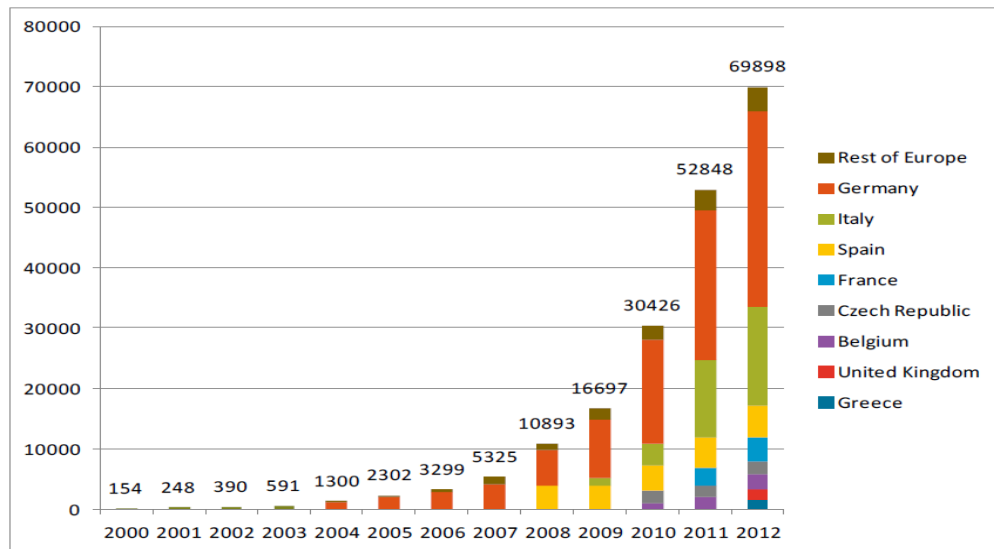
Figure 1.8. Evolution of PV capacity in EU 27 (in MWp). Source: EPIA 2013.

Table 1.1. PV installed capacity by countries in 2012.

Country	PV installed in 2012 (GW)
Germany	7.6
China	3.5
USA	3.3
Italy	3.3
Japan	1.7
France	1.1
Australia	1
India	1
UK	0.9

1.4.1.2 Hydropower global capacity

In 2012, 30GW of hydropower were installed, which means an increase of 3% reaching a global capacity of 990GW [6]. The leader country was China with 15.5GW (total capacity around 229GW). This country, together with Brazil, the United States, Canada and Russia have the 53% of the global installed capacity. See Table Table 1.2 [8] for a summary of the installed capacity in 2012 by countries.

1.4.1.3 Wind power global capacity

As can be observed in Figure 1.9, 45GW of wind power were installed in 2012 reaching the figure of 283GW [9]. China and the United States were the leader countries with almost 60% of the total power installed in this year, corresponding to 13.1GW and 13.GW, respectively. See Table 1.3 for a summary by countries [6].
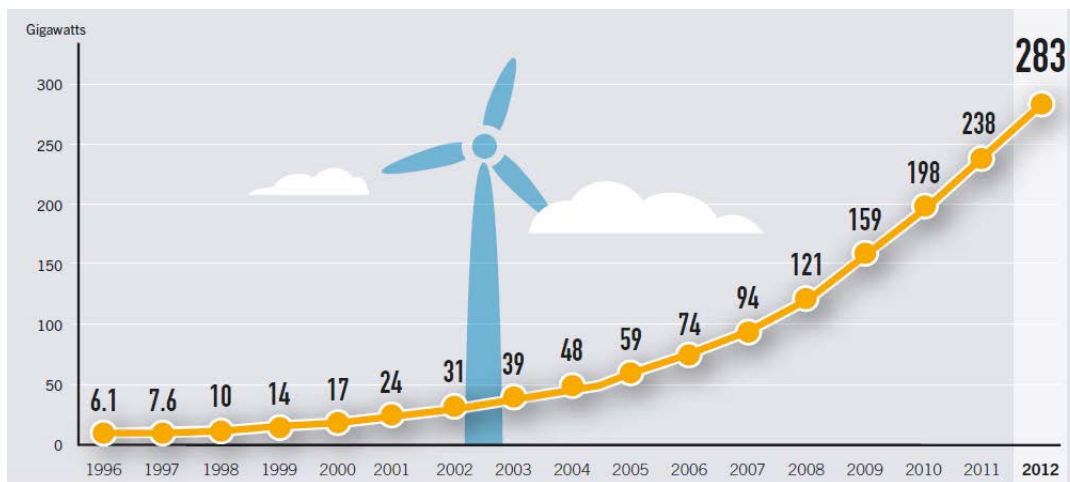
Figure 1.9. Wind Power Global Capacity, 1996–2012. Source: Renewables 2013, Global Status Report (REN21).

Table 1.2. Hydropower installed capacity by countries in 2012.

Country	Hydropower installed in 2012 (GW)
China	15.5
Turkey	2
Brazil	1.86
Vietnam	1.8
Mexico	0.75
Russia	0.33

Table 1.3. Wind power installed capacity by countries in 2012.

Country	Wind power installed in 2012 (GW)
China	13.1
USA	13
Germany	2.4
India	2.3
UK	1.9
Italy	1.3
Spain	1.1
Canada	0.9
Portugal	0.1

1.5 Analysis and discussion about the world energy scene

It is evident that the fast growth of the use of new renewable sources of energy in many countries is due to the creation of new energy policies focused on the reduction of CO_2 emissions derived from the generation of electrical energy with conventional sources such as fossil and nuclear fuels, being one of the main reasons of the climate change. These new sources of energy have been supported

by large amounts of grants for promoting the use of these new energy sources and thus fulfill the targets set in the Kyoto Protocol. It is also evident that the availability of these fuels is not guaranteed due to its world reserves are running out. For this, the mankind is raising awareness that it is mandatory the use of new sources of energy to supply the energy needs, and, in this way, the installed capacity of renewable has reached values that few decades ago were unimaginable to achieve. Nevertheless, this trend is not enough, and it is necessary to continue with the promotion of the use of these renewable sources instead.

An intelligent manner to provide the needed energy to the final customer is through the use of the Distributed Generation systems (DGs) which are composed by small producers of energy and, as a consequence, this lead to an increase of the number of grid-connected inverters which behaves as non-linear loads consuming reactive power and producing low-order harmonic pollution in the utility grid. The latter situation promotes the necessity of the creation of advanced control algorithms to overcome the non-desirable effect of these disturbances.

1.6 Methodology

MATLAB/SIMULINK [10] is used as the simulation tool on which the algorithms are developed. Inside this, SimPowerSystems Blockset contains a large number of electrical circuits, power electronic and measurement blocks, and is widely used for doing simulations.

However, a control algorithm for grid-connected renewable agents must be tested in real grid-connected platforms, which are very expensive systems. Furthermore, some of them could be fragile, and even so, it is difficult to test new control algorithms used by the inverter controller in a real operative renewable agent. It is also possible that the first algorithm versions are not fully debugged which could lead to cause faults in the renewable installation, or damages in the worst case.

In addition to this, too many laboratories are not able to do tests with a real 3-phase utility grid due to the lack of space or due to economic issues. Due to the above mentioned statements, the use of the Real-time Digital Simulation platforms [11-13], which also bring the opportunity to repeat a test under different scenarios making only small modifications and reducing the development time compared with non-real time simulations, play an important role in the experimentation for new control algorithms used in a wide variety of applications such as Power Electronics, test with Induction Machines, power flow control strategies, energy storage studies, configuration of Smart Grids, Electric Vehicles, Computer Architectures, Space Applications, Mechanical components for Automotive Industry, Wind Power Systems, among others [14,15].

Throughout this thesis, the experimental implementation of the synchronization and control algorithms for a PV grid-connected renewable agent will be done using a DS1006 DSPACE platform [13] with several I/O block, high power processing capabilities and user-friendly interconnection with SIMULINK. The model blocks of the control and power subsystems are built in MATLAB/SIMULINK and then, the C-code of the algorithms are generated with Real Time Workshop and downloaded into the DSPACE platform. The platform is formed by a host PC, the DS1006 DSPACE and the DS5202 Electric Motor HIL Solution boards with digital-to-analog and analog-to-digital converters interface, as well as an oscilloscope for waveforms monitoring. The configuration of the real time platform setup is shown in Figure 1.10 and a photo of the experiment setup is shown in Figure 1.11.

Finally, it must be pointed out that the possibility of using any other renewable agent source (wind, fuel cell, etc.) model is completely possible.
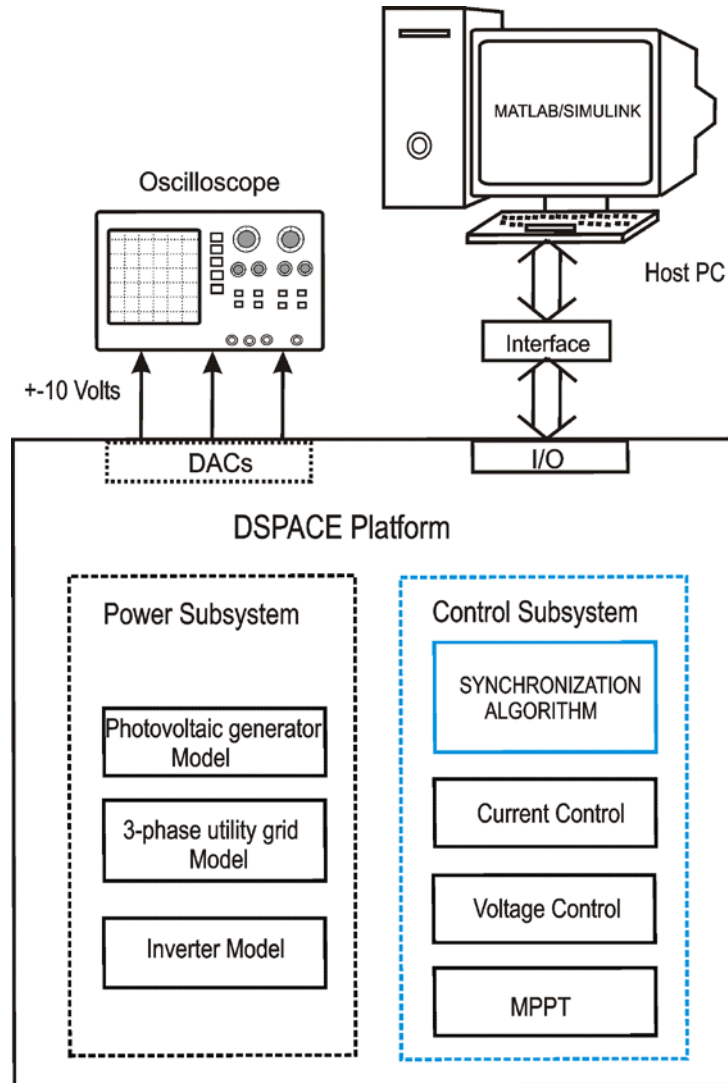
Figure 1.10. Configuration of the DSPACE platform for the real-time testing using a host PC, a DS1006 DSPACE board with a digital to analog converter interface and an oscilloscope for parameters monitoring.

Figure 1.11. Photo of the DSPACE platform for RTDS.

1.7 Aim of the thesis

The overall objective of this thesis is to make a study of several synchronization and control algorithms used in grid-connected inverters for renewable agents when the low-voltage 3-phase utility grid is affected by some disturbances, such as voltage unbalances, harmonic pollution and frequency variations.

It is intended to make an evaluation and a classification of the synchronization algorithms under the influence of the disturbances in the utility grid taking into account their capability for the optimal estimation of its phase and frequency with good dynamics, high harmonic rejection and good performance under unbalance condition. In addition, the amount of hardware resources of each algorithm is also

taken into account so as to make it possible an intelligent choice according a tradeoff between all the aspects mentioned above and the computational burden achieved for a specific figure of merit.

Finally, it is also intended to make an evaluation of the control algorithms according its capability of compensating the low-order harmonic pollution in the utility grid, as well as its capability of self-adaptation when the fundamental frequency varies from its nominal value, in order to attain a high power quality for the grid-connected renewable agent.

1.8 Thesis outline

The structure of this thesis is organized as follows:

Chapter 1 has presented a general view of the world energy scene and the contributions of the renewable energies to the electrical system.

Chapter 2 presents an overview of grid-connected renewable agents where the main components are explained and the global system is divided into the power and the control subsystems.

Chapter 3 describes several synchronization algorithms for grid-connected renewable agents where the main advantages and drawbacks of each one are studied and stated.

Chapter 4 analyzes two current control strategies for 3-phase grid-connected inverters: firstly, the well-known d-q control in the rotating synchronous reference frame (d-q axes) using PI regulators is described, and secondly, the PR controller in the stationary reference frame (αβ axes) using proportional and resonant regulators is deeply studied. Later and taking into account the PR controller structure, a harmonic compensator is also analyzed.

Chapter 5 presents, as an extension of the results obtained in Chapter 4, a new adaptive-frequency harmonic compensator.

Chapter 6 shows the conclusions, the contributions of the thesis and the future and outlooks.

CHAPTER 2
Overview of Grid-Connected Renewable Agents

This Chapter shows an overview of grid-connected renewable agents and, for the sake of simplicity, the overall system is divided into the power and the control subsystems. Nevertheless, it must be pointed out that this thesis is mainly focused in the study of the synchronization and control algorithms and so, a general description of the power subsystem is described to the reader so as to make it possible the deep comprehension of the control subsystem that will be analyzed in more detail throughout this work.

An important aspect for a grid-connected renewable agent is to control the power flow between the primary renewable energy source and the utility grid [16], as well as the power factor of the inverter-grid connection with high power quality [17].
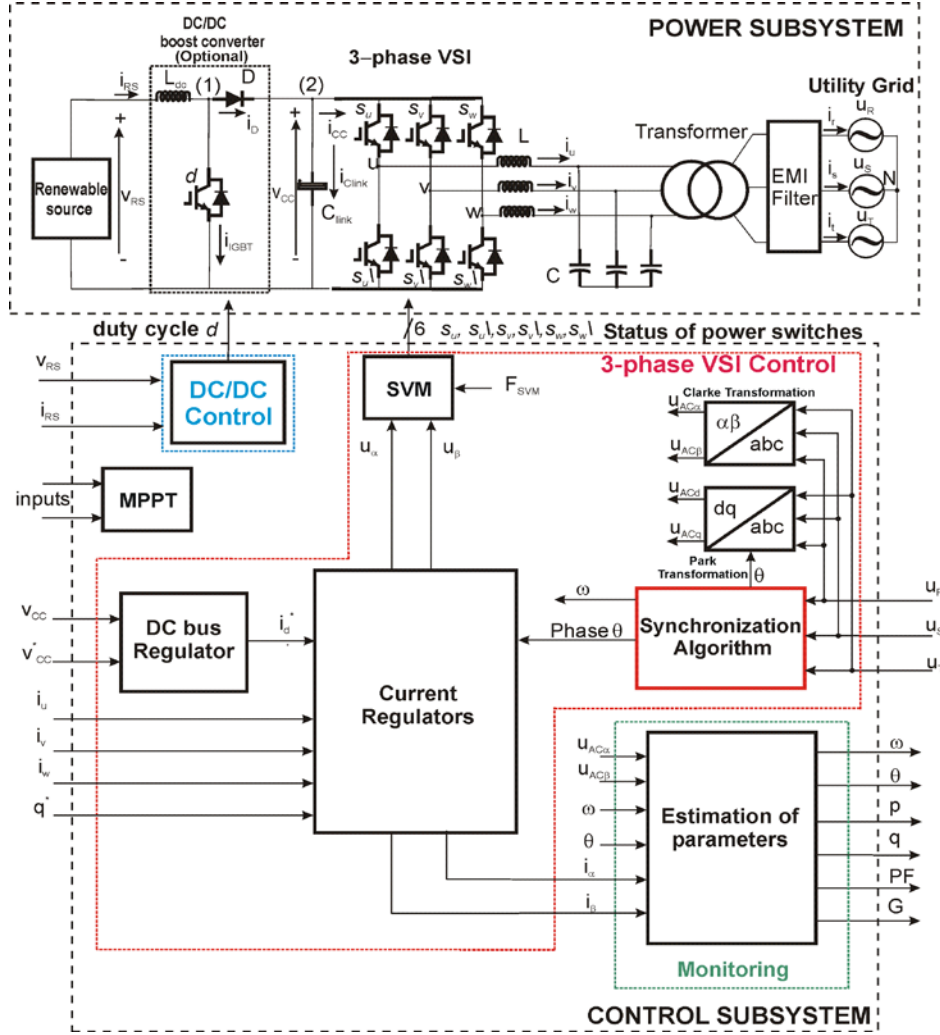
Figure 2.1. Block diagram of the Power and Control Subsystems for the 3-phase grid-connected renewable agent.

The power conditioner must guarantee the highest efficiency by injecting the maximum available power at the renewable source, as well as by controlling the power factor of the inverter-grid connection in a four quadrant operation; the latter

makes use of the instantaneous reactive power theory [18] for 3-phase systems which allows the control of the instantaneous active and reactive powers in decoupled d-q axes [19]. The global 3-phase grid-connected system can be divided into the power and control subsystems [17], whose block diagrams are depicted in Figure 2.1.

2.1   Power Subsystem

The power subsystem is shown in the upper zone of Figure 2.1 and is formed by the renewable energy source, an inverter, the LCL filter, the transformer, the EMI filter and the utility grid. Depending of the requirements of the installation, an optional DC/DC boost converter must be used. Following, a brief description of each block is developed.

2.1.1 Renewable sources:

News sources of energy such as Photovoltaic, Wind, Fuel Cell, etc., can be connected to the utility grid with the aim of power injection with good quality as a collaborative effort towards the mitigation of the greenhouse effect. The function of the renewable agents is to supply the necessary power for the renewable grid-connected system. Some renewable sources are mention below:

Fuel Cell (FC): One of the main technologies with a higher impact in Distributed Generation (DG) as a source of power is the based on FCs [20]. FC is a device that converts the chemical energy of fuel directly into dc electrical energy [21,22] and has a wide variety of potential applications including micro power, transportation, airplane and cogeneration applications [20,23]. The most significant advantages are its low levels of greenhouse gas emissions and its high energetic density [24,25]. Fuel cells are generally classified according to the type of electrolyte that uses and the electrolyte type depends of the temperature range

of operation [25-27]. Although the voltage of a fuel cell is usually small, with a theoretical maximum being around 1.2 V, fuel cells may be connected in parallel and/or in series to obtain the required power and voltage [25]. Due to the final low dc voltage output characteristic of the arrange, a power conditioning system is necessary, which can include inverters and DC-DC converters in order to supply the normal customer load demand or send electricity to the utility grid [22,25].

Photovoltaic (PV): Photovoltaic cell is an electric device that produces electric energy when it is exposed to direct sunlight and connected to a load. The function of a PV module is to supply the necessary power for the renewable grid-connected system, and it will depend of the available solar irradiance [28] and the temperature, meanwhile its size (arrange of parallel-series PV cells) will depend of the required power of the PV system [29]. Like fuel cell systems, a power conditioning system is also necessary for PV.

Wind Power: Wind energy is becoming one of the most important energy source [30] and it is one of the most development renewable agents [1]. In a wind renewable agent, the wind power is transformed into electricity through an electromechanical energy conversion [31]. The main components of a wind turbine are: the rotor of the turbine, the transmission box, the generator, the transformer and a power condition system based on power electronics [32]. Due to the variations of the wind velocity, a wind turbine must operate at variable speed which causes variations in the electric frequency of the wind generator. This could be a drawback because of the frequency incompatibility between the wind generator and the 3-phase utility grid, being necessary a power conditioner based on power electronics [32,33] to accommodate the frequency of the wind generator to that of the utility grid.

2.1.2 DC/DC boost converter

The arrange of series cells is necessary for increasing the level of the dc voltage at the output of some renewable sources (e.g. PV and FC systems), but in many cases this is not enough in order to guarantee the proper operation of the inverter. For this, a DC/DC boost converter must be used instead, built with semi-conductor electronic devices, an inductor and a capacitor in parallel with a resistor [24].

2.1.3 The inverter

The inverter is the main device of the grid-connected renewable agent and its mission is to convert the generated dc voltage into suitable ac currents to be fed into the 3-phase low-voltage utility grid [24,34]. Voltage Source Inverters (VSI) are commonly used as the power conditioner units to interface renewable resources to the utility grid in a Distributed Generation (DG) framework [34,35], and they are built with semiconductor devices operating in switch-mode. Pulse-width modulation (PMW) and space vector modulation (SVM) [36] techniques are used to control the gate signals of the power switches according to the averaged voltage and current references. A review of several topologies for interfacing renewable resources to the utility grid can be found in [24].

In order to obtain the higher efficiency of the renewable system, these units are usually controlled in a digital manner with up-to-date powerful microcontrollers and/or programmable logic devices such as FPGAs, allowing the automation of the power flow control with adaptive control algorithms, the reduction of the time response to grid perturbations and faults, and the monitoring of the main grid variables.

The power converter of the PV system shown in Figure 2.1 works in inverter-mode (3-phase Voltage Source Inverter (VSI)) since it delivers all the incoming power from the PV generator into the 3-phase utility grid, although an opposite power flow is also possible (rectifier-mode), being able to feed local dc loads from the utility grid.

2.1.4 LCL filter

In addition of guaranteeing a constant power delivery to the 3-phase utility grid, renewable agents must fulfil the power quality regulations. The maximum total harmonic distortion (THD) for the 3-phase currents must be around 5% [37] according to several normative [38,39], whereas the normative for the low-order harmonic distortions is indeed more restrictive. A resume of different standards about power quality for photovoltaic systems can be found in [40]. Ripples are created in the output currents of the inverter due to the high frequency commutation of the IGBTs, meanwhile the low-order harmonics are produced by non-linear loads. The best solution for correcting the high frequency ripples is by using an LCL filter in the ac side of the inverter [41].

2.1.5 The transformer

In DG a transformer can be used for two main reasons: one reason is to adequate the level of voltage at the output of the inverter to the nominal voltage of the utility grid, meanwhile the other reason is to exert a galvanic isolation between the renewable agent and the utility grid, energy consumers and loads.

2.1.6 EMI filter

In a grid-connected renewable agent, it is necessary to take into account the harmonic pollution due to the Electromagnetic Interference (EMI). These EMIs

are caused by the commutation of semiconductor electronic devices (IGBTs and diodes) [42] and an EMI filter is needed to reduce it. There are several methodologies to design an appropriate EMI filter, some of them are based on trial and error [42,43], and some novel methodologies are cited in several publications, including [43,44].

2.1.7 The 3-phase utility grid

Since this thesis is focused in a DG environment, the renewable agents are connected to a 3-phase low-voltage utility grid with a nominal *rms* voltage of 230V (phase-to-neutral) and a nominal frequency of 50Hz. However, some disturbances will affect the value of the nominal conditions mentioned above: the effect of nonlinear loads will produce low-order frequency harmonics pollution, ground faults will produce voltage unbalances, and the connection-disconnection of large loads can affect the utility grid stability or/and due to transient faults, the nominal frequency will vary around its nominal value.

According to Figure 2.1, the dc side of the inverter can be described as follows:

$$
\begin{aligned}
i_{RS} &= i_{IGBT} + i_{clink} + i_{CC} \\
i_{CC} &= s_u \cdot i_u + s_v \cdot i_v + s_w \cdot i_w \\
i_{clink} &= C_{link} \frac{dv_{CC}}{dt} \\
P_{RS} &= i_{RS} v_{RS}
\end{aligned}
$$

(Eq. 2.1)

where v_{RS}, i_{RS} are the voltage and the output current of the Renewable Source, respectively, P_{RS} is the available power for a specific input condition, v_{CC} is the dc bus voltage, i_{clink} is the current through the link capacitor C_{link}, i_{IGBT} is the current through the power switch of the DC/DC boost converter, and i_{CC} is the current delivered to the 3-phase VSI (which is a function of the line currents

i_u, i_v, i_w and the states of the power-poles s_u, s_v, s_w (1:'on', 0:'off', s_i-upper pole, s_i\-lower pole in the 3-phase VSI).

Neglecting the effect of the LCL filter to the fundamental and low-order frequencies of the utility grid voltages [17], the voltage in the filter capacitor is nearly the same that the voltage in the three phase utility grid. So, the dynamic in the ac side of the inverter can be expressed in a vector way and approximated as follows:

$$\mathbf{u} - \mathbf{u_{AC}} = R\mathbf{i} + L\frac{d\mathbf{i}}{dt} = \mathbf{u_R} + \mathbf{u_L} \qquad \text{(Eq. 2.2)}$$

where $\mathbf{u}$, $\mathbf{i}$, $\mathbf{u_{AC}}$ are the inverter voltage, the inverter line current and the utility grid voltage space vectors, respectively, L is the line inductance and R its resistance.

In a three-wire configuration 3-phase grid-connected system with no zero-sequence component for the 3-phase currents (as the one used in this thesis), it has two degree of freedom and can be analyzed in the $\Re^2$ plane, allowing the control of the instantaneous active and reactive powers in decoupled orthonormal axes. For this, two frames are mainly used: the stationary reference frame [45] which uses the αβ fixed axes, and the rotating synchronous reference frame which uses the d-q rotating axes [46].

For a 3-phase system described by vector $\mathbf{x}$=[x_a x_b x_c]´, where x_a, x_b, and x_c are instantaneous 3-phase variables, the Clarke transformation [45] is defined as follows:

$$\begin{bmatrix} x_o \\ x_\alpha \\ x_\beta \end{bmatrix} = \sqrt{\frac{2}{3}} \begin{bmatrix} \dfrac{1}{\sqrt{2}} & \dfrac{1}{\sqrt{2}} & \dfrac{1}{\sqrt{2}} \\ 1 & -\dfrac{1}{2} & -\dfrac{1}{2} \\ 0 & \dfrac{\sqrt{3}}{2} & -\dfrac{\sqrt{3}}{2} \end{bmatrix} \begin{bmatrix} x_a \\ x_b \\ x_c \end{bmatrix}$$ (Eq. 2.3)

where x_0 is the zero-sequence component and $x_{\alpha,\beta}$ are the αβ components of vector **x**.

The Park vector transformation [46] is defined as follows:

$$\begin{bmatrix} x_d \\ x_q \end{bmatrix} = \begin{bmatrix} \cos\theta & \sin\theta \\ -\sin\theta & \cos\theta \end{bmatrix} \begin{bmatrix} x_\alpha \\ x_\beta \end{bmatrix}$$ (Eq. 2.4)

where $x_{d,q}$ are the d-q components of vector **x**.

Expressing Eq. 2.2 in the rotating synchronous reference frame with its d-q components, the instantaneous active power (p) and the instantaneous reactive power (q) can be expressed as follows [17,47]:

$$\begin{aligned} p &= u_{ACd}\, i_d + u_{ACq}\, i_q \\ q &= u_{ACq}\, i_d - u_{ACd}\, i_q \end{aligned}$$ (Eq. 2.5)

where u_{ACd}, u_{ACq}, i_d and i_q are the d-q components of 3-phase voltages and currents, respectively, allowing a decoupled control of the instantaneous active and reactive powers if vector $\mathbf{u_{AC}}$ is aligned with the d axis ($u_{ACq}=0$). In this case, conventional PI regulators can be used due to the constant nature of d-q components, allowing zero error at steady state.

On the contrary, expressing Eq. 2.2 in the stationary reference frame with its $\alpha\beta$ components, the power flow between the 3-phase VSI and the utility grid can be

deduced by using the instantaneous reactive power theory [48]. So, the instantaneous active power (p) and the instantaneous reactive power (q) can be expressed as follows [18,49]:

$$p = u_{AC\alpha}\, i_{\alpha} + u_{AC\beta}\, i_{\beta}$$
$$q = u_{AC\beta}\, i_{\alpha} - u_{AC\alpha}\, i_{\beta}$$

(Eq. 2.6)

where $u_{AC\alpha}$, $u_{AC\beta}$, i_{α} and i_{β} are the $\alpha\beta$ components of 3-phase voltages and currents, respectively. In this case, Proportional-Resonant (PR) controllers must be used in order to achieve zero error at steady state due to the sinusoidal nature of the $\alpha\beta$ components.

2.2   Control Subsystem

The control subsystem is shown in the bottom zone of Figure 2.1. It is formed by the following blocks: 3-phase VSI control, the DC/DC control, the Maximum Power Point Tracking (MPPT), and Monitoring.

2.2.1 The 3-phase VSI control block

The 3-phase VSI control block is formed by a cascaded control and the synchronization algorithm modules. In this, the Clarke and Park vector transformations are needed for these modules, and the output is the status of the 3-phase power switches using the Space Vector Modulation (SVM) block.

2.2.1.1 Cascaded Control

The control strategy uses a cascaded control: Proportional-Integral (PI) regulators or Proportional-Resonant (PR) regulators are used for the inner line currents loop, whereas a PI regulator is used for the outer dc bus voltage loop.

2.2.1.1.1 Outer loop

The outer loop regulator compares the dc bus voltage in the link capacitor with a voltage reference which comes from the MPPT algorithm block, keeping a constant dc voltage and assuring the power flow balance between the Renewable source and the utility grid. This control loop is performed by using a PI controller. The tuning of the PI controller will define its dynamic response according to the crossover frequency (f_{cV}), the phase margin (PM_V), and the damping factor (ζ_c) specified for a rated power and the link capacitor (C_{link}), and neglecting the influence of the faster inner loop, whose transfer function is approximated to unity.

The detailed explanation of the outer loop regulator is beyond the scope of this thesis, but the interested reader may follow the steps described in [17,50] so as to calculate the constants of the PI regulator.

2.2.1.1.2 Inner loop

The inner control loop uses two controllers to regulate the d-q or the $\alpha\beta$ components of the line currents allowing the synchronization of the 3-phase inverter line currents with the 3-phase utility grid voltages. In the case of that a d-q control is performed PI regulators are used to regulate the d-q components of the inverter currents, whereas PR controller are used to regulate de $\alpha\beta$ components of the inverter currents.

2.2.1.2 Synchronization Algorithm

The synchronization algorithm for attaining a controllable power factor in the connection must detect the phase angle of the 3-phase utility grid voltages with optimal dynamic response and reliability in order to obtain the synchronization of the controlled 3-phase inverter currents and ensure the proper behaviour of the

inverter control strategy. There are several studies, which show different structures to estimate the utility-grid voltage phase angle in order to obtain the synchronization of the current inverter with the 3-phase utility grid voltages [51-54].

2.2.2 DC/DC control block

The DC/DC control block for the DC/DC boost converter computes the duty cycle and decides the status of its power switch with a Pulse Width Modulation (PWM) strategy.

2.2.3 MPPT block

The MPPT block is used to extract the maximum available power of the renewable source to increase the efficiency of the system.

As an example, the voltage characteristic of PV systems is not lineal and it is also time-variant, due to a series of atmospheric variations [55]. In PV grid-connected renewable agents it is necessary to extract its maximum available power to increase the efficiency of the system [19] and an algorithm-module named MPPT is used for this task [56]. The MPPT is an essential part of a PV system and several methods for MPPT algorithms have been designed, among them, Perturbation and Observation, Incremental Conductance and Ripple Correlation Control [57].

In the case of wind power, the speed of the wind is not constant and it is necessary to extract the maximum power possible in order to obtain the higher efficiency of the system. For this, the turbine must operate at optimum speed and a MPPT is used to find this point of the maximum efficiency [58].

2.2.4 Monitoring module

In order to track the main parameters concerning to the power features of the renewable agent, a monitoring block can be added to the control subsystem as can be observed in Figure 2.1. Several parameters, among others, can be monitored: the active (p) and reactive (q) powers, the angle phase (θ) and the frequency (ω) of the 3-phase utility grid voltage, the power factor (PF) and a flag (G) for detecting when the renewable agent is working in generation or consumption-mode.

2.3   Conclusions

An overview of the main parts of grid-connected renewable agents has been shown in this Chapter as an introduction to the renewable agents connected to the 3-phase low-voltage utility grid in a Distributed Generation environment. For the sake of simplicity, the global system has been divided into the control and the power subsystems.

The main equations of the power subsystem have been proposed so as to study the power balance between the renewable source and the utility grid. The Clarke and Park transformations are introduced as the tool for doing the vector analysis for three-wire configuration 3-phase grid-connected system, and be able to exert a decoupled control of the instantaneous active and reactive powers.

The control subsystem is also described as an overview, though a more deep analysis will be carried out in the next chapters of this thesis.

CHAPTER 3
Synchronization Algorithms used in Grid-Connected Inverters

This Chapter presents five synchronization algorithms that are commonly used in Grid-Connected Renewable Agents. The algorithm structures are studied and their corresponding block diagram are shown and explained in detail. The behaviour of the algorithms is studied according of their response under voltage unbalances, frequency variations and low-order voltage harmonics. The advantages and disadvantages of the algorithms are discussed by analyzing some simulations done with MATLAB/SIMULINK tool from The MathWorks, Inc. Later on, the final validation is done by doing real-time digital tests of the synchronization algorithms with a Real-Time Digital Simulator (RTDS) platform.

In a Distributed Generation (DG) environment it is necessary an appropriated control of the power factor of the inverter-grid connection to obtain the maximum efficiency in the renewable agent, and the synchronization algorithm is the module used for detecting the phase angle of the 3-phase utility grid voltages with optimal dynamic response.

There are several studies, which show different structures to estimate the utility-grid voltage phase angle in order to obtain the synchronization of the current inverter with the 3-phase utility grid voltages. Some of the main synchronization methods that can be mention are the following ones: Synchronous Reference Frame Phase-Locked Loop (dqPLL) [51]**,** Positive Sequence Detector plus a dqPLL (PSD+dqPLL) [52,59], Dual Second Order Generalized Integrator Phase-Locked Loop (DSOGI-PLL) [53,60], Dual Second Order Generalized Integrator Frequency-Locked Loop (DSOGI-FLL) [61,62] and Multiple Second Order Generalized Integrator Frequency-Locked Loop (MSOGI-FLL) [54].

The algorithms mentioned above have their advantages and disadvantages, being the dqPLL the simplest one, and the Multiple Second Order Generalized Integrator Frequency-Locked Loop (MSOGI-FLL) technique the most sophisticated. All these algorithms can be used in different renewable agents, and the selection will depend on the requirements and/or regulations to be fulfilled. A detail explanation of the above algorithms will be carried out in this Chapter where their structures, design and operation are discussed.

3.1   Synchronous Reference Frame Phase-Locked Loop (dqPLL)

There are several studies which show different structures for synchronization algorithms, being the Phase-Locked Loop (PLL) the classical one. A 3-phase PLL structure is shown in Figure 3.1, which is made by the Clarke and Park

transformations (also known as abc→d-q transformation) [63], the PI regulator [64] as the loop filter, and an integrator as the voltage-controlled oscillator (VCO). This PLL structure is also known as Synchronous Reference Frame PLL or dqPLL: the input variables are the 3-phase utility grid voltages (u_a,u_b,u_c), and the output variable is the phase angle (θ_{obs}).
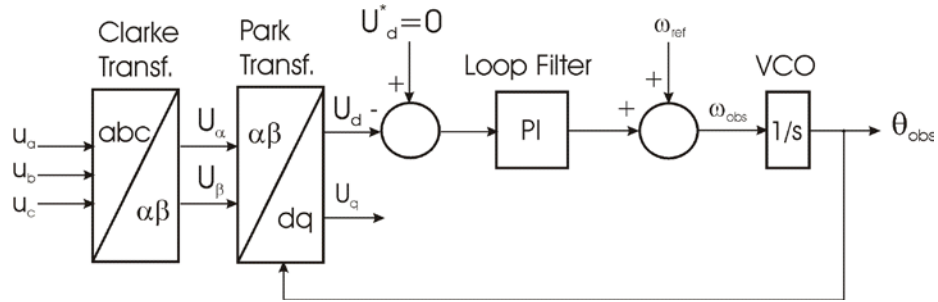
Figure 3.1. Block diagram of the dqPLL synchronization algorithm.

The design of the PLL gain is a critical point within this process. From the point of view of dynamic systems, high gains will imply higher dynamics [65], but stability may become unacceptable. The closed loop transfer function of the dqPLL of Figure 3.1 is giving by Eq. 3.1 [66]:

$$H_{(S)} = \frac{K_p s + K_i}{s^2 + K_p s + K_i}$$

(Eq. 3.1)

where K_p and K_i are the proportional and integral gains, respectively, of the employed PI regulator. Eq. 3.1 is a second order transfer function, similar to Eq. 3.2.

$$G_{(S)} = \frac{2\zeta\omega_0\, s + \omega_0^2}{s^2 + 2\zeta\omega_0\, s + \omega_0^2}$$

(Eq. 3.2)

where: ω_0 is the natural angular frequency, and ζ is the damping factor.

Equating Eq. 3.1 and Eq. 3.2:

$$K_p = \frac{9.2}{t_s} \tag{Eq. 3.3}$$

$$\omega_0 = \frac{Kp}{2\zeta} \tag{Eq. 3.4}$$

$$K_i = \omega_0{}^2 \tag{Eq. 3.5}$$

where t_s is the settling time [66].

As a design example of a dqPLL, gains are computed so as to obtain a $t_s = 50\text{ms}$ allowing a fast response of the algorithm when a variation of the nominal frequency occur, and a damping factor $\zeta = 0.707$ is chosen. Equating Eq. 3.3, Eq. 3.4, and Eq. 3.5, the other variables can be computed: $K_P = 184$, $\omega_0 = 130\text{rad/s}$ and $K_I = 16928$. The obtained value of ω_0 guarantees a trade-off between the dynamic, harmonic rejection capability, and the stability of the dqPLL algorithm. It must be pointed out that a normalization of the PI gains in function of the peak voltage of the utility grid is necessary in order to obtain the proper performance of de dqPLL algorithm.

The step response and the Bode plot of the design dqPLL algorithm are shown in Figure 3.2a, where an overshoot of 20% is obtained, and Figure 3.2b, respectively.

The dqPLL method has the advantage that its implementation is relatively easy; in addition to this, under the influence of some low-order harmonic distortions and frequency variations of the 3-phase utility grid voltages, the dqPLL could have an acceptable operation. The major disadvantage of the dqPLL is its high sensibility to voltage unbalances [52,54].
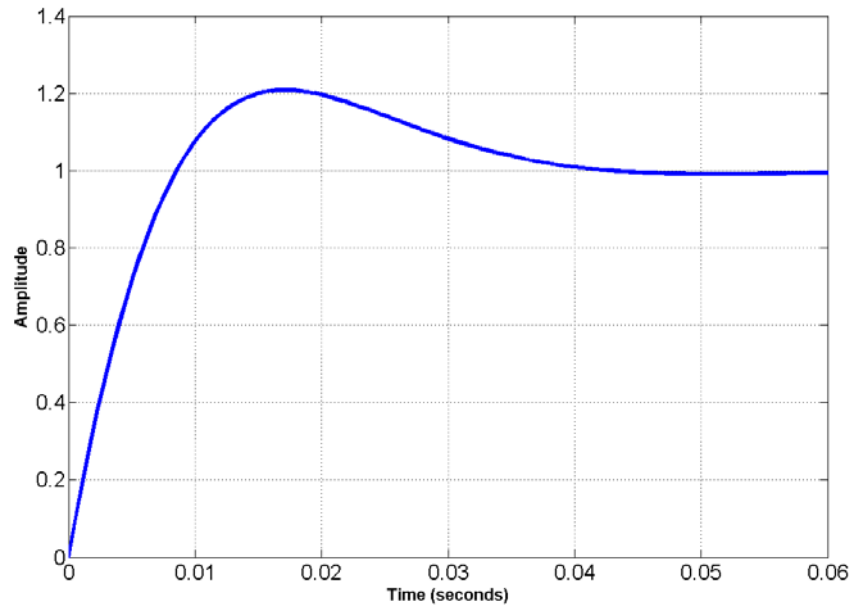
(a)
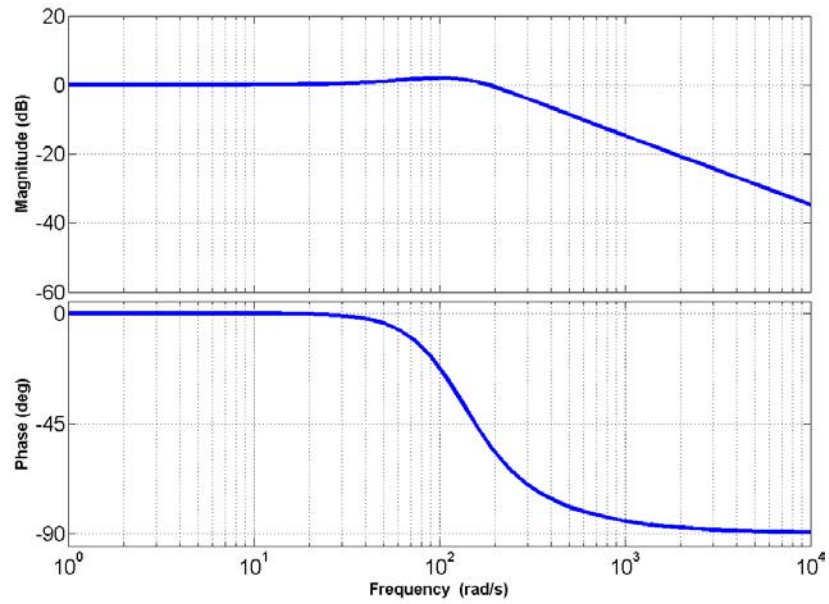
(b)

Figure 3.2. (a) Step response of the design dqPLL algorithm. (b) Bode plot of the design dqPLL algorithm.

3.2 Positive Sequence Detector plus a dqPLL (PSD+dqPLL)

The dqPLL method is very sensible to grid voltage unbalances [52], which also produces second order harmonics in d-q synchronous reference frame (rotating at the angular speed ω) due to the effect of the inverse sequence (rotating at the angular speed –ω); indeed, the sensors to be used can introduce second order harmonics due to accuracy errors. In addition, the voltages of the utility grid could be contaminated with harmonics and affected by variations of the fundamental frequency. A solution to the problems caused by the unbalance 3-phase utility grid voltages is adding a Positive Sequence Detector (PSD) block, which is based on the symmetrical components method or Fortescue theorem [67]. Applying this theorem, it is possible to decompose the unbalanced 3-phase utility grid voltages into its positive, negative and zero sequences, allowing a better performance of the PLL algorithm. In time domain, the instantaneous positive sequences component v^+_{abc} of a voltage vector is given by [52]:

$$v_a^+(t) = \frac{1}{3}v_{a(t)} - \frac{1}{6}\left(v_{b(t)} + v_{c(t)}\right) - \frac{1}{2\sqrt{3}}S_{90}\left(v_{b(t)} - v_{c(t)}\right) \qquad \text{(Eq. 3.6)}$$

$$v_b^+(t) = -\left(v_a^+(t) + v_c^+(t)\right) \qquad \text{(Eq. 3.7)}$$

$$v_c^+(t) = \frac{1}{3}v_{c(t)} - \frac{1}{6}\left(v_{a(t)} + v_{b(t)}\right) - \frac{1}{2\sqrt{3}}S_{90}\left(v_{a(t)} - v_{b(t)}\right) \qquad \text{(Eq. 3.8)}$$

where S_{90} is a 90-degree phase-shift operator which can be designed with the following transfer function [52]:

$$H_{S_{90}}(s) = \frac{1 - \dfrac{s}{\omega_0}}{1 + \dfrac{s}{\omega_0}}$$
(Eq. 3.9)

where: ω_0 is the natural angular frequency.

By adding the PSD block with Eqs. 3.6, 3.7 and 3.8 to the dqPLL structure shown in Figure 3.1, a PSD+dqPLL synchronization algorithm able to extract the positive sequence of the 3-phase utility grid voltages is obtained, and then, a reliable detection of the positive sequence of the frequency and phase will be achieved when voltage unbalances occur [59]. The overall structure of the PSD+dqPLL is shown in Figure. 3.3.
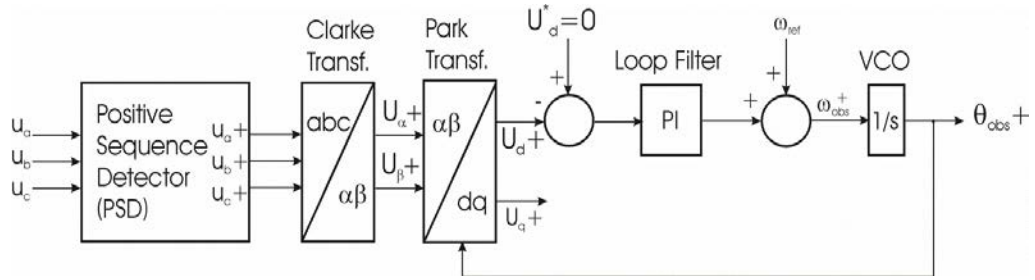
Figure 3.3. Block diagram of the PSD+dqPLL Synchronization algorithm.

A possible drawback of the PSD can be observed in Eq. 3.9. The S_{90} phase-shift operator has been implemented using a non-adaptive nominal angular frequency ω_o, making this filter sensible to frequency variations of the utility grid voltages, which will lead to a small degradation of the power factor of the inverter-grid connection.

3.3 Dual Second Order Generalized Integrator Phase-Locked Loop (DSOGI-PLL)

Another solution to overcome the problems caused by the voltage unbalance to the detection of the phase is presented in [53,60], where a Dual Second Order Generalized Integrator PLL (DSOGI-PLL) is proposed. In this, the in-quadrature signals (90° shifted) for $v_{\alpha\beta}$ are computed by two Second Order Generalized Integrator [68] with a Quadrature Signal Generation (SOGI-QSG) [61], one of them shown in Figure 3.4. The block diagram of the SOGI, which behaves as an integrator with infinite gain, is depicted in blue and its transfer functions is described by Eq. 3.10.

$$SOGI(s) = \frac{v'}{k\varepsilon_v}(s) = \frac{\omega's}{s^2 + \omega'^2} \qquad \text{(Eq. 3.10)}$$

whereas the transfer functions of the in-quadrature signals *DQ* are described by Eqs. 3.11 and 3.12.

$$D(s) = \frac{v'}{v}(s) = \frac{k\omega's}{s^2 + k\omega's + \omega'^2} \qquad \text{(Eq. 3.11)}$$

$$Q(s) = \frac{qv'}{v}(s) = \frac{k\omega'^2}{s^2 + k\omega's + \omega'^2} \qquad \text{(Eq. 3.12)}$$

ω' is the centre angular frequency of the adaptive filter, and k is the gain of the SOGI block. The transfer functions described by Eq. 3.11 and Eq. 3.12 suggest a band-pass and a low-pass filter behaviour, respectively, and Eq. 3.12 imply a constant lag of 90º between the qv' and v which will not be a function of the variation of ω' and k [61], yielding also to an insensitive system for frequency variations at the input signal v when $\omega = \omega'$ (ω is the angular frequency of v).

Equations 3.11 and 3.12 are second order transfer functions, and its dynamic response will depend on the localization of the poles in the complex plane. In addition, the band-pass and low-pass filter behaviour described above suggest the harmonic rejection capability of these filters. So, a trade-off between the proper bandwidth for harmonic rejection, and the proper settling time (t_s) with the corresponding overshoot for the dynamic response, must be imposed for the calculation of k for a specific ω'.
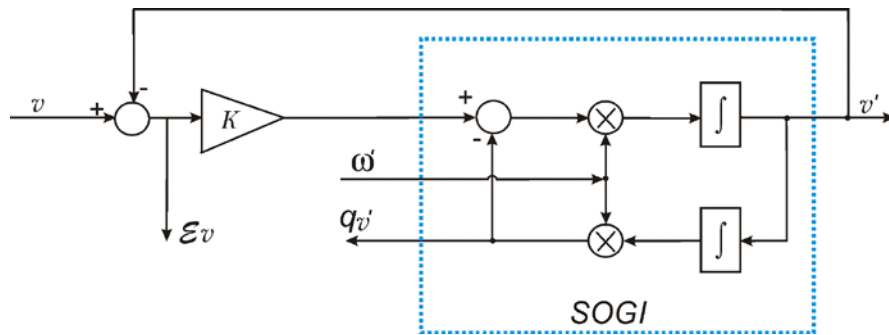
Figure 3.4. Block diagram of a SOGI-QSG.

Figure 3.5a shows the Bode plot of the transfer functions of the SOGI-QSG described by Eq. 3.11 and Eq. 3.12: the upper zone of Figure 3.5a shows the magnitude of the Bode plot, meanwhile the bottom zone shows the phase angle, both for several values of k. The trace of the phase depicts a perfect 90° shifting between the in-quadrature signals for all k. In addition, Figure 3.5b depicts the time evolution of the in-quadrature signals and the corresponding settling times for all k.

Table 3.1 shows the influence of gain k in the SOGI-QSG behavior according to the settling time, overshoot, damping factor, and harmonic rejection of Q(s): when k increases, the settling time and the harmonic rejection decreases, but the overshoot increases instead. It must be observed that when k =1.414, a good trade-off between the harmonic rejection (for the 5th and 7th harmonics) and the

dynamic response is achieved, corresponding to a damping factor $\zeta_{SOGI-QSG} = 0.707$

for second order systems [69].

(a)

(b)
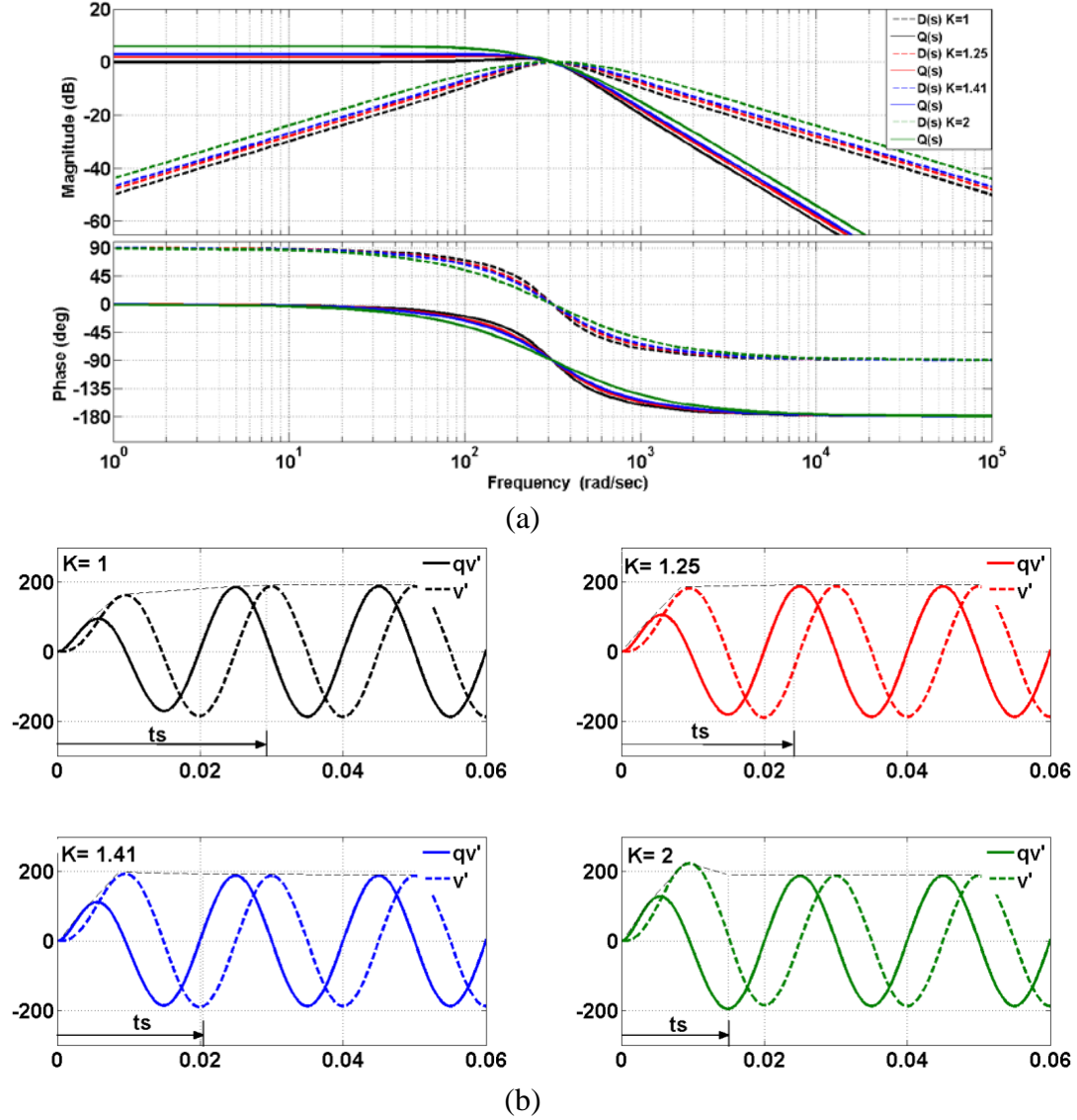
Figure 3.5. (a) Bode plot of a SOGI-QSG using the transfer functions of Equations 3.11 and 3.12 for several values of k. (b) Time evolution of the in-quadrature signals of the SOGI-QSG for several values of k.

It must be pointed out that the SOGI-QSG synchronization algorithm is tuned to the centre angular frequency ω', which is an input signal to this block (see Figure 3.4), and can behave as an adaptive filter scheme if an external circuit or algorithm is able to measure or detect this frequency. Clarke transformation [45] is applied to the input 3-phase voltages in order to obtain its $\alpha\beta$ voltage components ($V_{\alpha\beta}$), and two SOGI-QSG blocks are used to obtain its in-quadrature signals. A DSOGI-QSG structure for 3-phase systems [61] is shown in Figure 3.6.

Table 3.1. DSOGI-QSG behaviour according gain k.

k	$\zeta_{SOGI-QSG}$	Overshot (%)	Settling time (ms)	Harmonic Rejection of Q(s) (dB)	
				5th	7th
1	1	0	29.3	-27.72	-33.7
1.25	0.8	1.5	23.4	-25.89	-31.81
1.414	0.707	4.3	20.7	-24.9	-30.78
2	0.5	16.3	14.6	-22.23	-27.94
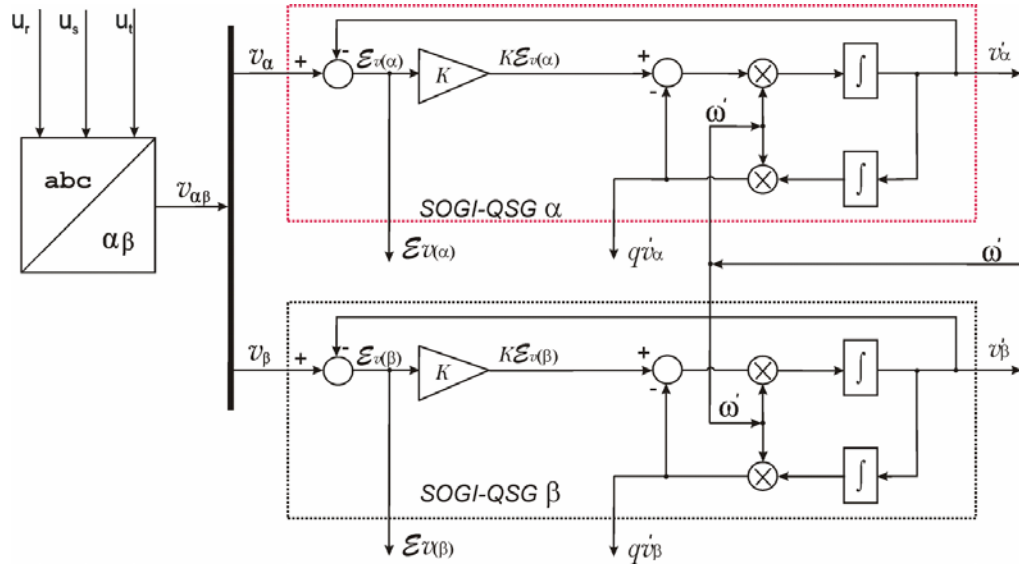
Figure 3.6. Block diagram of a DSOGI-QSG.

Knowing that the instantaneous positive sequence component ($v_{\alpha\beta}^{+}$) of a voltage vector described by $V_{\alpha\beta}$ is given by [70]:

$$v_{\alpha\beta}^{+} = \frac{1}{2}\begin{pmatrix} 1 & -q \\ q & 1 \end{pmatrix} v_{\alpha\beta} \tag{Eq. 3.13}$$

where $q = e^{-j\frac{\pi}{2}}$ is a phase-shift operator to obtain the in-quadrature version of an original wave form, a Positive Sequence Calculator (PSC) must be designed and applied to the in-quadrature output signals so as to compute the positive sequence of the input 3-phase unbalanced voltages $v_{\alpha\beta}^{+\prime}$.

Finally, the positive sequences of the $\alpha\beta$ voltage components ($V_{\alpha\beta}+$) are used to estimate the frequency with a Phase-Locked Loop (PLL) block. The final diagram of the DSOGI-PLL is shown in Figure 3.7.
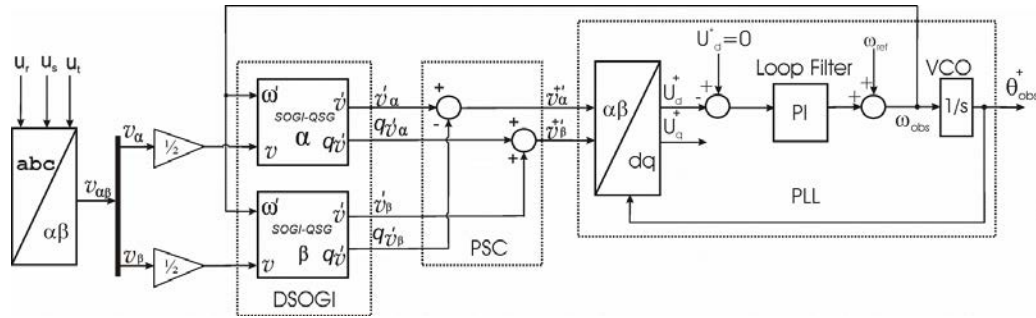
Figure 3.7. Block diagram of a DSOGI-PLL synchronization algorithm.

In order to obtain the proper performance of the DSOGI-PLL algorithm, an important aspect that must be taken into consideration when designing the K_P and K_I gains of the PLL block: the natural angular frequency (ω_0) of the transfer function of the PI regulator should be smaller than the centre angular frequency (ω') of the adaptive filter of the SOGI blocks.

3.4 Dual Second Order Generalized Integrator Frequency-Locked Loop (DSOGI- FLL)

A good alternative for the frequency and phase detections when voltage unbalances and frequency variations occur in the 3-phase utility grid voltages is described in [61,62], where a Dual Second Order Generalized Integrator Frequency-Locked Loop (DSOGI-FLL) is proposed. In the same manner of DSOGI-PLL this is based on the use of Quadrature Signal Generation (SOGI-QSG) but instead of using a Phase-Locked Loop (PLL) a Frequency-Locked Loop (FLL) is used.

The Frequency-Locked Loop (FLL) structure, shown in Figure 3.8 [61], can be used to measure the angular frequency ω of the input signal v (in this case, ω' is the output or estimated angular frequency of the input signal v) without using trigonometric functions [61], and making easier its implementation in conventional microcontrollers. The nominal angular frequency ω_c is feed-forward to this block in order to improve the dynamic response of the algorithm.
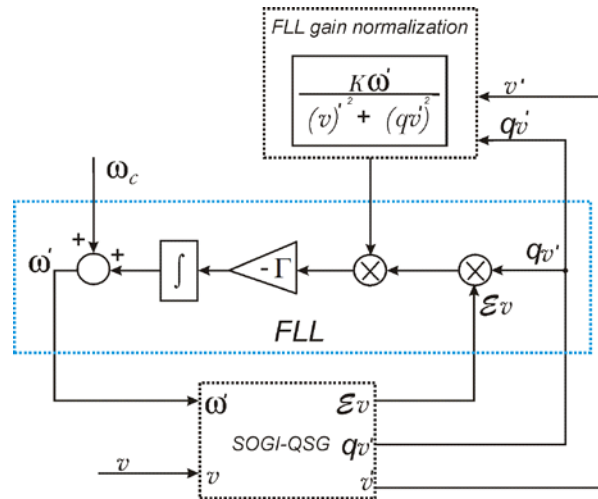
Figure 3.8. Block diagram of a Frequency-Locked Loop (FLL) with gain normalization.

FLL gain normalization is exerted so as to make this independent of the gain k of the SOGI-QSG block and of the amplitude of the utility grid voltage. In this case, the FLL algorithm can be approximated by a first order system with one integrator for steady state operation and linearized around the nominal output variables of the SOGI-QSG block. So, the settling time t_s can be set approximately by 5τ ($\tau = \dfrac{1}{\Gamma}$ is the time constant of the first order system and Γ is the gain to set $t_{s(FLL)}$):

$$t_{s(FLL)} \approx \frac{5}{\Gamma} \qquad\qquad \text{(Eq. 3.14)}$$

Finally, the measurement of ω' implies the feedback of the qv' signal from the SOGI-QSG block. This signal will have a small amount of harmonic contamination due to the attenuation imposed by the low-pass filter nature of the transfer function Q(s) described by Eq. 3.12.

The preliminary analysis can be extended to 3-phase systems, and Figure 3.9 shows the DSOGI-FLL structure proposed in [61]. Clarke transformation [45] is applied to the input 3-phase voltages in order to obtain its $\alpha\beta$ voltage components ($V_{\alpha\beta}$), and two SOGI-QSG blocks are used to obtain its in-quadrature signals. Knowing that the instantaneous positive sequence component ($v_{\alpha\beta}^{+}$) of a voltage vector described by $V_{\alpha\beta}$ is given by Eq. 3.13, a Positive Sequence Calculator (PSC) must be designed and applied to the in-quadrature output signals so as to compute the positive sequence of the input 3-phase unbalanced voltages $v_{\alpha\beta}^{+}{}'$.

In order to evaluate the performance of the DSOGI-FLL structure, some simulations depict the time evolution of the detected frequency in Figure 3.10. A step of 50-60Hz is exerted in the nominal frequency of the 3-phase utility grid voltages and several gains (Γ) are imposed to study the dynamic response. Using a relatively low Γ (50 and 70) a slow settling time of the FLL is attained (trace in

red and blue). On the contrary, for $\Gamma = 100$ (trace in black), a suitable settling time around two cycles and a half is achieved.
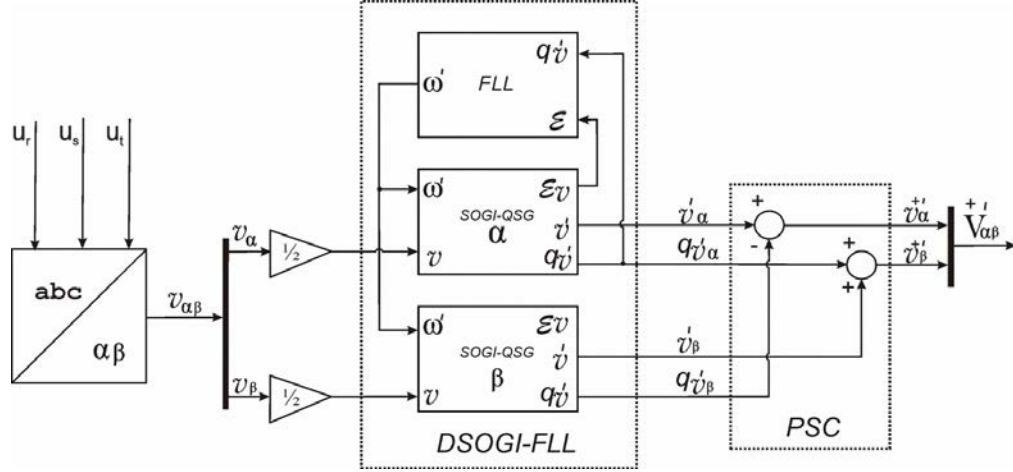
Figure 3.9. Block diagram of a DSOGI-FLL synchronization algorithm.
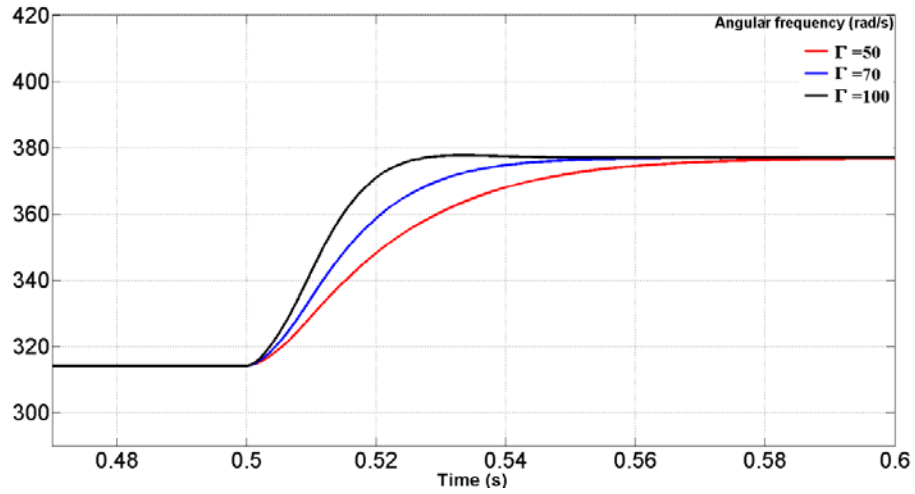
Figure 3.10. Time response of the DSOGI-FLL for several Γ.

Table 3.2 shows the relation between the gain Γ and the corresponding settling time $t_{s(FLL)}$ when a step of frequency of 50Hz to 60Hz is exerted on the utility grid frequency.

Table 3.2. Relation between the gain Γ and $t_{S(FLL)}$ in the FLL block.

Γ	$t_{S(FLL)}$ (ms)
50	100
70	70
100	**50**

Finally, the phase angle for the positive sequence of the 3-phase utility grid voltages can be computed as follows:

$$\theta^{+'} = \tan^{-1}\left(\frac{v_{\beta}^{+'}}{v_{\alpha}^{+'}}\right)$$

(Eq. 3.15)

The DSOGI-FLL synchronization algorithm has a good behaviour for detecting the phase and frequency when unbalance voltages and frequency variations occur in the utility grid, but no good behaviour is attained when low-order harmonics close to the fundamental frequency are present in the utility grid [54].

3.5 Multiple Second Order Generalized Integrator Frequency-Locked Loop (MSOGI-FLL)

The drawback of the DSOGI-FLL synchronization algorithm regarding harmonic rejection can be overcome by introducing a set of adaptive filters, based on the Quadrature Signal Generation (SOGI-QSG), tuned at different low-order harmonic frequencies and working in parallel, together with the Harmonic Decoupling Network (HDN) and the Positive Sequence Calculator (PSC) for each detected harmonic component. This new structure, which is proposed in [54], is named the Multiple Second Order Generalized Integrator Frequency-Locked Loop (MSOGI-FLL) synchronization algorithm.

This thesis deals with the calculation of the fundamental (1), the second (2), the fifth (5) and the seventh (7) voltage harmonic components, as can be seen in Figure 3.11, but the further extension to other harmonic components is completely and easily possible by extrapolation.
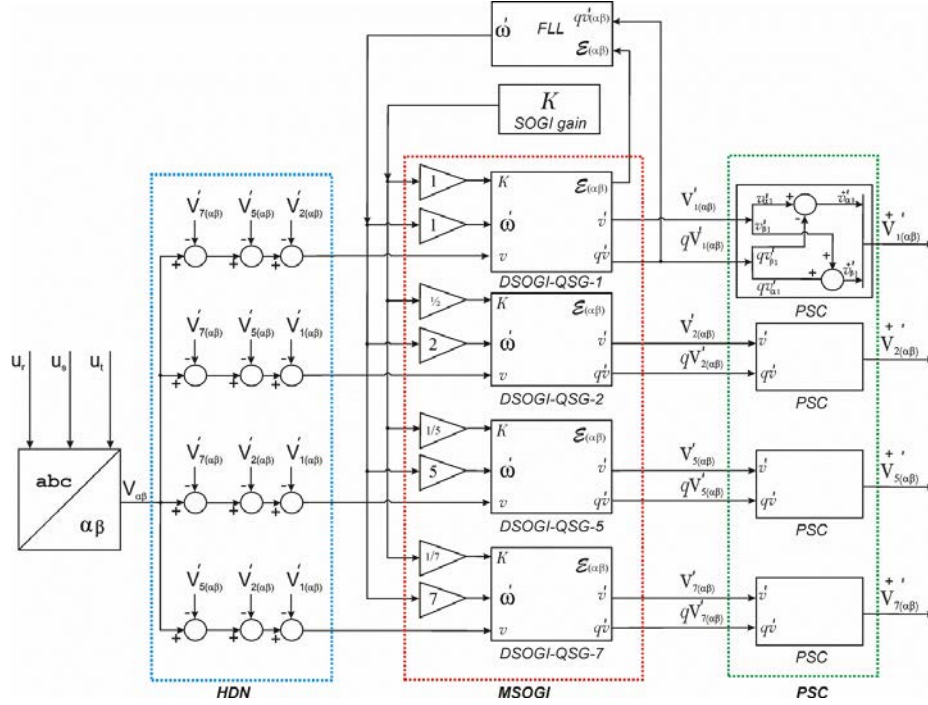
Figure 3.11. Block diagram of a MSOGI-FLL structure.

The Frequency-Locked Loop (FLL) block is used by the MSOGI-FLL structure to measure the fundamental angular frequency of the input signals $V_{\alpha\beta}$ and is described in detail in Figure 3.12: the semi-sum of the product of the error $\mathcal{E}_u$ and qv' in each axis is processed by an integrator with gain $-\Gamma$, being ω_c the feed-forward of the nominal angular frequency for improving its dynamic response. The measured angular frequency ω' is used to set the frequency of each DSOGI-QSG$_i$ block (shown in the red area of Figure 3.11) for the voltage harmonic component to be detected [54].

The FLL gain normalization is exerted so as to make this block independent of the gain k of the DSOGI-QSG block and of the amplitude of the utility grid voltage.

It must be pointed out that the HDN block (shown in the blue area of Figure 3.11) is added to the MSOGI-FLL synchronization algorithm in order to decouple the effect of the several utility grid low-order harmonics from the one involved in the calculation with its corresponding DSOGI-QSG$_i$ block. The outputs of the HDN block are sent to the DSOGI-QSGs and the decouple action is achieved by the feedback of the corresponding $V'_{k(\alpha\beta)}$ DSOGI-QSG outputs (k≠i) into the HDN block, as can be seen in Figure 3.11. As a consequence, the MSOGI-FLL synchronization algorithm is able to detect the separated voltage harmonic components of the 3-phase utility grid voltages.
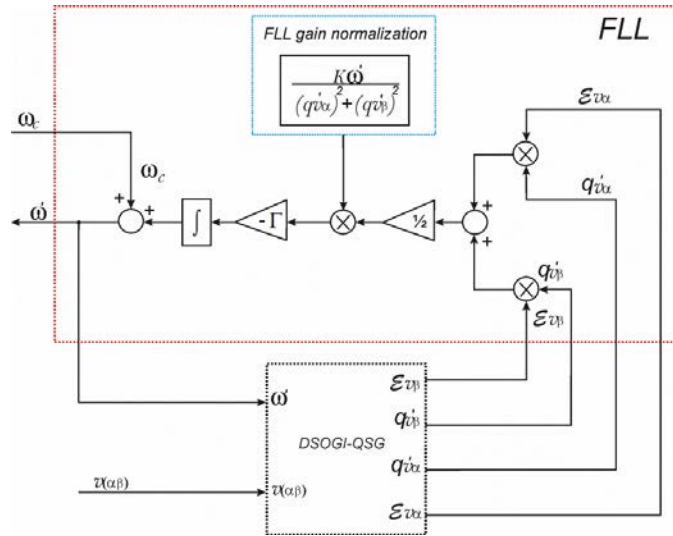
Figure 3.12. Block diagram of a Frequency-Locked Loop (FLL) with normalized gain used in a DSOGI-FLL.

Using Eq. 3.13, Positive Sequence Calculator (PSC) structures (shown in the green area of Figure 3.11) can be used at the output of each DSOGI-QSG block in order to obtain the positive sequence of each harmonic component of the 3-phase utility grid voltages when unbalances occur. The phase angle of the positive

sequence of the fundamental component of the 3-phase utility grid voltages can be calculated using Eq. 3.15.

3.6   Simulations

In order to evaluate the behaviour of the synchronization algorithms, some simulations are performed using a MATLAB/SIMULINK model of the 3-phase PV grid-connected system shown in Figure 2.1 with a nominal power of 10kW and using the parameters listed in Table 3.3.

Table 3.3. Power Subsystem characteristics.

• R=0.0465Ω
• L=1.1mH
• C=4µF (Y-connexion)
• Transformer:
    • R_t= 0.247 Ω
    • L_t=640 µH, neglecting the magnetizing effect
• 3-phase utility grid voltage:
    • U_{ACg}(rms) =232V (phase-to-neutral at grid side)
    • U_{AC}(rms)=$\dfrac{U_{ACg}}{\sqrt{3}}$
    =132.8V (phase-to-neutral at inverter side)
	$f_c = \dfrac{1}{2\pi}\dfrac{R}{L} = 6.72\,Hz$	First order RL

	$f_o = \dfrac{1}{2\pi\sqrt{LC}} = 2400Hz$ $(harm = 48)$ $\zeta = \dfrac{\omega_o}{2}RC = 0.0014$	Second order LC
	$f_{ot} = \dfrac{1}{2\pi\sqrt{L_tC}} = 3145.6Hz$ $(harm = 63)$ $\zeta_t = \dfrac{\omega_o}{2}R_tC = 0.0098$	Second order LtC

The values of the parameters for the control subsystem and the synchronization algorithms are resumed in Table 3.4:

Table 3.4. Control subsystem and the synchronization algorithms characteristics.

Control subsystem parameters

- K_{INV} or K_{PWM}=400V (V_{CC}=600V) (Gain of the inverter)
- C_{link}=2300µF ($\Delta V_{CCmáx}$=60V)
- f_{cI}=1220.8 (open loop cross-over frequency for the inner current loop)
- f_{cV}=12.2Hz (open loop cross-over frequency for the outer dc bus voltage loop)
- PM_V =63.5°=PM_I (phase margin for the outer and inner open loop transfer functions)
- $\zeta_c = \dfrac{\sqrt{2}}{2}$ (damping factor for the closed loop outer voltage loop)
- ΔI=16.7A (S=10KVA) (equivalent step of irradiance for the rated nominal power)
- K_P =0.019
- K_I =10
- $K_{Ih5} = K_{Ih7} = 10$
- ω_0 = 314.16rad/s
- ω_c =1rad/s
- ω_{c5h} =1rad/s, fifth harmonic
- ω_{c7h} =1rad/s, seventh harmonic

Synchronization algorithms parameters

dqPLL and PSD+dqPLL

- ω_0 =130rad/s (dqPLL natural angular frequency)
- T_s = 50ms (settling time)
- $\zeta = \dfrac{\sqrt{2}}{2}$ (damping factor for the dqPLL)

DSOGI-PLL

- $k = \sqrt{2}$ (gain of the SOGI)
- T_s = 50ms (settling time)

- $\zeta_{SOGI-QSG}$ =0.707 (damping factor for the DSOGI)
- ω' = 314rad/s (centre angular frequency for the DSOGI)
- ω_0 =130rad/s (PLL natural angular frequency)

DSOGI-FLL and MSOGI-FLL

- Γ =100 (gain to the settling time of the FLL block)
- $k = \sqrt{2}$ (gain of the SOGI)
- T_s = 50ms (settling time)

3.6.1 Testing the influence of the nominal frequency variation

Since transient faults can produce frequency variations, a step of frequency from 50Hz to 60Hz is exerted at 0.5s. The peak values of the 3-phase utility grid voltage is U_{Peak}=187.9V (phase-to-neutral) as can be observed in Figure 3.13a.

The upper zone of the Figure 3.13b shows the simulation of the time evolution of the detected frequencies for each algorithm. The dqPLL frequency detection is traced in blue colour; in order to attain a trade-off between the dynamic, stability and proper harmonic attenuation, a crossover frequency of 130rad/s is set, which leads to the constants of the PI regulator (K_I=16928 and K_P=184). Adding the PSD block, the frequency detection of the PSD+dqPLL is shown in green colour in Figure 3.13b; the S90 filter has been designed for a nominal frequency of 50Hz and an acceptable response is achieved. The frequency detection by the DSOGI-PLL is show in red colour; the DSOGI gain k =1.41 and the same constants used in the dqPLL are used for the PI regulator of the DSOGI-PLL. The orange trace shows the frequency detection by the DSOGI-FLL using a SOGI gain of k =1.41 and a gain Γ =100 yielding to a settling time of the FLL ($t_{S(FLL)}$) =50ms.

Finally, the frequency detection by the MSOGI-FLL is shown in black colour using the same values of the gains of the DSOGI-FLL algorithm. Some overshoot

can be observed when the dqPLL, the PSD+dqPLL and the DSOGI-PLL algorithms are used; on the contrary when the DSOGI-FLL and the MSOGI-FLL are used to estimate the frequency, no overshoot is observed. The above demonstrates the better dynamics attained when a FLL is used to estimate the frequency of the 3-phase utility grid.

In the case of the phase estimation, a similar behaviour can be observed for all the synchronization algorithms as can be seen in the bottom zone of the Figure 3.13b.

(a)

(b)
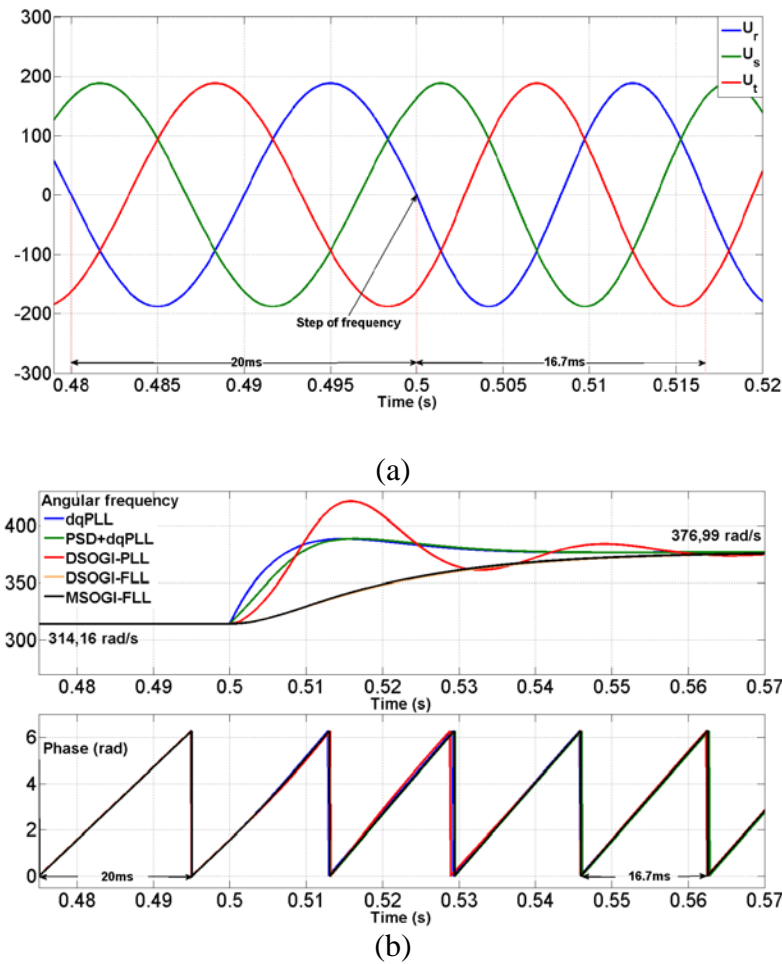
Figure 3.13. (a) Utility grid voltages during a step of the nominal frequency. (b) Time evolution of the detected frequency and phase using the five synchronization algorithms when a step of frequency is exerted.

An important issue to evaluate the vulnerability of the PSD+dqPLL synchronization algorithm is the study of the degradation of the power factor in the inverter-grid connection when frequency variations occur, regarding the international regulations. In Europe, the utility grid frequency is 50Hz and very seldom might have a variation of 49-50.3 [71]. In addition, a maximum frequency oscillation of 50±1 is established by the European Standard EN 50160 [72].

In order to study the degradation of the Power Factor (PF) when variations of frequencies are exerted and the PSD+dqPLL is used as synchronization algorithm, the following test is performed. The synchronizations attained by the PSD+dqPLL synchronization algorithm when frequency variations occur at 0.5s are shown in Figure 3.14.
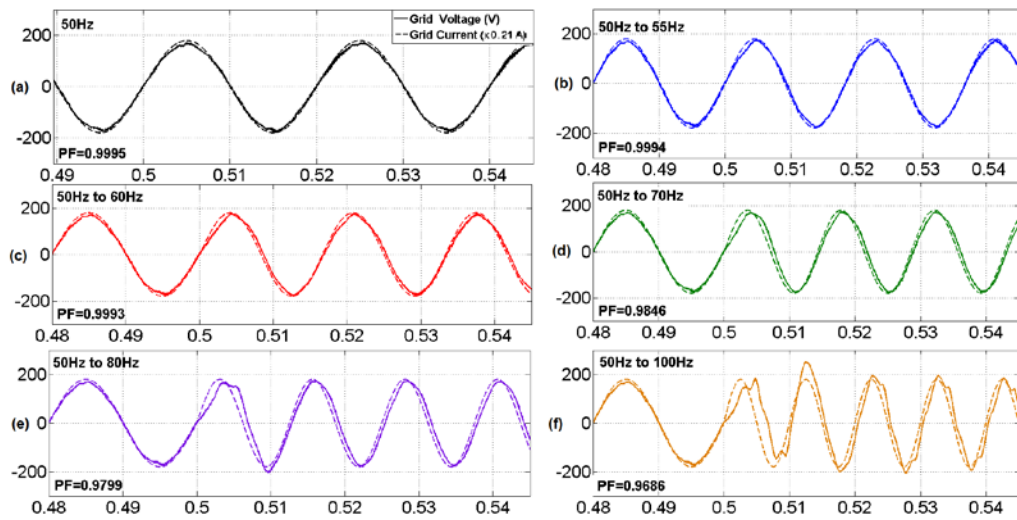
Figure 3.14. Voltage and current at phase 1 during a step of the nominal frequency. (a) No step of frequency is exerted. (b) Step of 5Hz. (c) Step of 10Hz. (d) Step of 20Hz. (e) Step of 30Hz. (f) Step of 50Hz.

The synchronization of the voltage and current at phase 1 before and after the step of frequency of 50Hz to 55Hz and 50Hz to 60Hz is perfectly attained and a FP of 0.99 is obtained. Certain degradation of the PF occur when the steps of 50Hz to 70Hz, 50Hz to 80Hz and 50Hz to 100Hz occur with the corresponding decrease of

the power factor to 0.98, 0.97 and 0.96, respectively. Note that the power factors are higher than the specifications in the standards where a PF for PV system of at least 0.85 is suggested [73]. In addition, these frequency variations cannot occur in the real utility grid, but they have been exerted in order to evaluate the degradation of the power factor of the system when a PSD+dqPPL is used.

A summary of the power factors attained by the PSD+dqPLL synchronization algorithm when frequency variations occur is shown in Table 3.5, and they are compared with the suggested by the IEEE Std 929-2000 Standard [73].

Table 3.5. Power Factor degradation due to frequency variations for a PSD+dqPLL synchronization algorithm.

Step of frequency (Hz)	Power Factor (PF)	Power Factor IEEE Std 929-2000
0	0.9995	>0.85
5	0.9994	>0.85
10	0.9993	>0.85
20	0.9846	>0.85
30	0.9799	>0.85
50	0.9686	>0.85

3.6.2 Testing the influence of Harmonic Distortion

The 5th and 7th harmonics are introduced in the 3-phase utility grid voltages with an amplitude distortion of 25% as can be observed in Figure 3.15a. The frequency and phase detection by the synchronization algorithms are shown in Figure 3.15b: by one hand, a poor frequency and phase detection can be observed when the dqPLL (trace in blue), the PSD+dqPLL (trace in green), the DSOGI-PLL (trace in red), and the DSOGI-FLL (trace in orange) are used to estimate the frequency; on the other hand, a significant difference can be observed when the MSOGI-FLL (trace in black) is used. This good performance of the MSOGI-FLL algorithm

when the utility grid is affected by harmonic pollution is due to the use of a Harmonic Decoupled Network (HDN) and that a DSOGI is used for each harmonic. The drawback of the MSOGI-FLL is that a sophisticated structure is necessary to implement it yielding to a high computational burden.
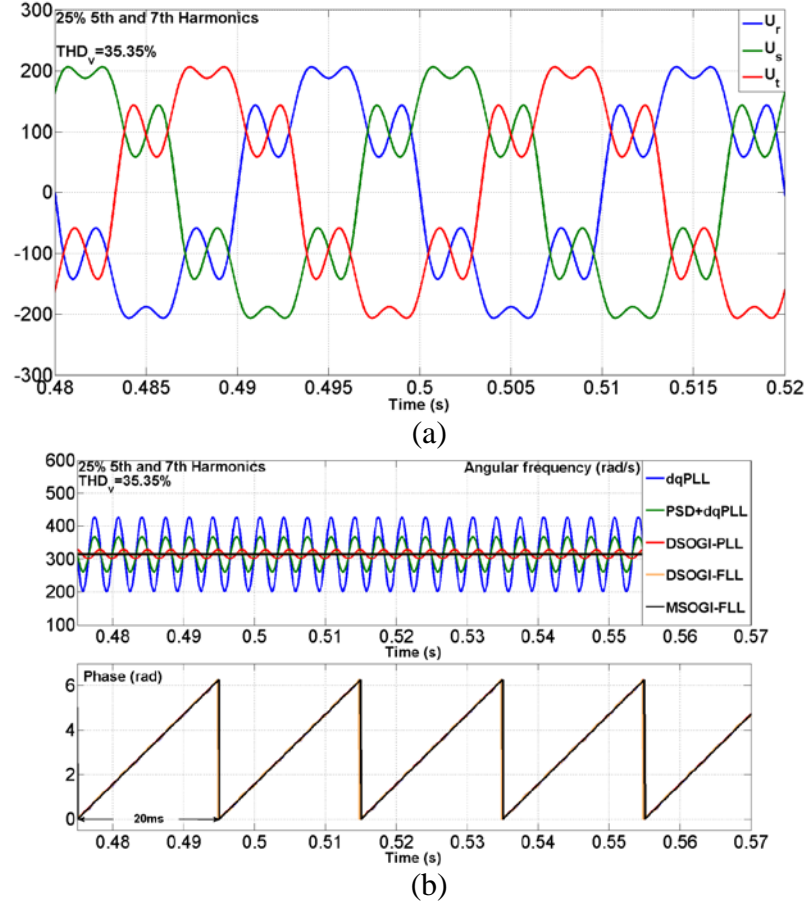
Figure 3.15. (a) Utility grid voltages (U_r=187.79 = V_{peak} = U_s = U_t) affected with 25% pollution in magnitude of the 5th and 7th harmonics. (b) Time evolution of the angular frequency and phase detection when a magnitude distortion of 25% in the 5th and 7th harmonics in the 3-phase utility grid voltages is present.

3.6.3 Testing the influence of the Voltage Unbalances

In order to analyze the response of the synchronization algorithms when voltage unbalances occur in the low-voltage 3-phase utility grid a voltage unbalance for a

ground fault in phase 3 is performed on the 3-phase utility grid as can be observed in Figure 3.16a.

(a)

(b)
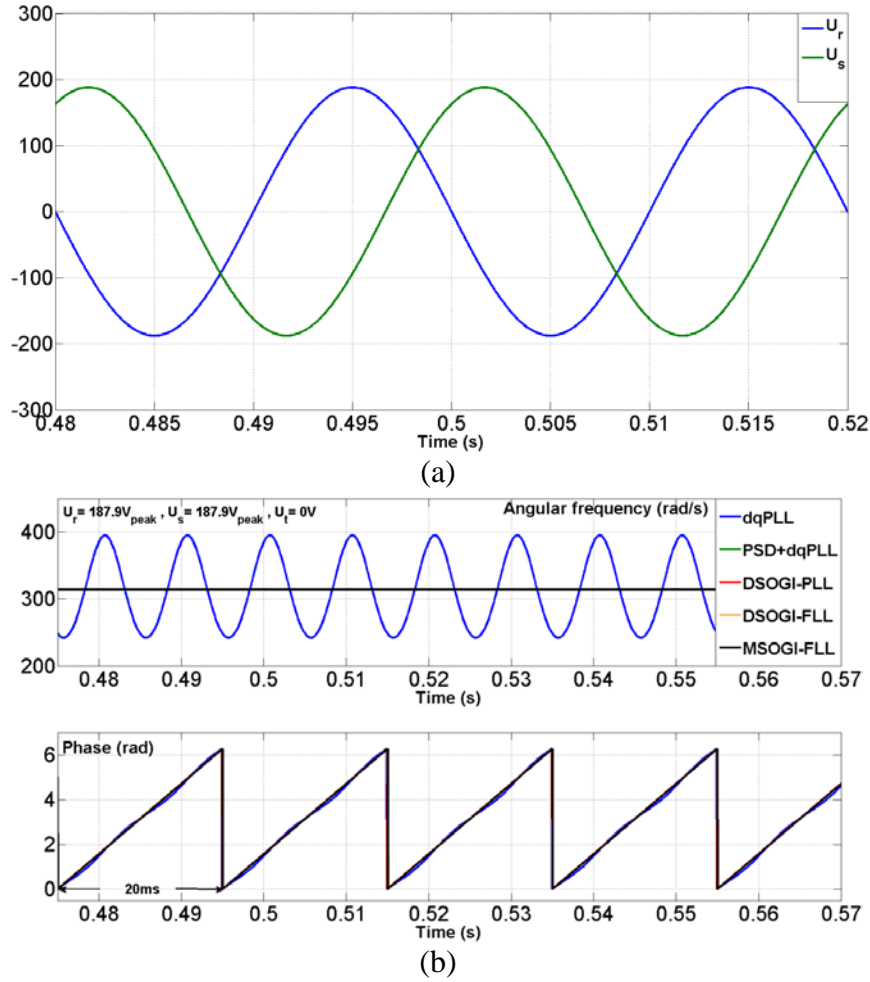
Figure 3.16. (a) Utility grid voltages (U_r=187.9V_peak U_s=187.9Vpeak U_t=0V, respectively). (b) Time evolution of the detected frequency and phase when voltage unbalances occur in the 3-phase utility grid.

Figure 3.16b shows the time evolution of the detected frequencies and phases by the five synchronization algorithms for a ground fault in phase 3. When using the dqPLL method, it can be observed the presence of the 2nd order harmonic in the detected frequency with blue trace in Figure 3.16b, being this issue the main drawback of the dqPLL synchronization algorithm. This

situation has been overcome by adding a PSD block in the case of the PSD+dqPLL or a PSC in the case of the DSOGI-PLL, the DSOGI-FLL and the MSOGI-FLL algorithms, where optimal frequency detection is attained (2nd order harmonic free) as can be seen in Figure 3.16b.

3.7 Real-time digital simulation

In order to support the results obtained with simulations, a series of real-time digital simulations have been carried out using the configuration of the real-time platform shown in Figures 1.10 and 1.11.

3.7.1 Real-Time Test of the influence of the nominal frequency variation

The first Real-Time digital test that is performed is a step of frequency from 50Hz to 60Hz. The responses of the synchronization algorithms are shown in Figure 3.17a. Acceptable frequency detection is attained by the dqPLL when a frequency step of 50 to 60Hz is exerted (Figure 3.17a1). In the case of the PSD+dqPLL it is possible to observe that its response is similar to the response of the dqPLL, but the PSD block has a discrete filter which is very sensitive to the variation of the nominal frequency of the utility grid, and may lead to the power factor degradation of the inverter-grid connection (Figure 3.17a2). The frequency detection by the DSOGI-PLL is attained but it can be seen an overshoot and certain fluctuations when the step of frequency is exerted as can be seen in Figure 3.17a3. Perfect frequency detection is attained when the DSOGI-FLL (Figure 3.17a4) and the MSOGI-FLL (Figure 3.17a5) are used due to the use of a Frequency-Locked Loop (FLL), allowing good dynamics.

1 (dqPLL)

1 (dqPLL)

2 (PSD+dqPLL)

2 (PSD+dqPLL)

3 (DSOGI-PLL)

3 (DSOGI-PLL)

4 (DSOGI-FLL)

4 (DSOGI-FLL)

5 (MSOGI-FLL)

5 (MSOGI-FLL)

(a)   (b)
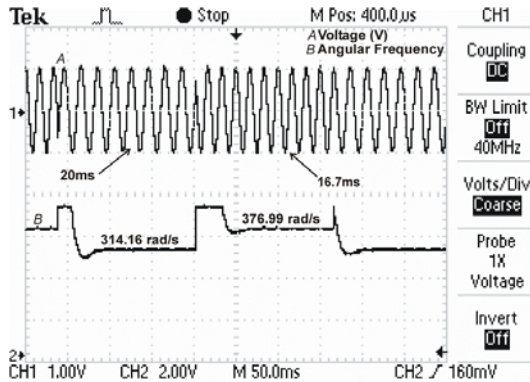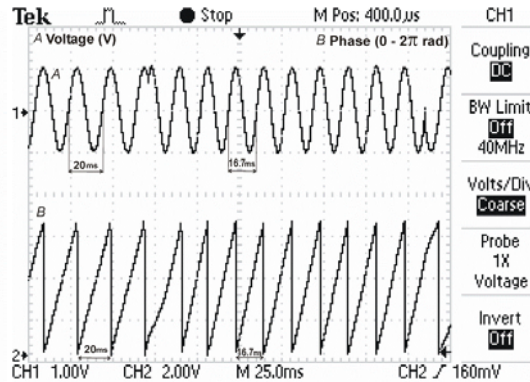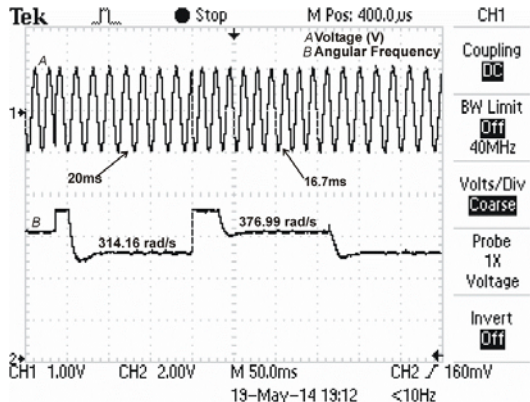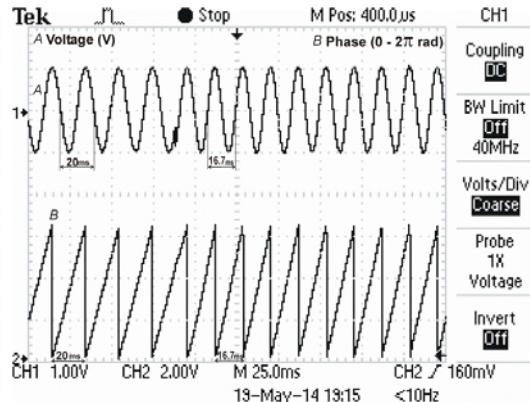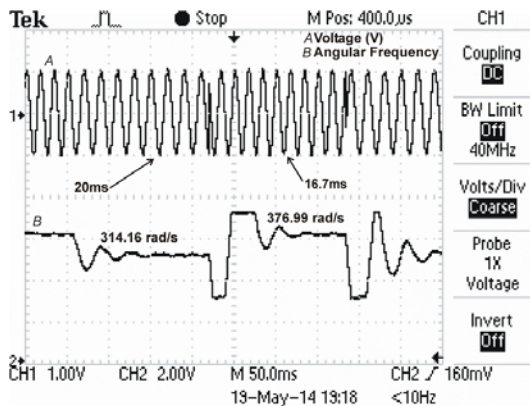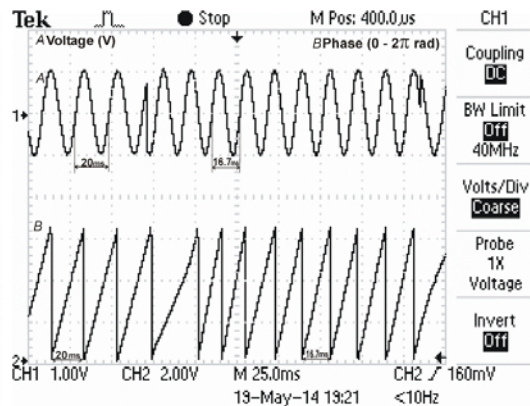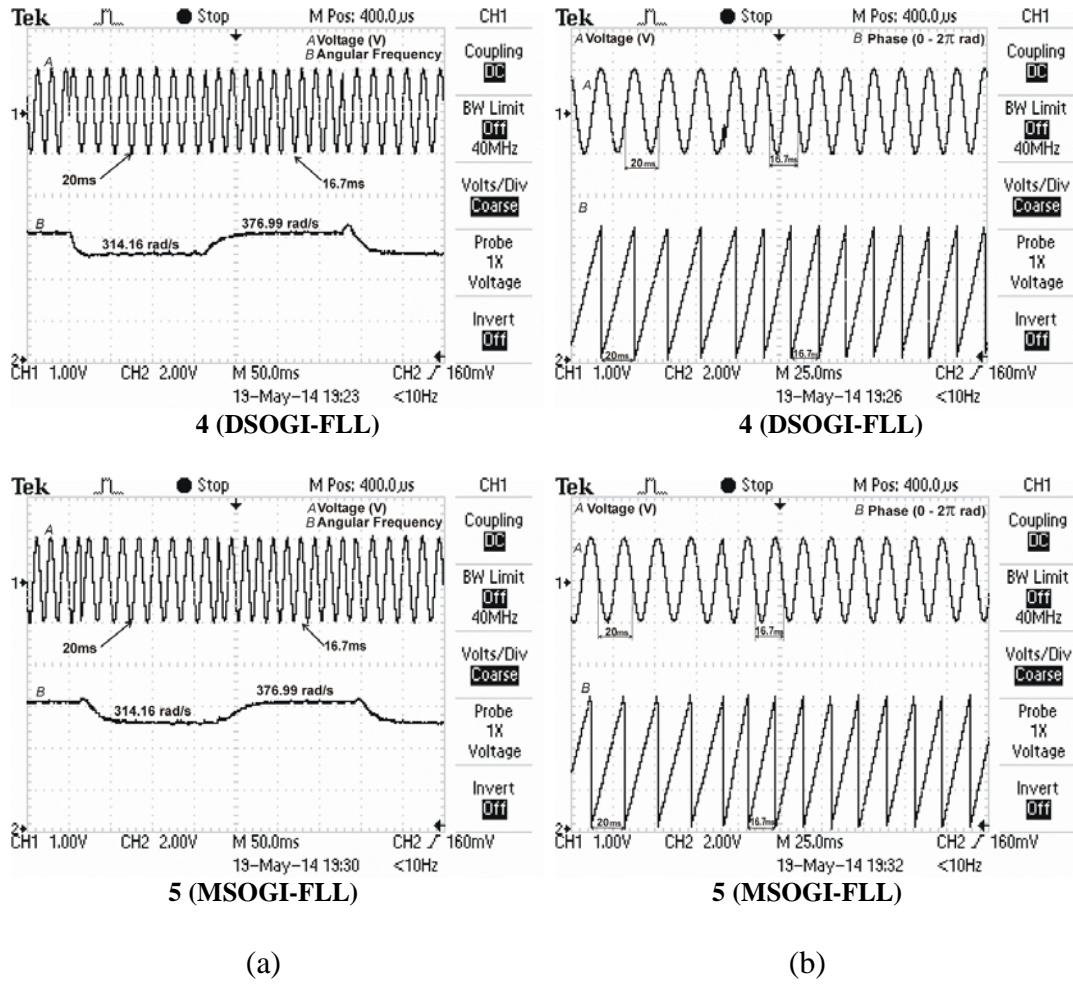
Figure 3.17. (a) Real-time evolution of the voltage at phase 1 and frequency detection by the synchronization algorithms when a step of frequency from 50Hz to 60Hz is exerted. (b) Real-time evolution of the voltage at phase 1and real-time phase detection when a step of frequency from 50Hz to 60Hz is exerted.

The phase detection by the synchronization algorithms are shown in Figure 3.17b and as can be observed all synchronization algorithms are capable to detect the phase when a step of frequency from 50Hz to 60Hz is exerted.

61

3.7.2 Real-Time Test of the influence of the Harmonic Distortions

In this second test, the 5th and 7th harmonics are introduced in the 3-phase utility grid voltages with an amplitude distortion of 25%. The frequency and phase detection by the synchronization algorithms are shown in Figure 3.18.

The frequency detection by the synchronization algorithms is shown in Figure 3.18a. A poor harmonic attenuation can be observed in the detected frequency when using the dqPLL, the PSD+dqPLL, the DSOGI-PLL and the DSOGI-FLL synchronization algorithms. When using only the dqPLL (Figure 3.18a1), the 6th harmonic in the detected frequency can be observed due to the application of the Park transformation of the 3-phase voltages, which transforms the 5th (negative sequence) and the 7th (positive sequence) harmonics into the 6th harmonic in d-q components (rotating at the fundamental angular speed). When using the PSD block together with the dqPLL, a certain attenuation of the 6th harmonic is observed in Figure 3.18a2 because of the contribution of the negative sequence 5th harmonic is removed by the PSD block, only allowing the contribution of the positive sequence 7th harmonic. Similar attenuation can be observed when the DSOGI-PLL and the DSOGI-FLL are used due to the use of the PSC block.

Finally, when using the MSOGI-FLL, almost perfect frequency detection can be observed in Figure 3.18a5: this good detection under harmonics influence is achieved because of the use of a Harmonic Decoupled Network (HDN).

The phase detection by the synchronization algorithms is shown in Figure 3.18b: the synchronization algorithms capable of obtaining good phase estimation when low-order harmonics are present in the low-voltage 3-phase utility grid are the DSOGI-PLL (Figure 3.18b3) and the MSOGI-FLL (Figure 3.18b5) algorithms due to the use of the Harmonic Decoupled Network (HDN) and that a DSOGI for each one of the harmonics present in utility voltage is used, in the case of the

MSOGI-FLL. In the case of the DSOGI-PLL, this good phase detection under harmonic pollution is due to the combination of the SOGI filters used in the DSOGI part and the PI filter used in the PLL part.

1 (dqPLL)

1 (dqPLL)

2 (PSD+dqPLL)

2 (PSD+dqPLL)

3 (DSOGI-PLL)

3 (DSOGI-PLL)

4 (DSOGI-FLL)   4 (DSOGI-FLL)

5 (MSOGI-FLL)   5 (MSOGI-FLL)

(a)   (b)
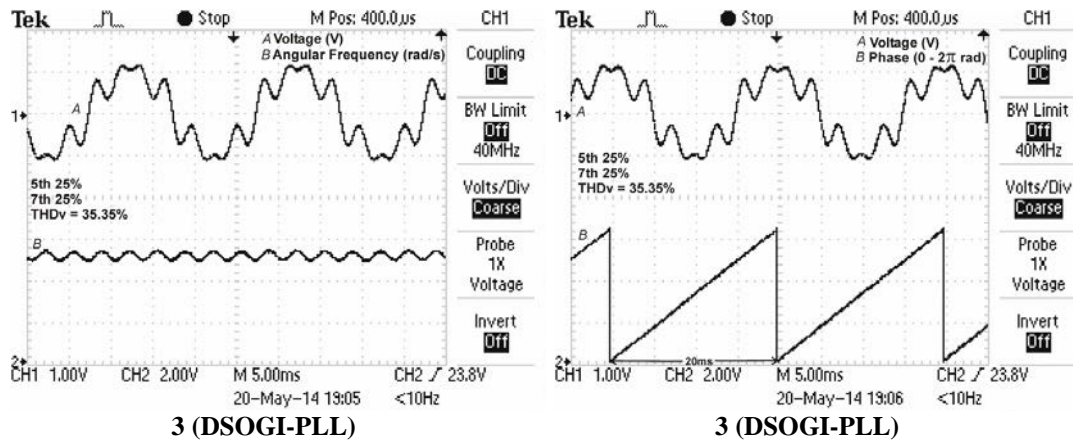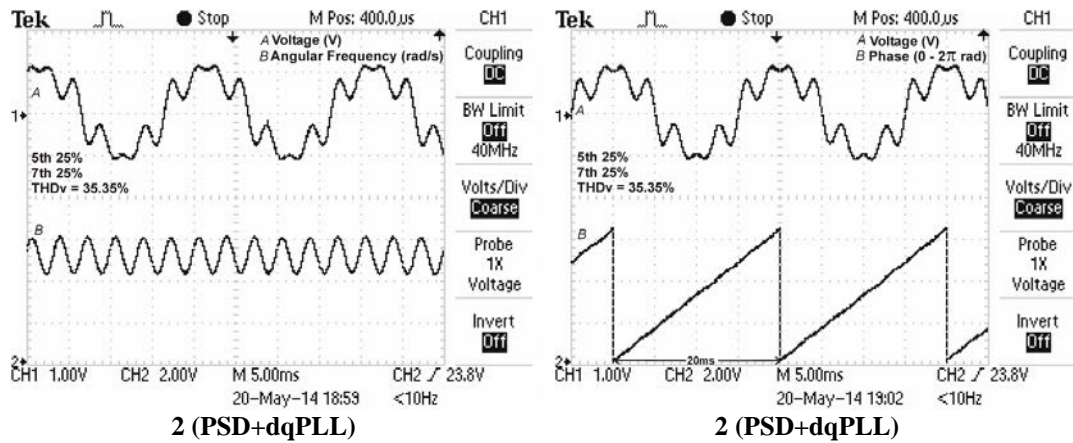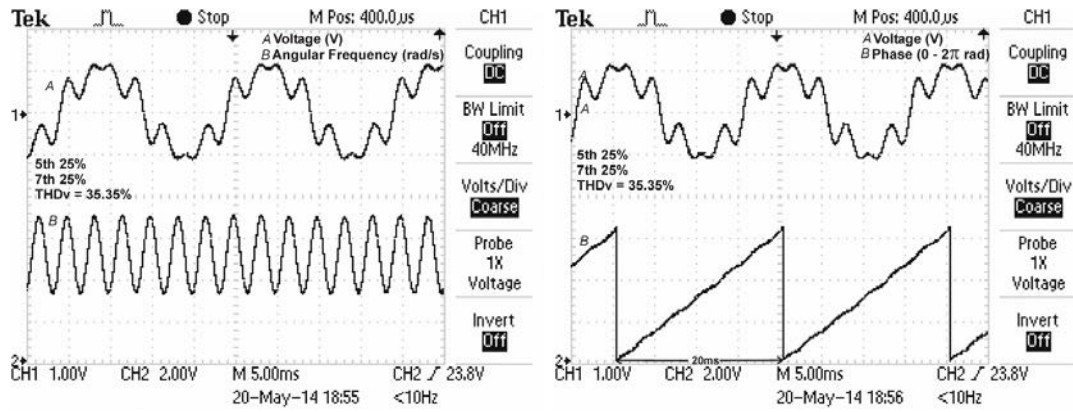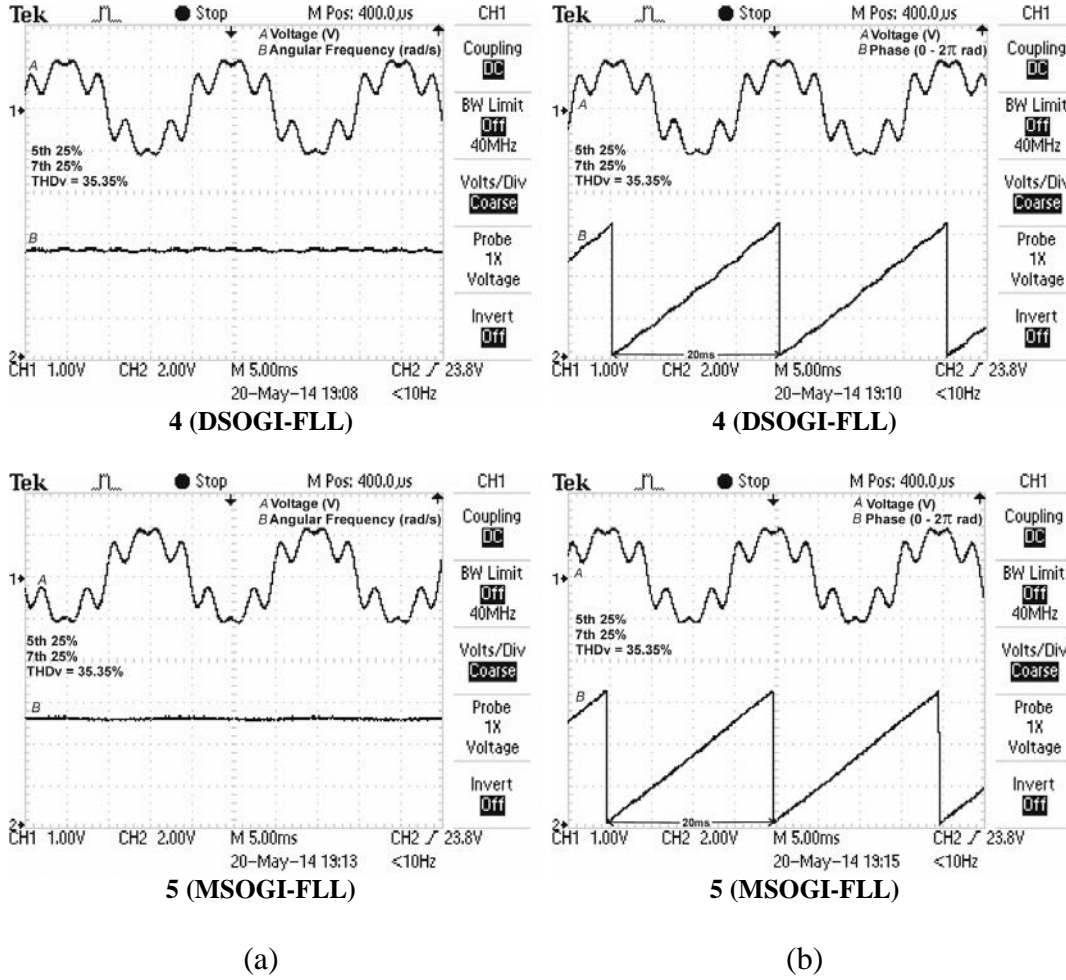
Figure 3.18. (a) Real-time evolution of the voltage at phase 1 and frequency detection by the synchronization algorithms when a magnitude distortion of 25% in the 5th and 7th harmonics in the 3-phase utility grid voltages is present. (b) Real-time evolution of the voltage at phase 1 and real-time phase detection when a magnitude distortion of 25% in the 5th and 7th harmonics in the 3-phase utility grid voltages is present.

3.7.3 Real-Time Test of the influence of the Voltage Unbalances

In order to analyze the response of the synchronization algorithms when voltage unbalances occur in the low-voltage 3-phase utility grid, Figure 3.19 shows the time evolution of the real-time frequencies and phases detection obtained by the synchronization algorithms when voltage unbalances (modeled as $U_r=187.9V_{peak}$ $U_s=187.9V_{peak}$ $U_t=0V$, respectively) occur in the 3-phase utility grid. When

using the dqPLL method, it can be observed the presence of the 2nd order harmonic in the detected frequency and phase (See Figures 3.19a1 and 3.19b1), being the main drawback of the dqPLL. This is solved by adding the PSD block, in which acceptable frequency detection is attained (2nd order harmonic free). In the case of the DSOGI-PLL, the DSOGI-FLL and the MSOGI-FLL, the positive sequence component of the frequency and the phase are detected due to the use of the PSC block.

1 (dqPLL)

1 (dqPLL)

2 (PSD+dqPLL)

2 (PSD+dqPLL)

3 (DSOGI-PLL)   **3 (DSOGI-PLL)**

4 (DSOGI-FLL)   **4 (DSOGI-FLL)**

5 (MSOGI-FLL)   **5 (MSOGI-FLL)**

(a)   (b)
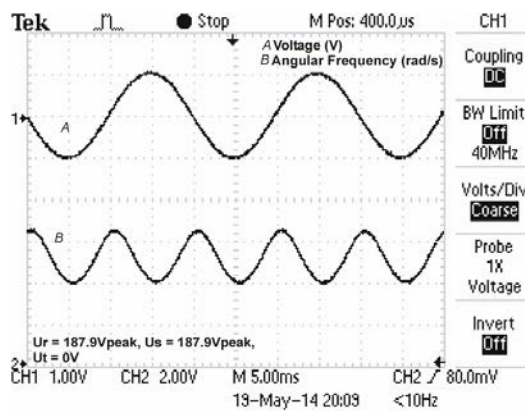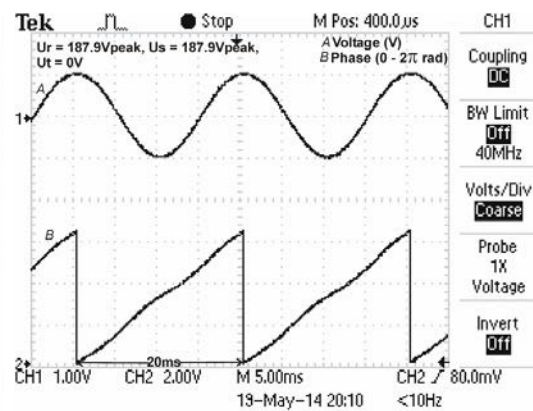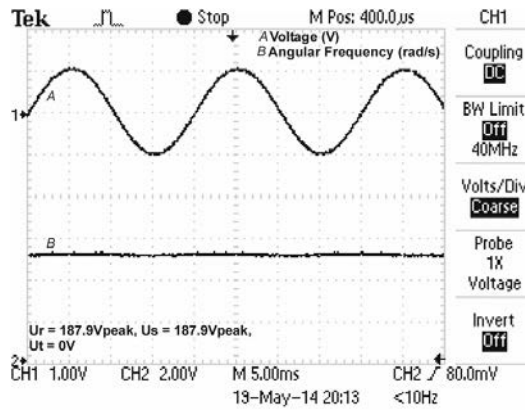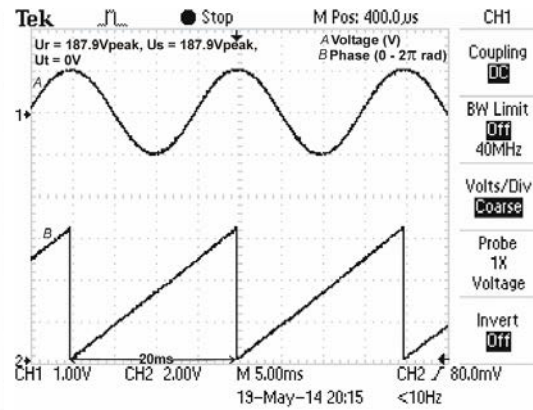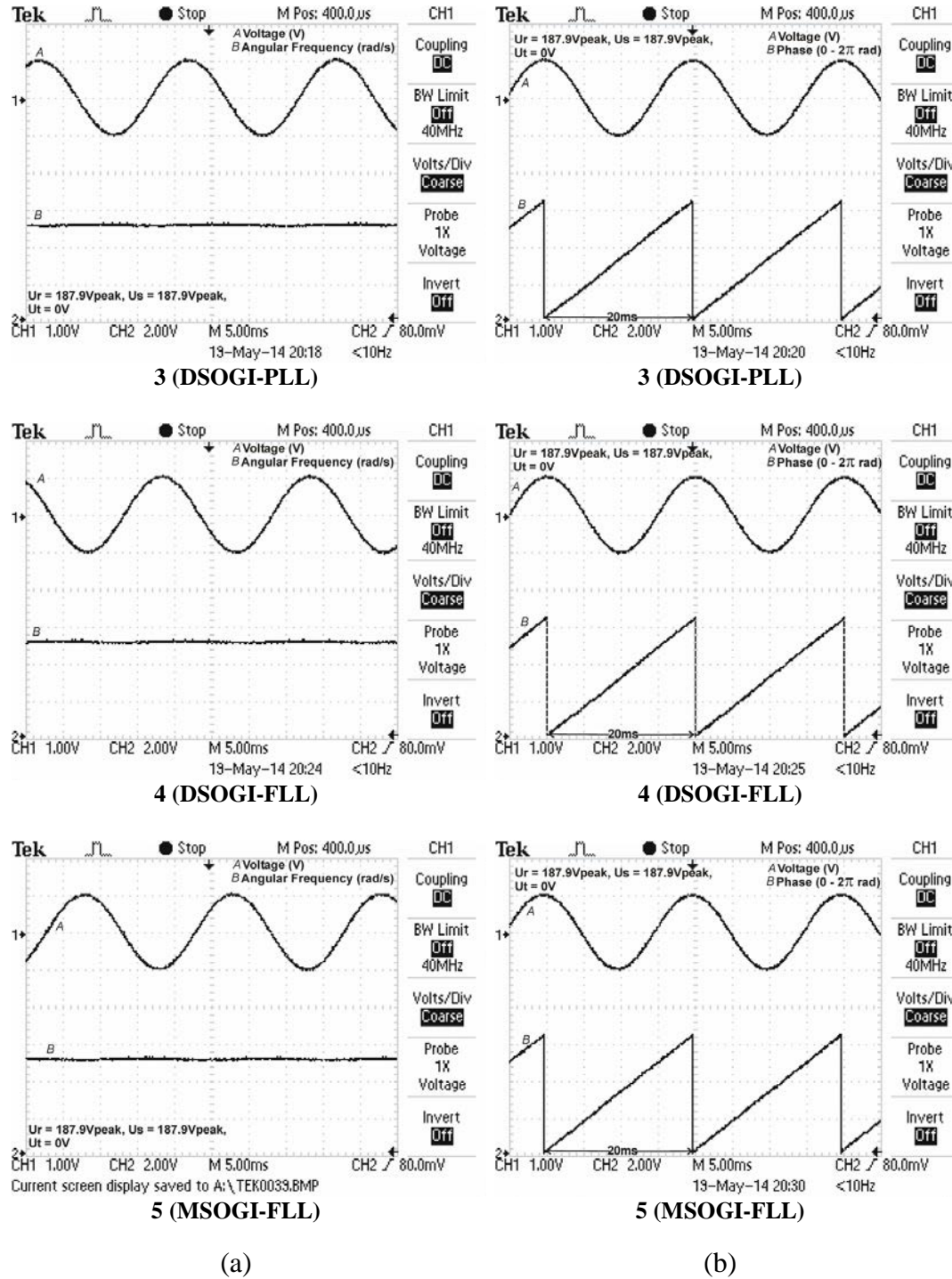
Figure 3.19. (a) Real-time evolution of the voltage at phase 1 and frequency detection by the synchronization algorithms when a voltage unbalances occur. (b) Real-time evolution of the voltage at phase 1and real-time phase detection when a voltage unbalances occur.

66

Finally, a summary with a comparative study of the synchronization algorithms is shown in Table 3.6.

Table 3.6. Comparative studies of the Synchronization Algorithms.

NAME	STRONG POINT	WEAK POINT
dqPLL	Simplicity, Frequency Variations	Harmonic, Voltage Unbalances
PSD+dqPLL	Voltage Unbalances	Frequency variations, Harmonics
DSOGI-PLL	Frequency Variations, Voltage Unbalances	Harmonics
DSOGI-FLL	Frequency Variations, Voltage Unbalances	Harmonics
MSOGI-FLL	Harmonics, Frequency Variations, Voltage Unbalances	Sophisticated structure

3.8 Conclusions

This Chapter has shown several synchronization algorithms that are used in grid-connected renewable agents. The algorithms were studied using MATLAB/SIMULINK simulation techniques and by using a Real Time Digital Simulator Platform.

The behaviours of the synchronization algorithms were analyzed when the 3-phase utility grid voltage was affected by the influence of a frequency variation where a step from 50Hz to 60Hz was exerted, harmonic distortions by introducing 25% pollution in the magnitude of the 5th and 7th harmonics of the utility grid voltages and finally when voltage unbalances occur in the 3-phase utility grid due to a ground fault in phase 3.

An important aim was to make a comparative summary where the strong and weak points of each synchronization algorithm are shown. After a detail analysis carried out to the five synchronization algorithms, it can be said that the most complete and reliable synchronization algorithm is the MSOGI-FLL, although a sophisticated structure is necessary yielding to a higher computational burden.

CHAPTER 4
Current-Control Strategies for Grid-Connected Inverters

Since the control algorithm is an essential part of a grid-connected inverter, two current-control strategies are deeply studied in this Chapter. The first control strategy to be treated is the Synchronous Reference Frame Control (d-q control) which makes use of Proportional Integral (PI) regulators. Then the Stationary Reference Frame Control ($\alpha\beta$ control) is analyzed. Unlike the d-q control which uses PI regulator, in the $\alpha\beta$ control the control strategy is performed by using PR controllers.

In addition to study the d-q and the $\alpha\beta$ control strategies, a Harmonic-Compensator structure is discussed in this Chapter.

In order to validate the control strategies and the Harmonic-Compensator structure, some simulations using MATLAB/SIMULINK from The MathWorks, Inc. are shown firstly, and secondly, some real-time digital simulations are carried out.

4.1 Synchronous Reference Frame Control (d-q control)

The configuration of a d-q control strategy is shown in Figure 4.1. This is formed by the power and the control subsystm where PI regulators are used in the inner control loop. Following this control loop is explained.
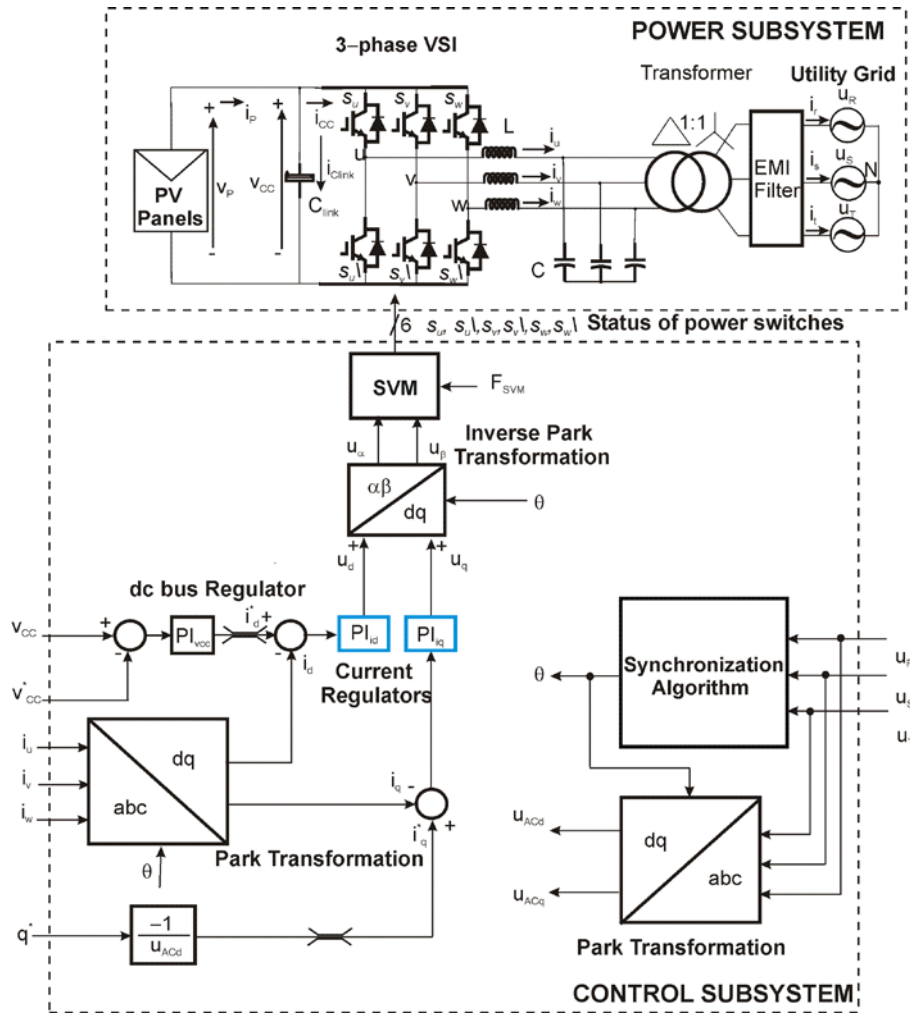
Figure 4.1. Block diagram of the Power and Control Subsystems for the 3-phase grid-connected PV system using a d-q control strategy.

The inner control loop uses two PI controllers to regulate the d-q components of the line currents allowing the synchronization of the 3-phase inverter line currents

with the 3-phase utility grid voltages. By using the Park transformation [46], the sensed 3-phase inverter currents are transformed into a reference frame (abc->dq or according to Figure 4.1: i_U, i_V, i_W into i_d and i_q) which rotates synchronously with the voltage vector of the utility grid [33]. According to this transformation, the d-q components of the 3-phase inverter currents are dc signals, making possible the use of PI regulators in the control strategy for zero error behaviour at steady state.

As can be observed in Figure 4.1, the output of the dc regulator is used as the reference signal of the d component of the current ($i_d{}^*$) which is compared with the measured d component of the line current of the inverter (i_d). This d component is used to regulate the active power (p) injected to the utility grid. For a zero reactive power (q) injected to the utility grid, its corresponding current reference $i_q{}^*$ is set to zero; on the contrary, if a desirable quantity of reactive power is to be injected to the utility grid, a specific value of $i_q{}^*$ should be imposed [33].

The constants of the PI regulators (K_{Ii} and K_{Pi}) used in the inner loop for the d-q components of the currents can be calculated by making a frequency analysis and using Eq. 4.1 [17,50]:

$$
\begin{cases}
\dfrac{K_{Ii}}{K_{Pi}} = \dfrac{\omega_{cl}}{\tan\left[-90° + PM_I + \tan^{-1}\left(\omega_{cl}\dfrac{L}{R}\right)\right]} \\[4ex]
K_{Pi} = \dfrac{FSR}{K_{INV}}\dfrac{R}{G_{TI}}\sqrt{\dfrac{1+\left(\omega_{cl}\dfrac{L}{R}\right)^2}{1+\left(\dfrac{1}{\omega_{cl}}\dfrac{K_{Ii}}{K_{Pi}}\right)^2}}
\end{cases}
\qquad \text{(Eq. 4.1)}
$$

where ω_{cl} is the crossover angular natural frequency of the inner loop and under the suggestion of [17] should be one order of magnitude smaller than the switching frequency F_{sw}, PM_I is the phase margin, $\tau = L/R$ is the time constant, *FSR* is the full scale range of the ADC which for simulation is set to 1, $K_{INV} = \frac{2}{3}V_{cc}$ is the gain of the inverter, G_{TI} is the gain of the current transducer which for simulations is set to 1[17].

A block diagram of the continuous equivalent small-signal model of the cascaded control for the 3-phase VSI used for PV systems is depicted in Figure 4.2 and, as can be observed, the effect of the computing delays is not taking into account because the tests of the algorithms are carried out in a simulation environment, being $\omega L i_q$ and $-\omega L i_d$ the cross-term perturbations, and u_{ACd} the utility grid perturbation [49].
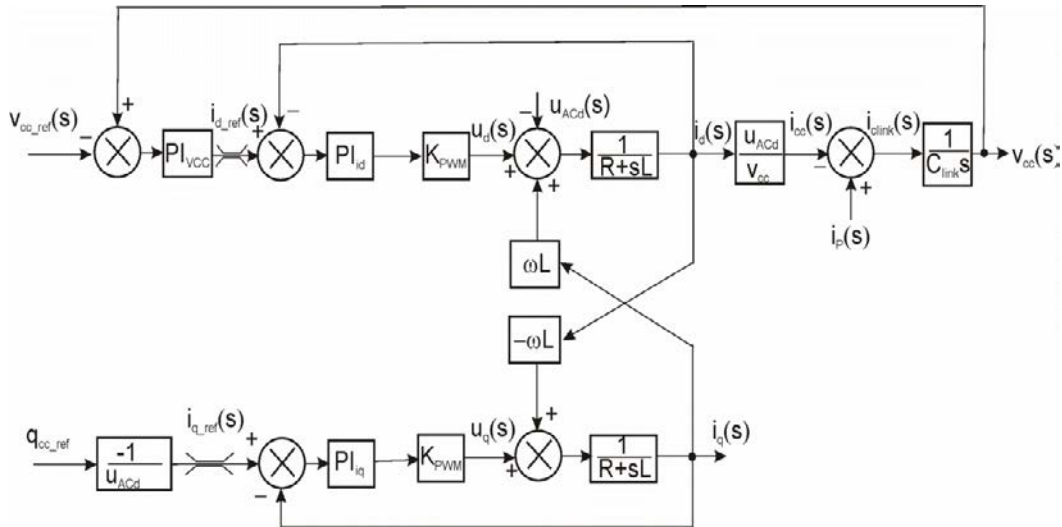
Figure 4.2. Block diagram of the continuous equivalent small-signal model of the cascaded control for the 3- phase VSI for PV systems.

Figure 4.3 shows a Bode plot of the open loop gain for the inner current loop and the used plant with the parameters shown in table 3.3. As can be seen, the chose

72

crossover frequency of 1220.8Hz leads to a stable control system with a Phase Margin of 63.5º.
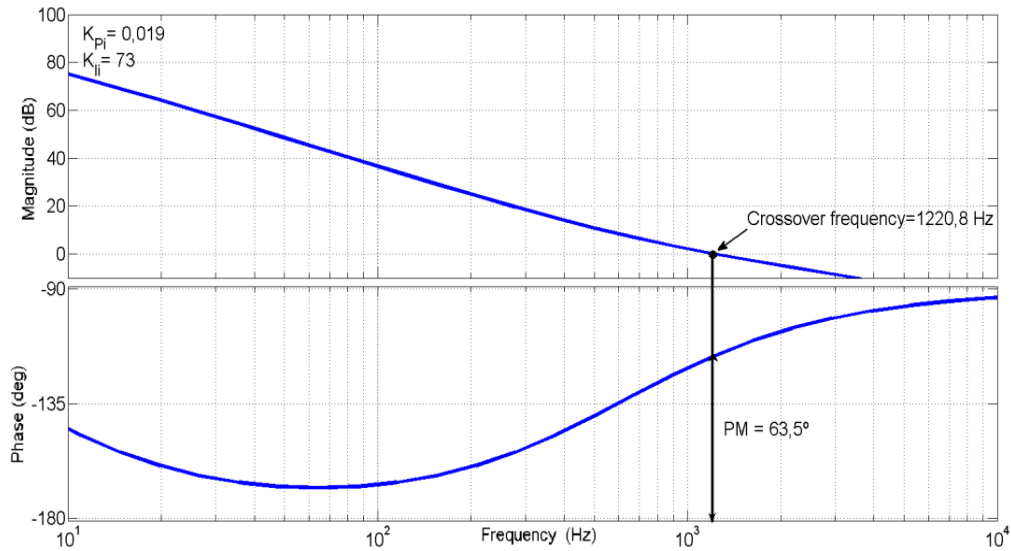
Figure 4.3. Bode plot of the open loop gain of the PI regulator + the plant.

4.2   Stationary Reference Frame Control (PR control)

A grid-connected configuration for a PV generator is shown in Figure 4.4, the control strategy is based on the use of Proportional-Resonant (PR) controllers and its cascaded control block diagram for the small-signal model is shown in Figure 4.5.

Classical PI regulators produce zero steady-state error for dc signals due to its integral part. In a similar way, when sinusoidal signals are to be regulated, Proportional-Resonant (PR) regulators must be used for zero steady-state error behaviour instead.

In the Stationary Refrence Frame Control (PR control), a Clarke transformation (abc->$\alpha\beta$) of the 3-phase line currents is carried out and sinusoidal $\alpha\beta$ components are obtained. Then, two Proportional-Resonant (PR) controllers are

used for both in the inner control loop, allowing the synchronization of the 3-phase inverter line currents with the 3-phase utility grid voltages, and avoiding the non-zero stady-state error if PI controllers were used.

The ideal Proportional-Resonant transfer function is described by Eq. 4.2 which has an infinite gain at the frequency ω_0 and no gain or phase shift at other frequencies [74]:

$$G_{PR}(s) = K_P + \frac{2K_I s}{s^2 + \omega_0^2}$$

(Eq. 4.2)

where K_P is the Proportional gain, K_I is the integral gain, and ω_0 is the resonance angular frequency of the controller.
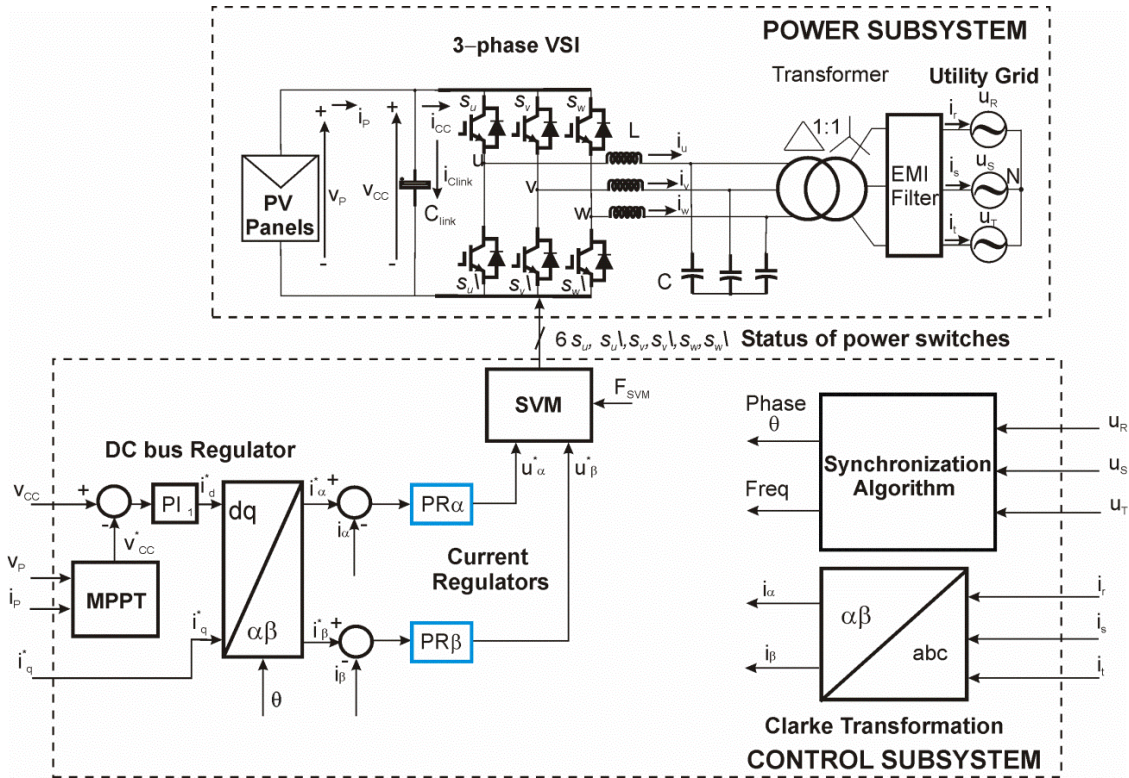
Figure 4.4. Block diagram of the Power and Control Subsystems for the 3-phase grid-connected PV system using PR controllers**.**
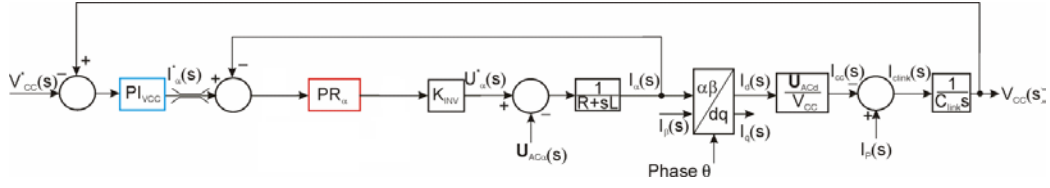
Figure 4.5. Block diagram of the small-signal model of the cascaded control.

The ideal PR has an infinite gain within a narrow bandwidth around the resonance frequency ω_0, which may lead to stability and digital implementation problems. Adding the cut-off frequency ω_c, as a new term to Eq. 4.2, leads to a non-ideal PR with finite gain and an improved transient response [74], solving the stability problems and making easier the digital implementation. The transfer function of the non-ideal PR Controller is shown in Eq. 4.3.

$$G_{PR}(s) = K_P + \frac{2K_I\omega_c s}{s^2 + 2\omega_c s + \omega_0^2} \tag{Eq. 4.3}$$

The dynamic of the system in terms of bandwidth, phase and gain margin will depend of the proportional gain K_P [75] which is adjusted in a similar way as it is tuned in a PI controller; the stady-state error will depend of the integral gain K_I whose value will be selected comparatively high, but holding the limits for stability [74]. The second term of Eq. 4.2 can be viewed as a Generalized Integrator (GI) [68].

A bode plot of Eq. 4.2 is shown in Figure 4.6 for $K_P = 0.019$, $\omega_0 = 314.16$rad/s and $K_I = 10$. It can be seen the very high gain around ω_0.

In order to assure a good transient response with minimum steady-state error, an adequate cut-off frequency ω_c must be chosen for the non-ideal PR controller. For this, several Bode plots of Eq. 4.3 are shown in Figure 4.7 for $K_P = 0.019$, $\omega_0 = 314.16$rad/s, $K_I = 10$ and $\omega_c = 1$rad/s, 10rad/s and 20rad/s. The upper zone of

Figure 4.7 shows that finite gain is achieved for all ω_c, meanwhile the increment of ω_c increases the bandwidth which can help to obtain a certain tolerance in order to support a small variation of the nominal frequency, but at the same time, avoiding the negative influence of the low-order harmonics not involved in the PR controller behaviour if a high value of ω_c were used. Then, ω_c =1rad/s is chosen because the resonant filter will be more selective in frequency with a high harmonic rejection.
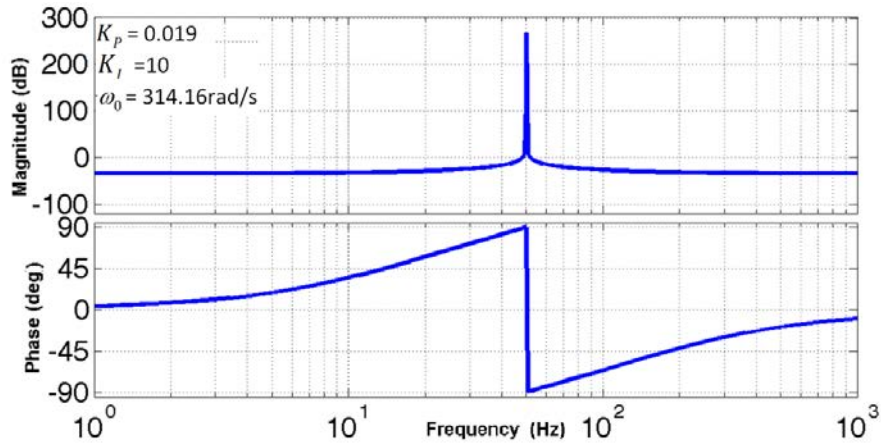
Figure 4.6. Bode plot of an ideal PR controller.
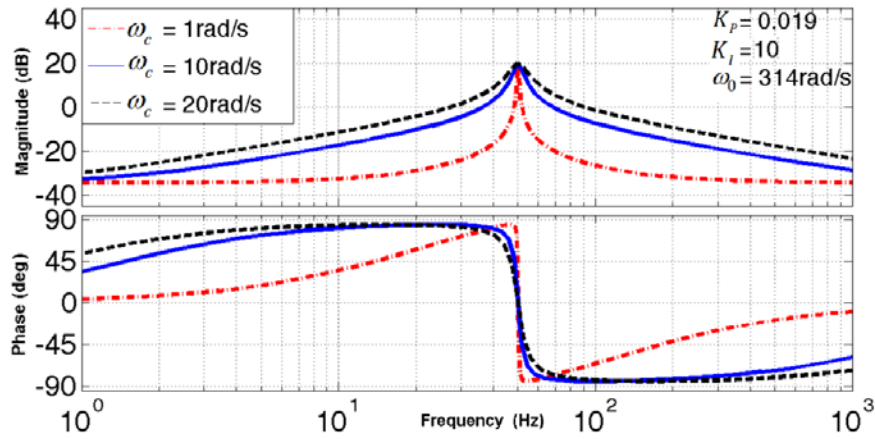
Figure 4.7. Bode plot of non-ideal PR controller using several values for ω_c.

4.3 Harmonic-Compensator

When the low-order frequency harmonics (5th, 7th, 11th, 13th, 17th, 19th, etc.=$6n\pm1$, n=1,2,3,…) distortions perturb the utility grid voltage, the controlled line currents of the inverter will also be distorted as well, reducing the power quality of the inverter-grid connection, unless a harmonic compensation strategy were used.

In [76] [77], a Voltage Source Inverter (VSI) working as a shunt active filter is proposed as a harmonic compensator scheme at the point of common coupling (PCC) of the distribution 3-phase line voltages and nonlinear loads: in this, the 3-phase line currents of the inverter are controlled in the Synchronous Reference frame (SRF) (abc->dq transformation needed) so as to feed 3-phase "pure" sinusoidal currents into the utility grid; however, this type of harmonic compensator behaves as a feedforward open-loop control which is affected, essentially, by the line currents control delay and the harmonic cancellation cannot be done completely. If some low-pass filter, with a cutoff frequency that produces a leading phase equal to the currents delay, is employed to sense the currents, the delay effect can be reduced [78]. The same idea is exposed in [79], where a Stationary Reference frame approach is used.

In order to overcome the effect of the delay effect, a closed-loop harmonic compensation (HC) structure in the SRF is described in [78], allowing a total compensation of selected harmonic currents. However, this approach involves an extremely complex structure needed for the positive and negative sequence of each harmonic to be compensated and, consequently, a high computational burden is required, unless the control of the 3-phase currents and the harmonic compensation were exerted in the Stationary Reference frame (abc->αβ transformation needed) [45].

The use of the Proportional-Resonant (PR) controller in the inner current loop opens the possibility of performing a harmonic compensator procedure with minimal computational burden in order to deliver a good power quality to the utility grid due to the absence of the cross coupling terms in the inner loop. This harmonic compensation is achieved by cascading multiple Genaralized Integrators (GI) which are tunned to resonate at specific low order frequencies [33]. In this thesis, as an example of this explanation, the 5th and 7th voltage harmonics will be introduced in the utility grid voltages, meanwhile, a harmonic-compensator structure for the 5th and 7th harmonics (shown in Figure 4.8) will be added to the inner current controller. The transfer function of a harmonic compensator [74] is described by Eq. 4.4.

$$G_h(s) = \sum_{h=5,7} \frac{2K_{ih}\omega_{ch}s}{s^2 + 2\omega_{ch}s + (h\omega_0)^2} \tag{Eq. 4.4}$$

where h is the harmonic to be compensated, ω_0 is the fundamental angular frequency and K_{ih} is the integral gain for harmonic h.
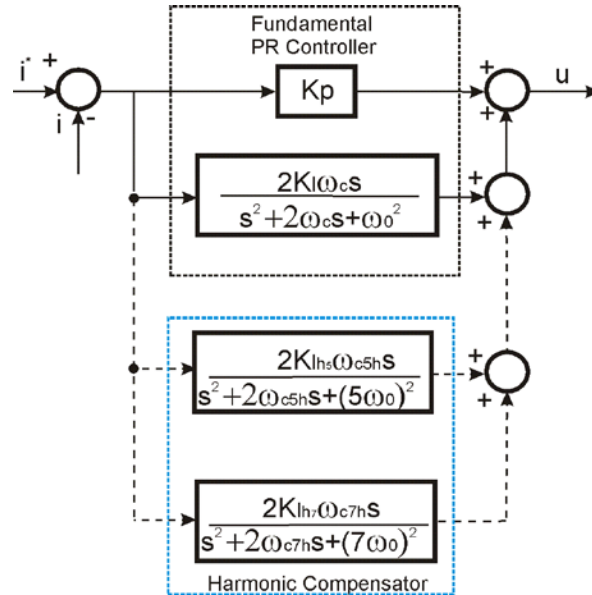
Figure 4.8. PR Controller + Harmonic Compensator structure.

78

It must be pointed out that the harmonic-compensator (HC) shown in Figure 4.8 does not affect the dynamics of the PR controller, because each filter block will work at its own resonance frequency.

The configuration of a PR-controller plus a HC structure is shown in Figure 4.9, in the same manner of Figure 4.4, but in this case the HC structures are added to the PR regulators. The cascaded control block diagram for the small-signal model is shown in Figure 4.10.
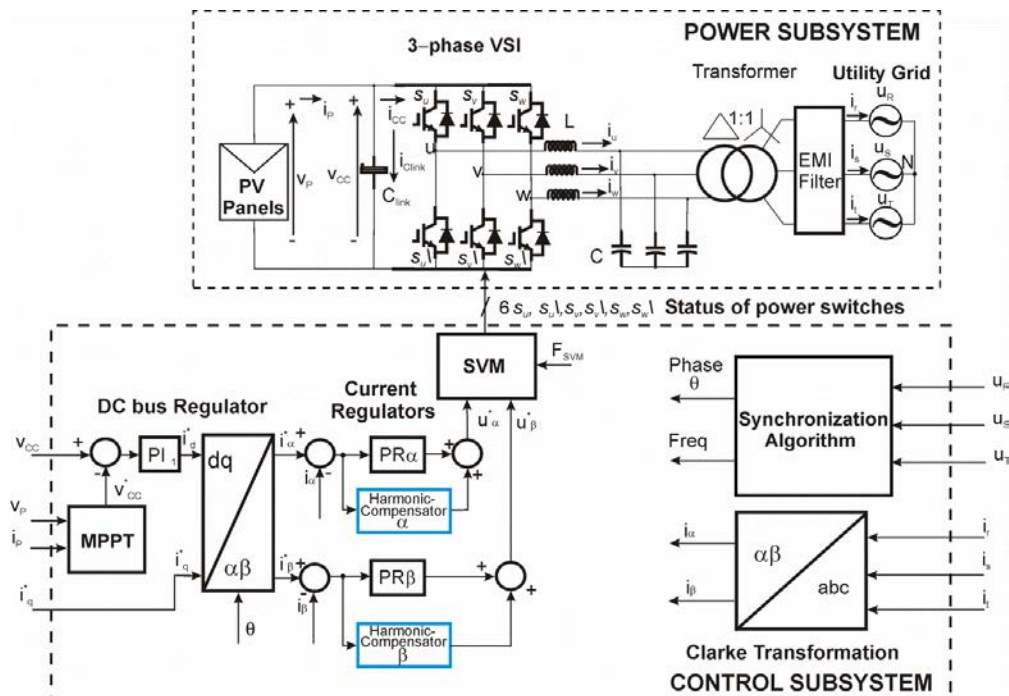
Figure 4.9. Block diagram of the Power and Control Subsystems for the 3-phase grid-connected PV system using a PR controller strategy plus a HC structure.
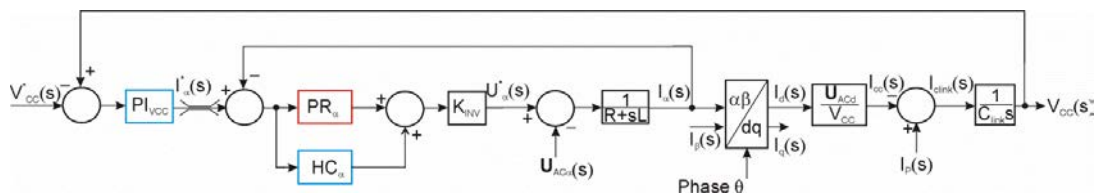
Figure 4.10. Block diagram of the small-signal model of the cascaded control used for the PR+HC control.

Adding the effect of the Harmonic Compensator (trace in red) described in Eq. 4.4, to the PR controller (trace in blue) described in Eq. 4.3, an extension of the previous analysis can be done for the influence of the low-order harmonics of the 3-phase utility grid voltages. In addition, the dynamic of the inner current loop (block diagram described in Figure 4.9 and the parameters shown in Tables 3.3 and 3.4) can be studied by taking into account the behaviour of its open loop Bode depicted in Figure 4.11, in which PM_I=63.5^o and a crossover frequency f_{cI}=1220.8Hz is set. The harmonic compensation is carried out by the effect of the resonant filters at $5f_0 = 250$Hz, and $7f_0$=350Hz.
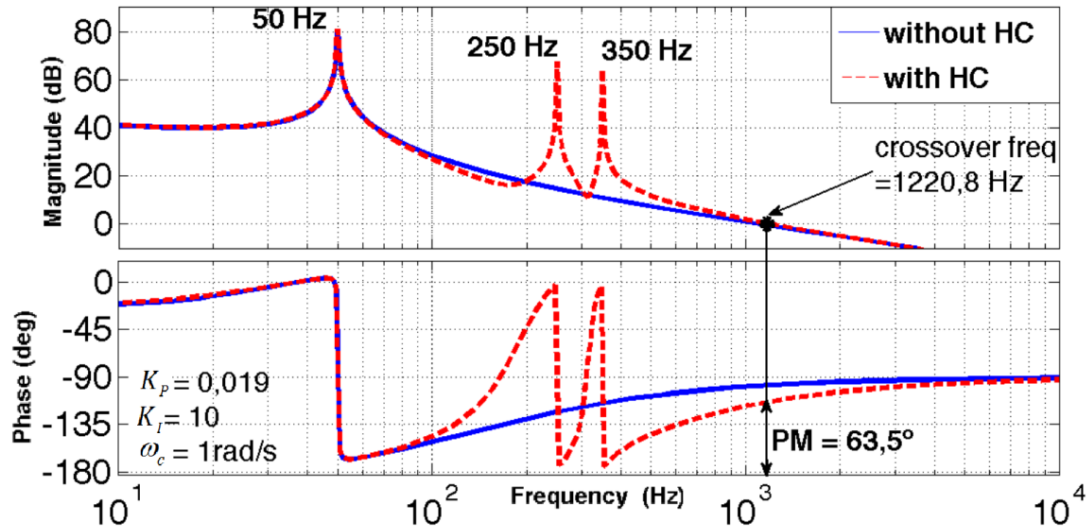
Figure 4.11. Open loop Bode plot of the PR Controller + Harmonic Compensator + Plant.

4.4 Simulations

Following, several MATLAB/SIMULINK simulations are carrying out in order to test the behaviors of the control algorithms studied in this Chapter.

4.4.1 d-q control

Figure 4.12a shows the SIMULINK [10] model of the PV system, where a discrete model is used for the Plant with a sample time of 2.56µs. The model is composed by the power and control subsystems shown in Figure 4.1 and using the parameters associated with the d-q control strategy shown in Table 3.3 and Table 3.4.

The vector controller block includes the synchronization algorithms and the cascaded control. The SIMULINK implementation of the cascaded control is shown in Figure 4.12b which is formed by the outer loop regulator that compares the dc bus voltage in the link capacitor with the reference which comes from the MPPT algorithm block. This control loop has been performed using a PI regulator. The inner control loop uses two PI controllers to regulate the d-q components of the line currents.

Several tests have been carried out in order to study the behaviour of the d-q control strategy applied to a grid-connected PV system. The cascaded control has been evaluated by introducing variations in the solar irradiance, changes in the MPPT of the PV generator I-V curve, and by injecting reactive power to the utility grid.

The response to a change in the MPPT of the I-V curve of the PV generator is simulated with a corresponding step from 500V to 600V (its nominal value, see Table 3.4) in the dc bus voltage reference V_{CC_ref} at 1s and keeping constant the incoming output current from the PV generator for a specific irradiance, as can be seen in Figure 4.13: the proper time evolution of the dc bus voltage is shown in green.

(a)

(b)
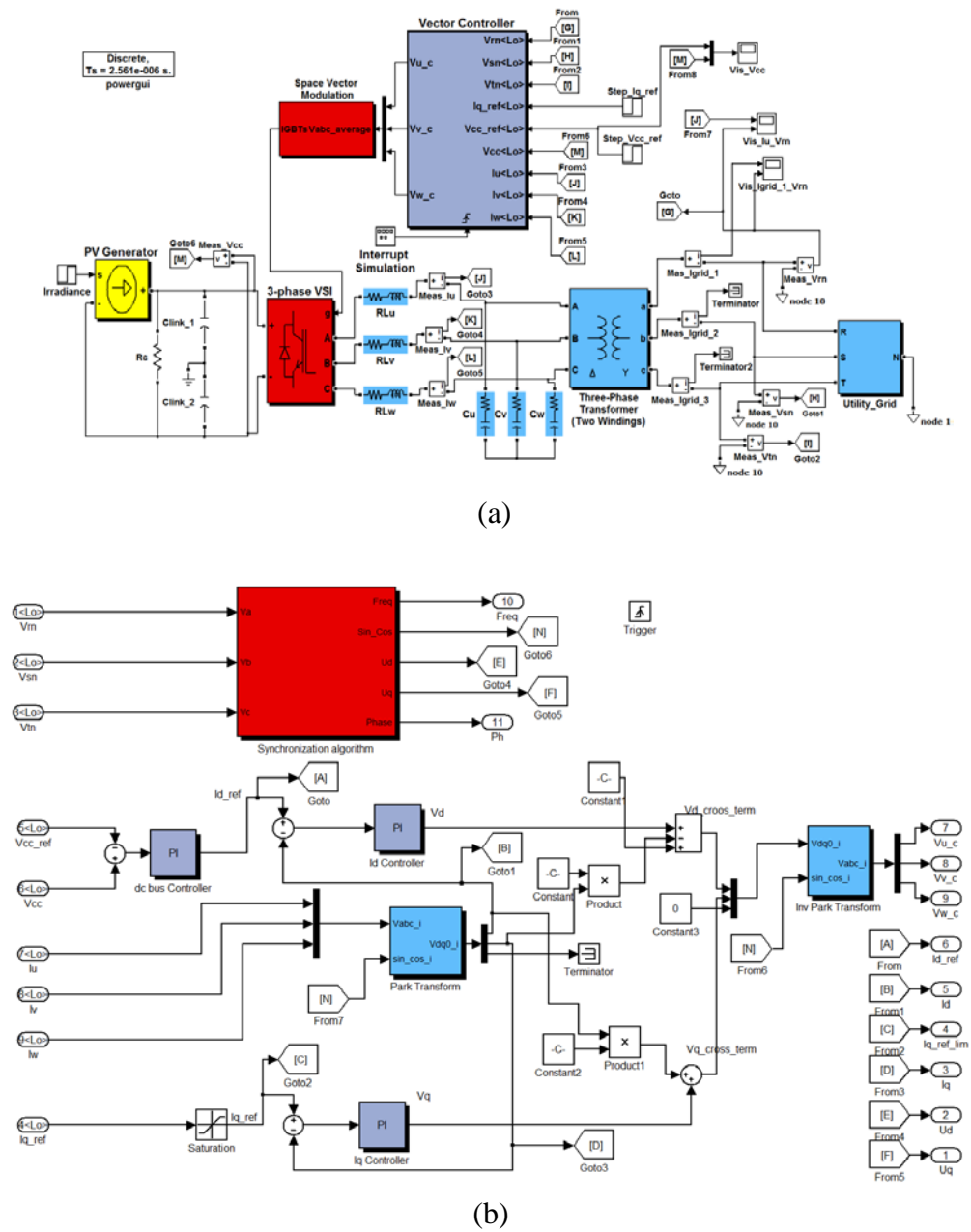
Figure 4.12. (a) SIMULINK model of the grid-connected PV system. (b) SIMULINK implementation of the cascaded control.
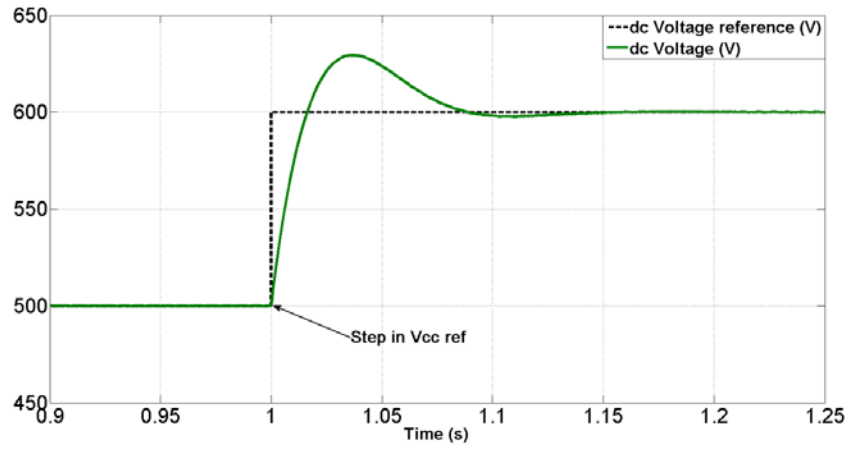
Figure 4.13. dc bus voltage during a step in V_{CC_ref} with constant output current in PV modules.

A typical situation in PV systems is a variation of the solar irradiance over the PV modules due to clouds or a sunny day: Figure 4.14a and Figure 4.14b show the time simulation of a variation in the incoming irradiance. For this, a step in the output current of the PV generator I_g is exerted at 1s from a 50% up to nominal conditions with constant dc bus voltage reference: in this case, the time evolution of the utility grid current at phase 1 is depicted in Figure 4.14a and an increasing of the current can be observed; consequently, the instantaneous active power increases from 5kW to 10kW approximately (trace in green in the Figure 4.14b).

(a)

(b)
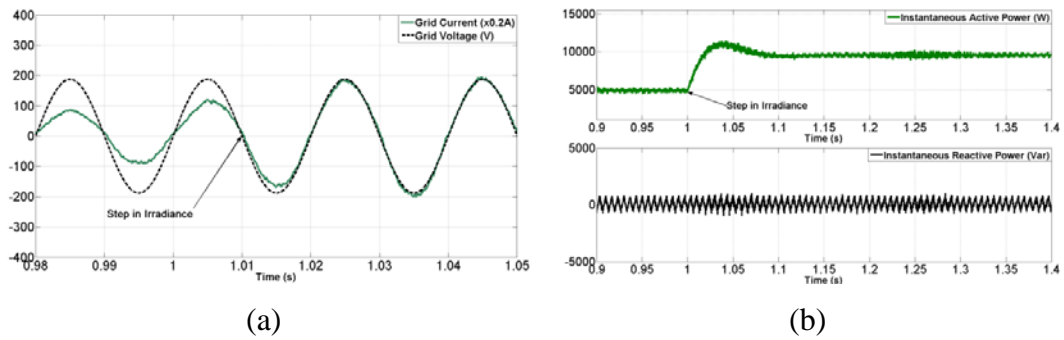
Figure 4.14. Time simulations for a step in irradiance with a constant dc bus voltage. (a) Time evolution of the utility grid voltage and current at phase 1. (b) Time evolution of the instantaneous active and reactive powers.

A time simulation of the power factor control is depicted in Figures 4.15a and 4.15b: the time evolution of the utility grid voltage and current at phase 1 is displayed in Figure 4.15a: prior 1s, the grid voltage and current are synchronized in phase and frequency for unitary power factor operation; when the step in the reference reactive power current is exerted at 1s, with constant output current at the PV Generator and the dc bus voltage, the unitary power factor operation is not achieved in this condition and the utility grid current lags the grid voltage. The step of 4.4kVar in the instantaneous reactive power can also be noticed in Figure 4.15b (trace in black), meanwhile the instantaneous active power is almost constant at 10kW (trace in green) due to the decoupled control exerted.

(a)   (b)
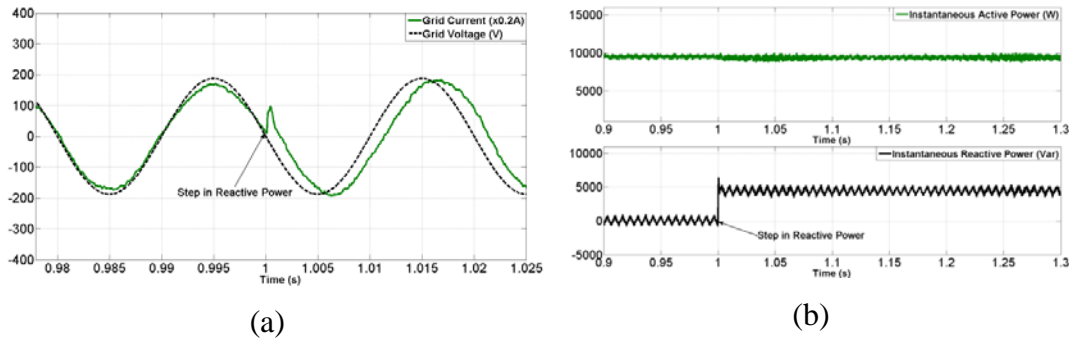
Figure 4.15. Time simulations for a step in reactive power with constant output current at the PV Generator and constant dc bus voltage. (a) Time evolution of the utility grid voltage and current at phase 1. (b) Time evolution of the instantaneous active and reactive powers.

4.4.2 PR control

Some simulations in MATLAB/SIMULINK environment are shown to validate the operation of the PV Generator grid-connected system using the parameters of the power and control subsystems shown in Table 3.3 and 3.4, respectively. Figure 4.16a shows the SIMULINK model of the system, where a discrete model is used for the Plant with a sample time of 2.56µs. The controller block includes the MSOGI-FLL synchronization algorithm and the cascaded control exerted. The SIMULINK implementation of the cascaded control used is shown in Figure 4.16b.

(a)

(b)
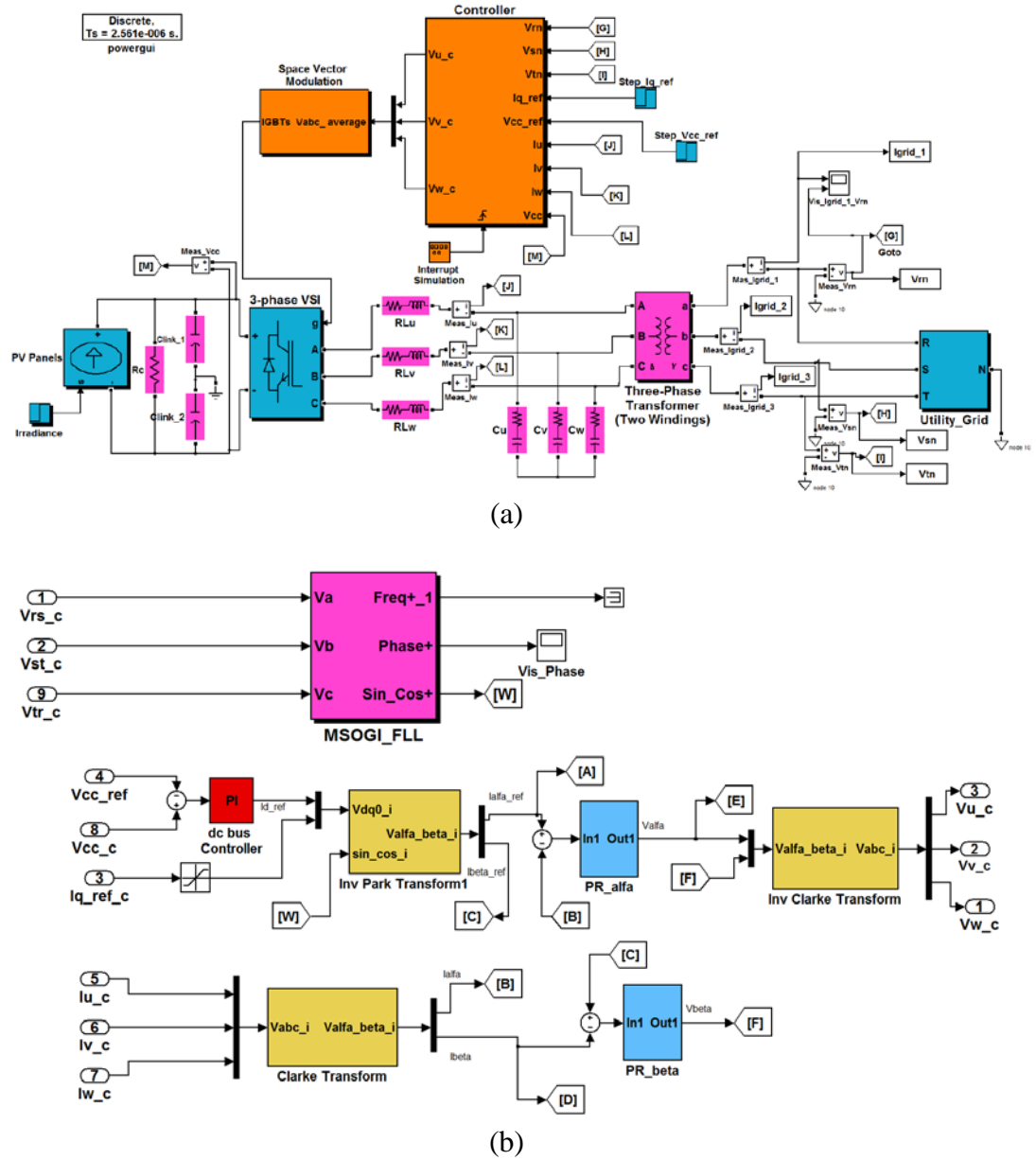
Figure 4.16. (a) SIMULINK model of the PV Generator grid-connected system. (b) SIMULINK implementation of the cascaded control.

In order to simulate the response of the 3-phase grid-connected VSI to different input conditions, some time simulations are shown in Figures 4.17, 4.18 and 4.19. The time response to a change in the MPPT of the I-V curve of the PV Generator,

is simulated with a corresponding step in the dc bus voltage reference V^*_{CC} at 1s. Holding a constant incoming output current from the PV Generator for a specific irradiance, a step from 500V to nominal value (600V) is exerted at 1s as can be seen in Figure 4.17: the proper time response of the dc bus voltage regulator is shown in blue.
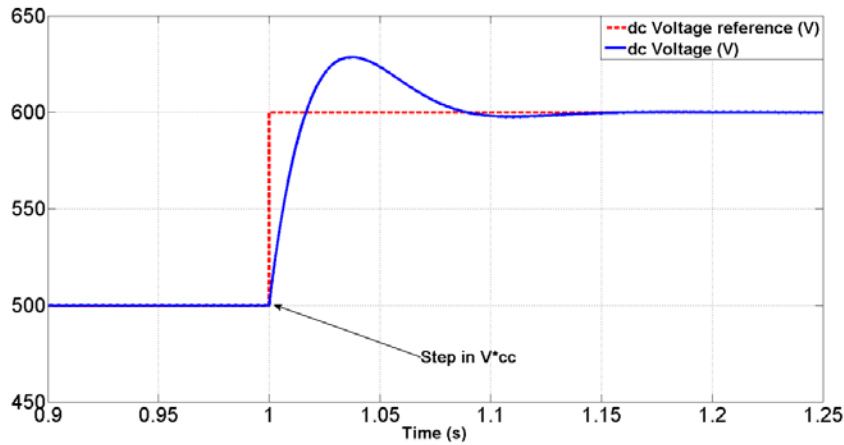
Figure 4.17. Time evolution of the dc bus voltage for a step in V^*_{CC} with constant output current in PV Generator.

Figure 4.18 shows the time simulation of a variation in the incoming irradiance. For this, a step in the output current of the PV Generator is exerted at 1s from a 50% up to nominal conditions with constant dc bus voltage reference (V^*_{CC}): in this case, the time evolution of the utility grid voltage and current at phase 1 is depicted at left side, meanwhile the instantaneous active power increases from 5kW to 10kW (trace in red), as it is shown at the right side of the Figure 4.18, and the instantaneous reactive power is almost constant (trace in blue).

An important aspect in grid-connected renewable agents is to select a suitable power factor according to the grid demand (active or reactive power) [80]. For this, a time simulation of the power factor control is depicted in Figure 4.19: the time evolution of the utility grid voltage and current at phase 1 is displayed at left side. Prior 1s, the grid voltage and current are synchronized in phase and

frequency for unitary power factor operation; a drop step in the reference reactive power current is exerted at 1s, with constant output current at the PV Generator and the dc bus voltage, and the unitary power factor operation is not achieved in this condition (the utility grid current lags the grid voltage).

(a)   (b)
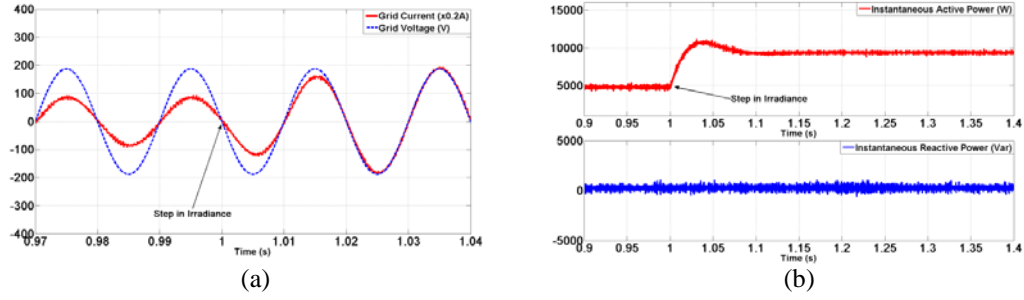
Figure 4.18. Time simulations for a step in irradiance with a constant dc bus voltage. (a) Time evolution of the utility grid voltage and current at phase 1. (b) Time evolution of the instantaneous active and reactive powers.

(a)   (b)
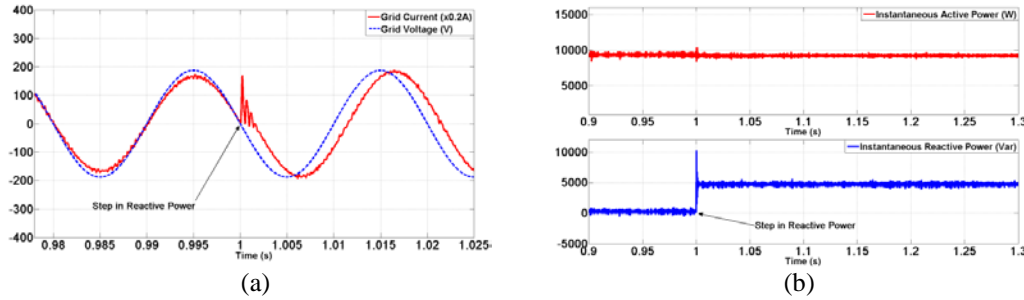
Figure 4.19. Time simulations for a step in reactive power with constant output current at the PV Generator and constant dc bus voltage. (a) Time evolution of the utility grid voltage and current at phase 1. (b) Time evolution of the instantaneous active and reactive powers.

It can be observed the response of the power subsystem with the corresponding step of 4.4kVar in the instantaneous reactive power at the right side of the Figure (trace in blue), meanwhile the instantaneous active power is almost constant around 10kW (trace in red) due to the decoupled control exerted. The resonance effect of the PR controllers can be noticed when the step in reactive power is exerted at 1s as can be observed in Figure 4.19a.

87

4.4.3 HC structure

Some simulations in MATLAB/SIMULINK environment are carry out to show the operation and the advantage of the harmonic-compensator structure when the utility grid is affected by low-order harmonic pollution. The SIMULINK model has been created from the block diagrams shown in Figure 4.8 and 4.9 and using the parameters of Table 3.3 and 3.4.

In Figure 4.20, the 5th and 7th harmonics are introduced in the 3-phase utility grid voltage with a distortion in its amplitude of 50% for both. In Figure 4.20a no harmonic compensation is performed, and then, the time evolution of the utility grid current at phase 1 is distorted due to the harmonic pollution. On the other hand, the time evolution of the grid current at phase 1 is shown in Figure 4.20b when the harmonic compensator structure shown in Figure 4.8 is used. For the latter, a perfect sine-wave grid current without harmonic pollution is observed.

(a)	(b)
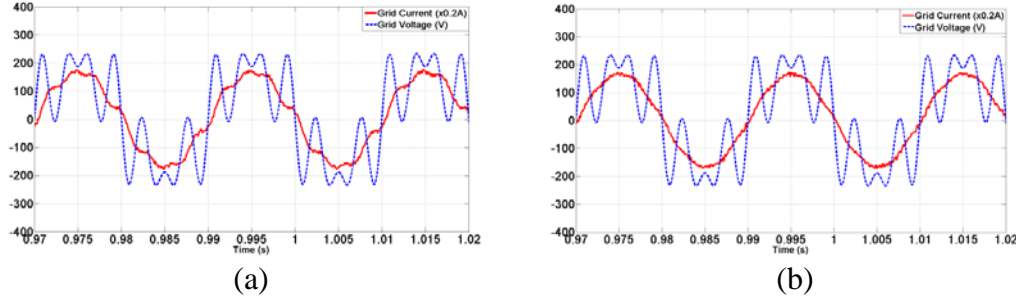
Figure 4.20. Utility grid voltage and current at phase 1. The grid voltage is distorted in amplitude by 50% for the 5th and 7th harmonics. (a) No Harmonic compensation. (b) Harmonic compensation.

4.5 Real-Time Digital Simulations

In order to support the results obtained with simulations, a series of real-time digital simulations have been carried out using the configuration of the real time platform shown in Figures 1.10 and 1.11.

4.5.1 d-q control

The real-time digital test is focused in the response of the control algorithm under different perturbations coming from the PV modules. Also a step of reactive power is exerted in order to evaluate the capability of the d-q control strategy to deal with this type of disturbances.

The real-time response of the control to a change in the MPPT of the I-V curve of the PV generator is simulated with a corresponding step from 500V to 600V (its nominal value) in the dc bus voltage reference V^*_{CC} and keeping constant the incoming output current from the PV generator for a specific irradiance, as can be seen in Figure 4.21a: the proper real-time evolution of the dc bus voltage is attained. A common situation in PV systems is a variation of the solar irradiance over the PV modules and for this, a step in the output current of the PV generator I_g is exerted from a 50% up to nominal conditions with constant dc bus voltage reference; consequently, the instantaneous active power increases from 5kW to 10kW approximately as can be observed in Figure 4.21b where the real-time evolution of the instantaneous active power is shown.

Figure 4.22a shows the real-time evolution of the instantaneous active and reactive powers injected to the 3-phase utility grid when a step of 4.4kVar is exerted. In this case, the instantaneous active power is almost constant around 10kW at steady state, due to the decoupled control exerted. The real-time evolution of the voltage and grid current at phase 1 is shown in Figure 4.22b for the same situation: after the reactive step there is a lag of the current yielding a decrement of the power factor of the inverter-grid connection from 1 to 0.92.

(a)   (b)
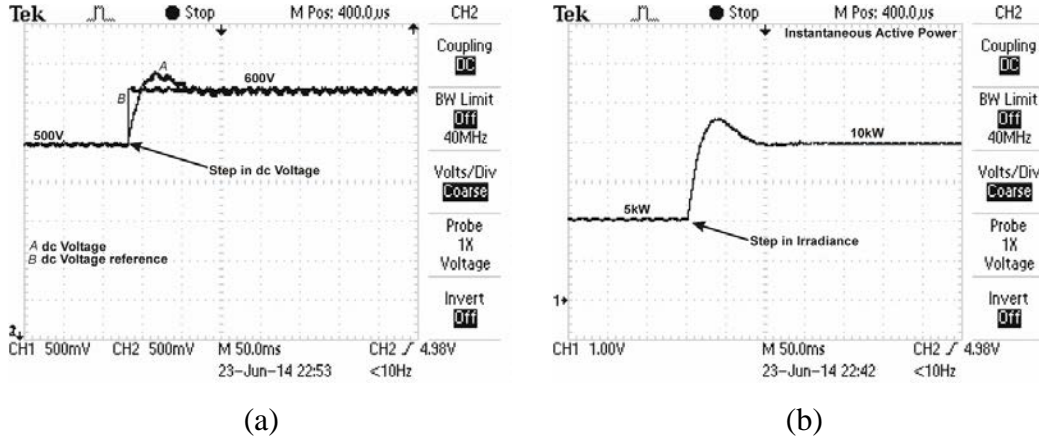
Figure 4.21. (a) dc voltage bus when a step in V^*_{CC} from 500V to 600V occur. (b) Instantaneous Active power during step of irradiance from 50% to nominal conditions.

(a)   (b)
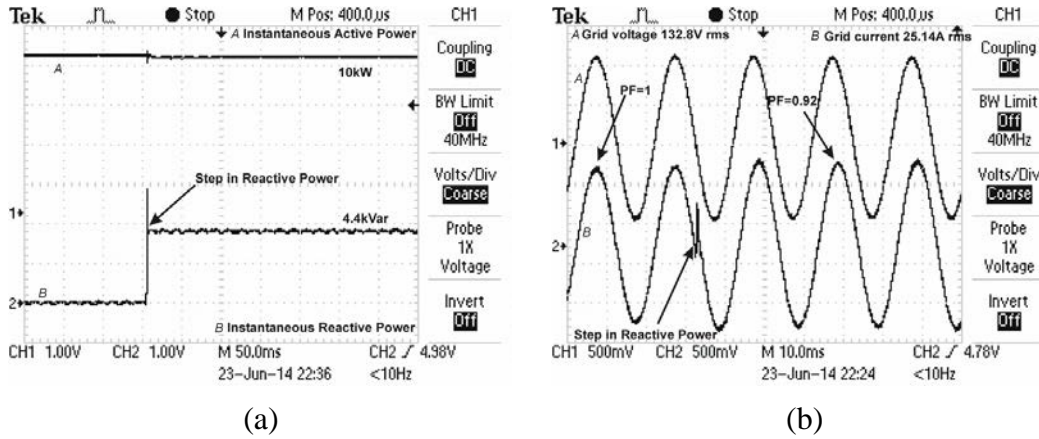
Figure 4.22. (a) Real-time evolution of the instantaneous active and reactive powers during a step in reactive power. (b) Real-time evolution of the voltage and grid current at phase 1.

4.5.2 PR control

Figure 4.23a shows the real-time evolution of dc bus voltage when a step in the reference V^*_{CC} from 500V to 600V is exerted, showing a good dynamic response of the outer dc bus regulator loop. The real-time behavior of the instantaneous active power during a variation in the incoming irradiance from a 50% to nominal conditions with constant dc bus voltage is shown in Figure 4.23b: in this case, the instantaneous active power increases from 5kW to 10kW approximately.

Figure 4.24a depicts the real-time evolution of the instantaneous active and reactive powers at steady state, injecting 10kW and 4.4kVar into the 3-phase utility grid, respectively. In addition, the real-time evolution of the voltage and grid current at phase 1 is shown in Figure 4.24b for the same situation: after the reactive step there is a lag of the current yielding a decrement of the power factor of the inverter-grid connection from 1 to 0.92.
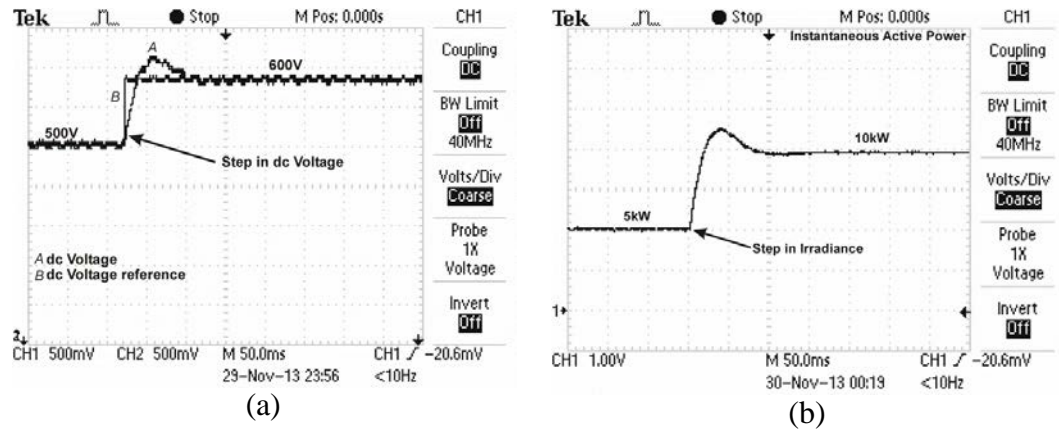
Figure 4.23. (a) dc voltage bus when a step in V^*_{CC} from 500V to 600V occur. (b) Instantaneous Active power during step of irradiance from 50% to nominal conditions.
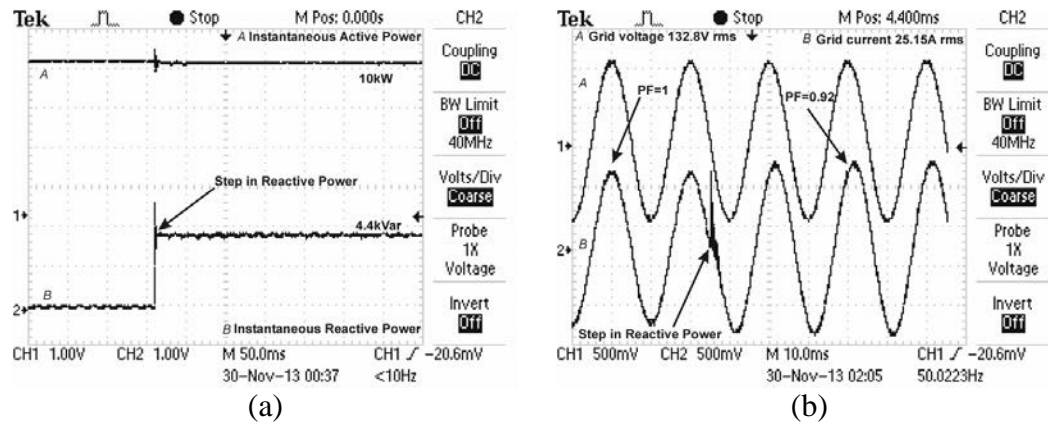
Figure 4.24. (a) Real-time evolution of the instantaneous active and reactive powers during a step in reactive power. (b) Real-time evolution of the voltage and grid current at phase 1.

91

4.5.3 HC structure

Figure 4.25a displays the real-time evolution of the utility grid voltage and current at phase 1: the 3-phase utility grid voltages are affected by 50% pollution in the magnitude of the low-order 5th and 7th harmonics, and no harmonic compensator is used. The frequency spectrum of the grid current at phase 1 is displayed in Figure 4.25b, where the fundamental component has a gain of 62dB, meanwhile the 5th and 7th harmonics have 39dB (7.94% pollution in the amplitude) and 41dB (11.22% pollution in the amplitude), respectively. In this case, the Total Harmonic Distortion (THD) is 13.64%.

(a)   (b)
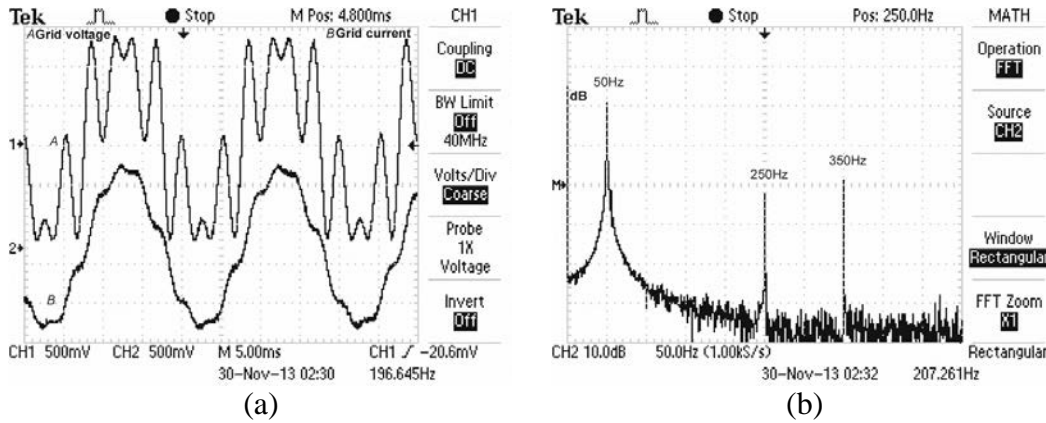
Figure 4.25. (a) Real-time evolution of the grid voltage (with a 50% pollution in the magnitude of the 5th and 7th harmonics) and current at phase 1. No harmonic compensator is used. (b) Frequency spectrum of the grid current at phase 1.

On the contrary, Figure 4.26a displays the real-time evolution of the utility grid voltage (affected by the same 50% pollution in the magnitude of the low order 5th and 7th harmonics) and current at phase 1, but a harmonic compensation is performed. The frequency spectrum of the utility grid current at phase 1 is shown in Figure 4.26b: the fundamental frequency of the current at phase 1 (50Hz) has a magnitude of 62dB, and the 5th and 7th harmonics have a magnitude of 28dB (2.51% pollution in the amplitude) and 32dB (3.97% pollution in the amplitude), respectively, yielding a THD=4.69%. In this case, it must be pointed out that an

important attenuation of the harmonic contamination is attained when using the harmonic compensator.

(a)	(b)
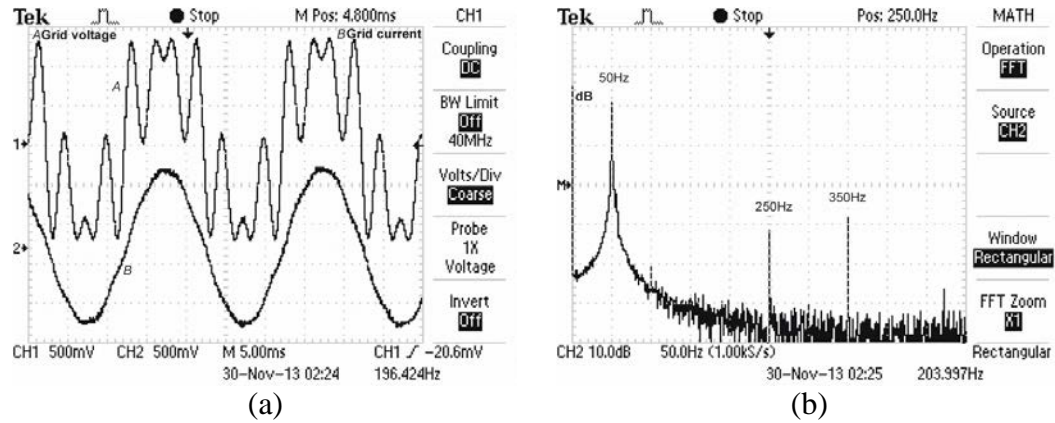
Figure 4.26. (a) Real-time evolution of the grid voltage (with a 50% pollution in the magnitude of the 5th and 7th harmonics) and current at phase 1. A Harmonic compensator structure is used. (b) Frequency spectrum of the grid current at phase 1.

A summary of the distortions in the amplitude of 5th and 7th harmonics in the grid current at phase 1, the total harmonic distortion, as well as the comparison with the normative [38] is shown in Table 4.1.

Table 4.1. Harmonic Distortions of the grid current at phase 1.

Odd harmonics	Grid Current Distortion (not using Harmonic Compensator)	Distortion using Harmonic Compensator	Distortion limit
5th	7.94%	2.51%	< 4.0%
7th	11.22%	3.97%	< 4.0%
	THD$_I$	THD$_I$	THD$_I$ limit
	13.64%	4.69%	< 5.0%

4.6 Conclusions

In this Chapter, two control strategies have been analyzed; one of them is the d-q control that uses PI regulators in the inner control loop, the other one is the PR control where PR regulators are used in the inner control loop. After a major

study, it can be said that if there are not disturbances in the utility grid a similar behaviour of response for both strategies has been observed. In the case of the PR control strategy it must be pointed out that for a very short period of time an oscillatory behaviour appears in the grid current when a step of reactive power is exerted due to the use of resonant filters in the inner control loop.

The remarkable difference between the two control strategies is that the PR controller provides a greater facility for carrying out the harmonic compensation process by cascading multiple Genaralized Integrators (GI) which are tunned to resonate at specific low order frequencies, as an easy extension of the PR structure.

CHAPTER 5
The Adaptive-Frequency Resonant Harmonic-Compensator

In this Chapter, an adaptive-frequency harmonic-compensation structure for a Voltage Source Inverter used in a 3-phase grid-connected Photovoltaic system is presented. The main purpose is to show the frequency adaptation of the used control algorithm in order to improve the compensation of the low-order utility grid current harmonics when frequency variations occur, which can be seen as an outstanding feature when comparing to conventional non-adaptive harmonic-compensator structures, and can be used in any country regardless its nominal frequency and maintaining its harmonic compensation capability without making any change in the control algorithm.

The frequency spectrum of the utility grid current is analyzed for three different scenarios: Proportional Resonant Controller without harmonic compensation, Proportional Resonant Controller with harmonic compensation, and adaptive-frequency Proportional Resonant Controller with harmonic compensation; a comparison with the normative of its individual and total harmonic amplitude distortions is carried out for the three situations.

5.1 Adaptive-Frequency Resonant Harmonic-Compensator structure

Several HC structures have been proposed in the scientific literature [76-79], and a remarkable and interesting one is found in [79], where the control of the 3-phase currents and the harmonic compensation is exerted in the Stationary Reference frame (abc->αβ transformation needed) [45]. This structure has been demonstrated as a reliable solution when harmonics distortions perturb the utility grid [33,74,81]. The HC structure proposed in [79] uses a Proportional-Resonant (PR) controller which is pre-designed to resonate at the fundamental frequency; so when frequency variations occur the operation of the PR controller could be affected. To overcome this issue, an adaptive-frequency PR controller is proposed in [82], in which a Phase-Locked Loop (PLL) is used to estimate the frequency of the 3-phase utility grid voltage. Nevertheless, when the low-voltage 3-phase utility grid is contaminated with harmonics and voltage unbalances, a classical PLL is not capable to estimate properly the frequency of the utility grid [54] and an improved strategy, such as proposed in [54,83], is necessary in order to fulfill the power quality standards [38,39,84].

When a variation of the nominal angular frequency occurs in the 3-phase utility grid voltages, the HC structure shown in Figure 5.1a will not operate properly, unless the measured angular frequency ω and its corresponding low-order harmonics were fed back to the transfer functions described by Eqs. 4.3 and 4.4, respectively, as can be seen in Figure 5.1b, yielding the adaptive-frequency PR+HC structure for the 5th and 7th harmonics, which can be extended to other low-order harmonics by extrapolation.
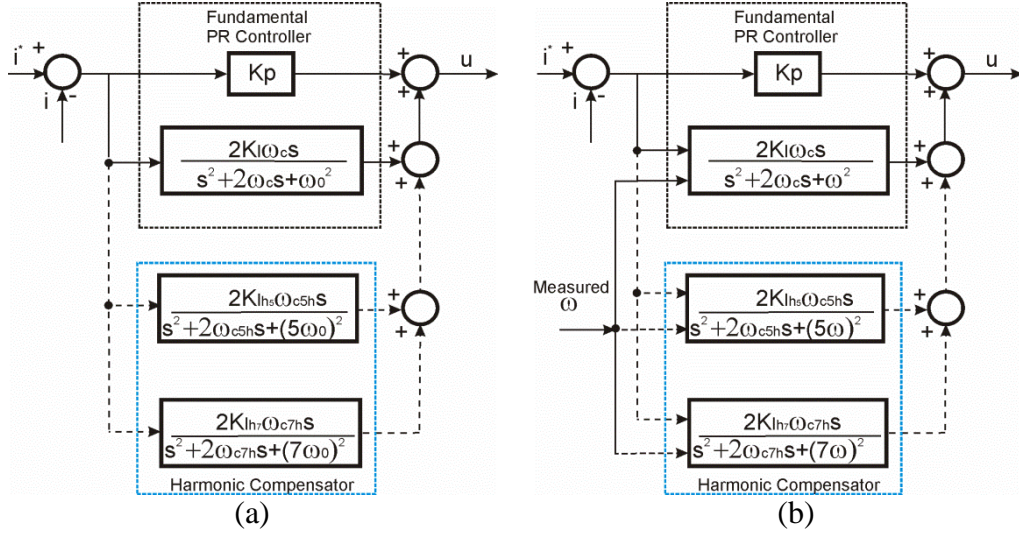
Figure 5.1. (a) PR Controller + Harmonic Compensator structure. (b) Adaptive-frequency PR Controller + Harmonic Compensator structure.

The adaptive-frequency of the HC structure described in Eq. 4.4 will be discretized with Tustin method ($s = \dfrac{2}{T_s}\dfrac{1-z^{-1}}{1+z^{-1}}$) for low-order harmonics, and considering very slow variation for the angular frequency ω. So, the transfer function in Z-domain can be stated as follows:

$$G_h(z) = \frac{Y(z)}{X(z)} = \frac{K_{ih}T_s\omega_{ch}(1-z^{-2})}{1 - 2z^{-1} + z^{-2} + \omega_{ch}T_s(1-z^{-2}) + \left(\dfrac{h\omega T_s}{2}\right)^2\left(1 + 2z^{-1} + z^{-2}\right)} \qquad \text{(Eq. 5.1)}$$

Applying inverse Z transform and considering zero initial conditions, the difference equation of the HC can be stated as follows:

$$y(n) = K_1\,y(n-1) - K_2\,y(n-2) + K_3 x(n) - K_3 x(n-2) \qquad \text{(Eq. 5.2)}$$

where:

$$K_1 = \frac{2\left[1 - \left(\dfrac{h\omega T_s}{2}\right)^2\right]}{1 + T_s\omega_{ch} + \left(\dfrac{h\omega T_s}{2}\right)^2} \ , \ K_2 = \frac{1 - T_s\omega_{ch} + \left(\dfrac{h\omega T_s}{2}\right)^2}{1 + T_s\omega_{ch} + \left(\dfrac{h\omega T_s}{2}\right)^2} \ \text{and} \ K_3 = \frac{K_{ih}T_s\omega_{ch}}{1 + T_s\omega_{ch} + \left(\dfrac{h\omega T_s}{2}\right)^2}$$

As can be seen, K_1, K_2, and K_3 will be a function, in addition to the sampling period T_s, the cutoff frequency ω_{ch} and the integral gain K_{ih}, of the measured angular frequency and its harmonics ($h\omega$), making the HC structure insensitive to frequency variations.

The block diagram (also known as simulation diagram) for the implementation of the difference equation described by Eq. 5.2 is depicted in Figure 5.2, in which the adaptive K_1, K_2, and K_3 gains are highlighted.
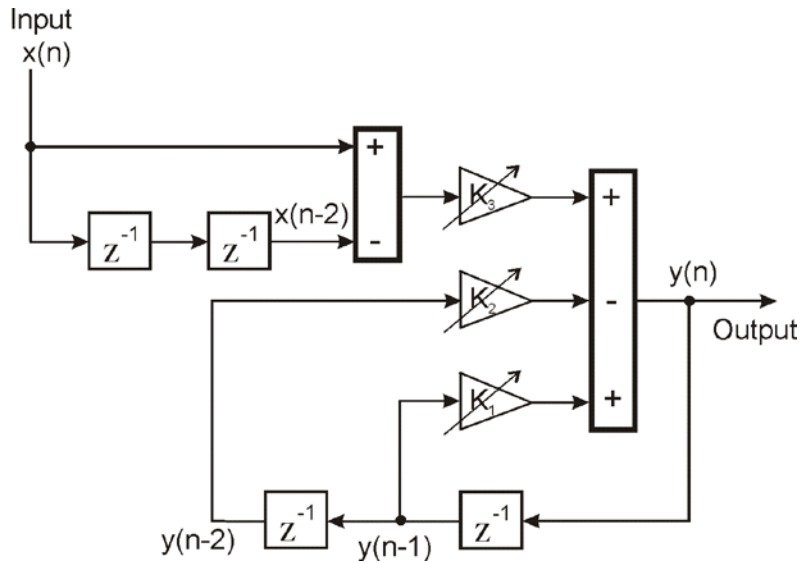
Figure 5.2. Block diagram of the discrete HC described by Eq. 5.2.

Figure 5.3 shows the grid-connected configuration for a PV renewable agent where the adaptive-frequency harmonic-compensator is used. It can be observed the use of the angular frequency from the synchronization algorithm in the

fundamental and the harmonic-compensator resonant filters in order to obtain an adaptive- frequency control.
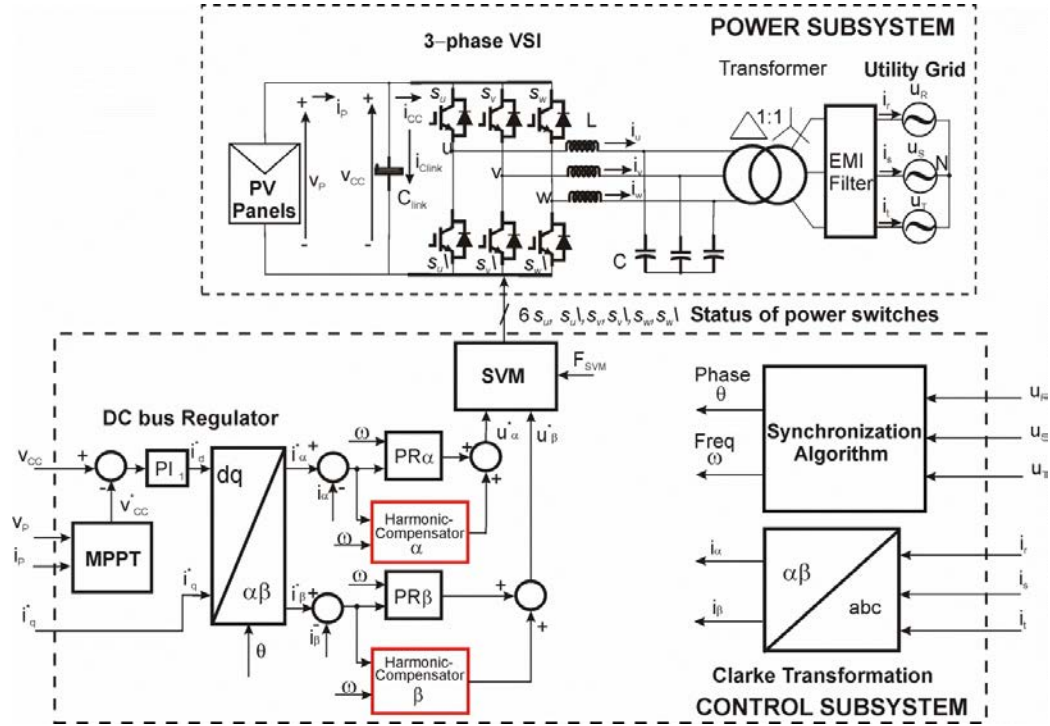
Figure 5.3. Block diagram of the Power and Control Subsystems for the 3-phase grid-connected PV system using an adaptive-frequency PR controller plus an adaptive-frequency HC structure.

Figure 5.4 depicts the open loop Bode for nominal frequencies f_0 of 50Hz and 60Hz, and its corresponding harmonic components as an example of the frequency adaptation procedure. It must be pointed out that in both cases, $PM_I=63.5^o$ and the crossover frequency $f_{cI}=1220.8Hz$ are set, producing the same dynamic response and guaranteeing the stability limits because of the adaptive-frequency achieved.
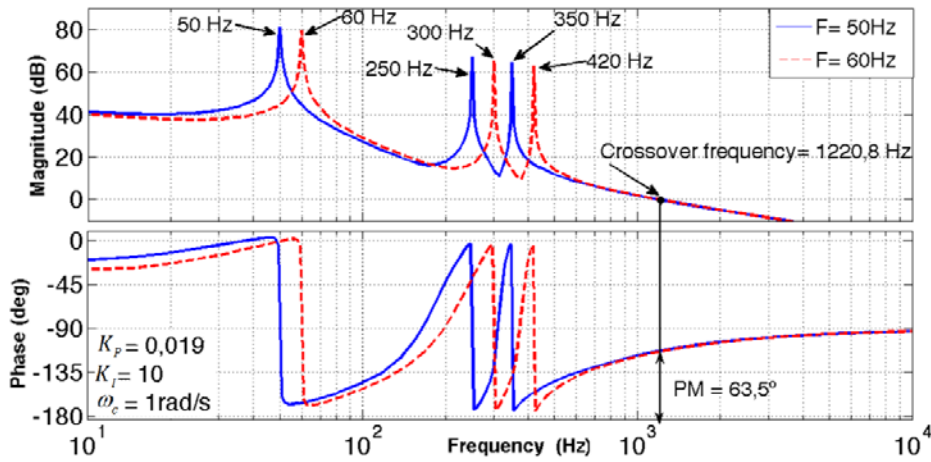
Figure 5.4. Open loop Bode plot of the PR Harmonic Compensator + Plant for 50Hz and 60Hz, respectively**.**

5.2 Simulations

In order to evaluate the adaptive-frequency control algorithm some simulations have been performed using a MATLAB/SIMULINK [10] model of the grid-connected PV system shown in Figure 5.3. The Power Subsystem is update at $Ts_{\_Plant}$=2.56μs, meanwhile the control subsystem is updated at $Ts_{\_Controller}$= 20.478μs, and is modeled inside a Triggered Subsystem which is driven by a signal emulating an Interrupt Request in the microcontroller. Analog PWM is used with a switching frequency F_{PWM}=12.208 kHz = F_{SVM}.

The 5th and 7th harmonics are introduced in to the 3-phase utility grid voltages with an amplitude distortion of 25% for both harmonics as can be observed in Figure 5.5a.

The response to a change in the MPPT of the I-V curve of the PV generator is simulated with a corresponding step at 0.6s from 500V to 600V in the dc bus voltage reference V_{CC_ref}. In this, the incoming output current from the PV generator is kept constant for a specific irradiance and the proper time evolution of the dc bus voltage is shown in blue as depicted in Figure 5.5b.
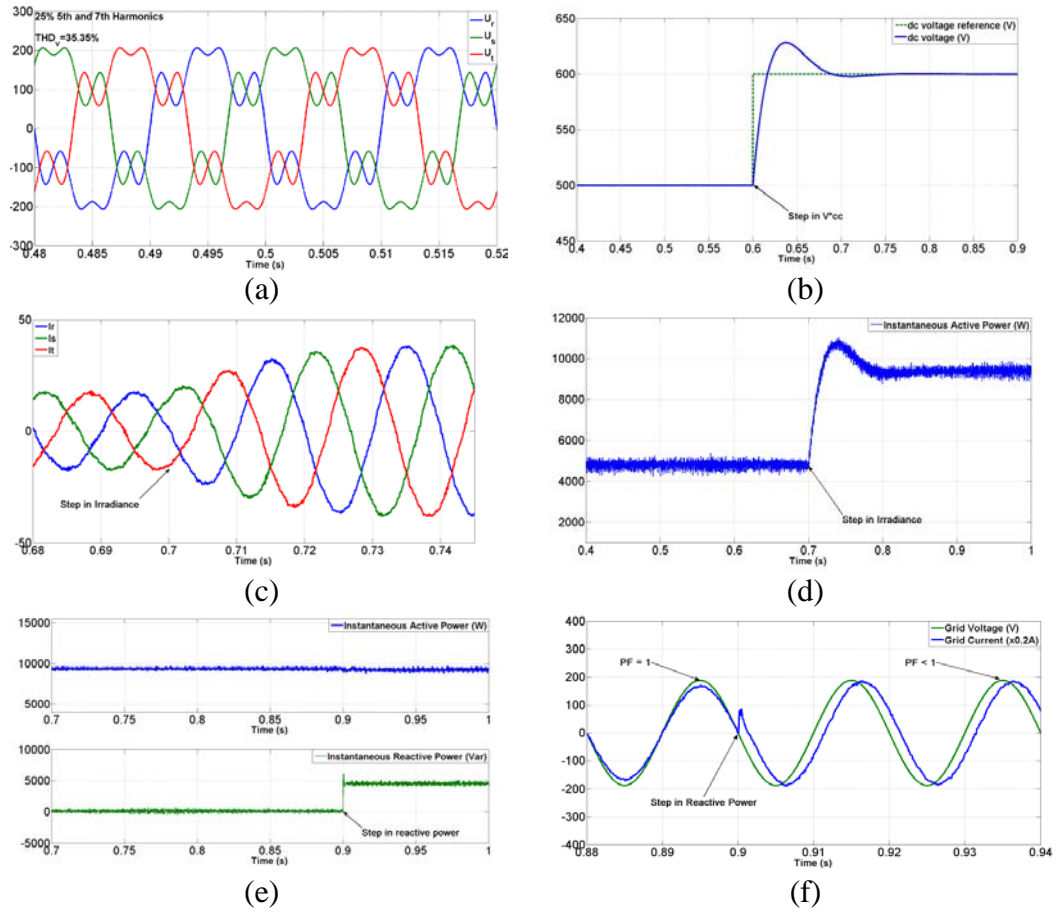
Figure 5.5. Evaluation the adaptive-frequency control algorithm. (a) Utility grid voltages (V_r=187.79 = Vpeak V_s = V_t) affected with 25% pollution in magnitude of the 5th and 7th harmonics. (b) dc bus voltage during a step in VCC_ref with constant output current in PV modules. (c) Grid currents; step in irradiance with constant reference in dc bus voltage. (d) Increasing of the instantaneous active power delivered to the 3-phase utility grid due to a step in irradiance. (e) Instantaneous active and reactive powers when a step in reactive power is exerted (constant output current in PV generator and constant reference in dc bus voltage). (f) Time evolution of the utility grid voltage and current at phase 1.

A typical situation in PV systems is a variation of the solar irradiance over the PV modules due to clouds or a sunny day: Figure 5.5c and Figure 5.5d show the time simulation of the 3-phase grid currents and the instantaneous active power according the variation in the incoming irradiance. For this, a step in the output current of the PV generator I_g is exerted at 0.7s from a 50% up to nominal conditions with constant dc bus voltage reference.

A time simulation of the power factor control is depicted in Figures 5.5e and 5.5f (the harmonics have been removed in order to have a better observation of the response of the decoupled control): a step of 4.4kVar in the instantaneous reactive power can also be noticed in Figure 5.5e (trace in green), meanwhile the instantaneous active power is almost constant at 10kW (trace in blue) due to the decoupled control exerted.

The time evolution of the utility grid voltage and current at phase 1 is displayed in Figure 5.5f: prior 0.9s, the grid voltage and current are synchronized in phase and frequency for unitary power factor operation; when the step in the reference reactive power current is exerted at 0.9s, with constant output current at the PV Generator and the dc bus voltage, the unitary power factor operation is not achieved in this condition and the utility grid current lags the grid voltage.

For the next simulations, the 5th and 7th harmonics are present in the 3-phase utility grid voltages with an amplitude distortion of 25% for both harmonics. In addition, a step of frequency from 50Hz to 60Hz is exerted in order to analyze the behaviour of the adaptive-frequency harmonic-compensator structure.

The frequency and phase detection by the synchronization algorithm is shown in Figure 5.6a: when a step of frequency of 50Hz to 60Hz is exerted at 1s, a proper frequency and phase detection can be observed in spite of the presence of high harmonic pollution in the utility grid voltages. Consequently, the synchronization of the voltage and current at phase 1 is perfectly attained as shown in Figure 5.6b, producing a unitary power factor operation before and after the step of frequency.

<div align="center">(a)   (b)</div>
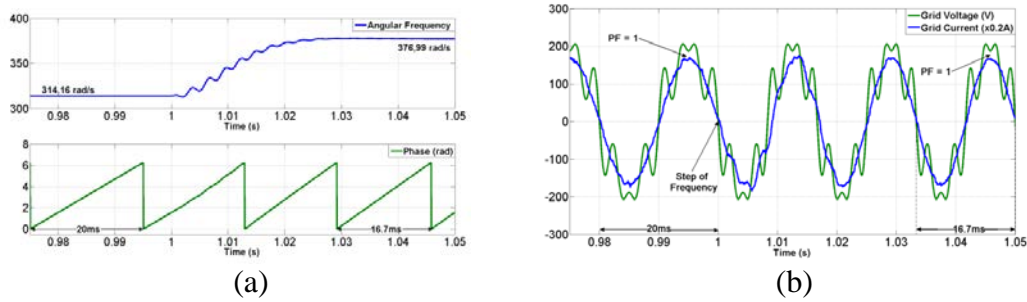
Figure 5.6. (a) Time evolution of the detected frequency and phase when a step of frequency is exerted. (b) Voltage and current at phase 1 during a step of the nominal frequency.

Figure 5.7 shows several simulations of the utility grid current at phase 1 when 5th and 7th harmonics are present in the 3-phase utility grid voltages with an amplitude distortion of 25% for both, and a frequency variation from 50Hz to 60Hz is exerted as depicted in Figure 5.7a. In order to evaluate qualitatively the distortion of the 3-phase grid currents, three scenarios are studied:

1. PR controller with no harmonic compensation

    Figure 5.7b shows the time evolution of the utility grid current at phase 1(trace in green) and it can be observed the high distortion before and after the step of frequency.

2. PR controller with harmonic compensation

    Figure 5.7c shows the time evolution of the grid current at phase 1 (trace in red): an important harmonic attenuation can be observed prior the step of frequency is exerted, but the harmonic attenuation is not obtained when the utility grid frequency is 60Hz due to the filters of the HC structure have been previously designed for a frequency of 50Hz.

3. adaptive-frequency PR controller+ HC used

    By using the adaptive-frequency HC structure, a good attenuation of the grid current harmonics for both frequencies (50Hz and 60Hz) can be observed in

Figure 5.7d (trace in blue). This is due to the auto-adjusted frequency ω and its harmonics in the resonant filters of the PR controller + HC structure.
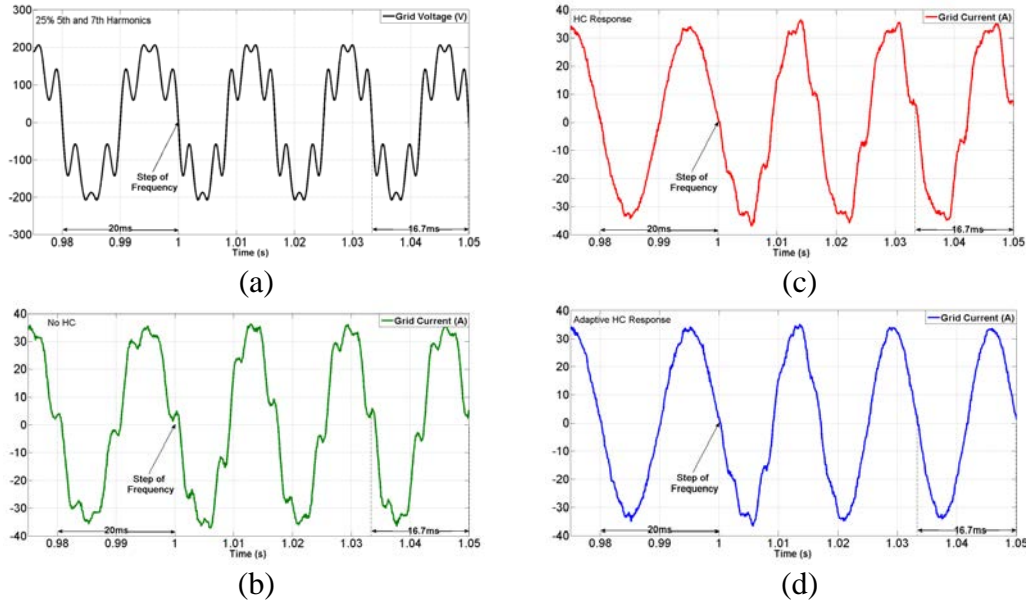
Figure 5.7. a) Grid voltage at phase 1. The grid voltage is distorted in amplitude and a variation of frequency is exerted. (b) Grid current. No Harmonic-compensator. (c) Grid current. Harmonic-compensator. (d) Grid current. Adaptive-frequency Harmonic-compensator.

5.3 Real-Time Digital Simulations

A series of real-time digital simulations have been carried out using the DS1006 DSPACE platform shown in Figure 1.1.

Following, a 25% pollution in the magnitude of the low-order 5th and 7th harmonics in the 3-phase utility grid voltages is exerted together with a step of frequency from 50Hz to 60Hz, in order to evaluate the behavior of the adaptive-frequency PR+HC structure.

Figure 5.8 shows the validation of the synchronization algorithm. The frequency detection is shown in Figure 5.8a and the time evolution of the voltage and grid current at phase 1 are depicted in Figure 5.8b: the optimal frequency detection by

this algorithm due to the use of adaptive-frequency filters for each harmonic can be seen in Figure 5.8a. No power factor degradation of the inverter-grid connection happens prior and after the step of frequency, as can be seen in Figure 5.8b, attaining a unitary power factor operation. These results validate the proper behaviour of the synchronization algorithm, as an adaptive filter for the frequency variations and when harmonic pollution is present in the utility grid voltages.

| (a) | (b) |
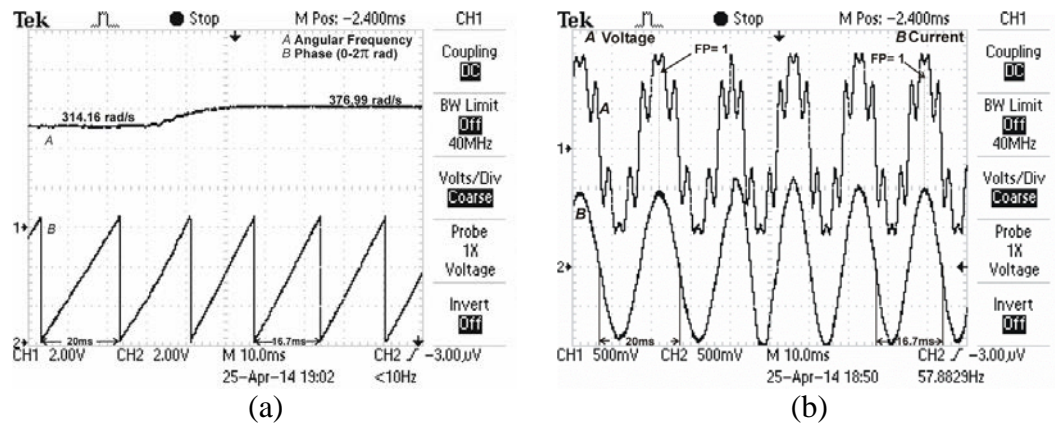
Figure 5.8. (a) Real-time frequency and phase detection by the MSOGI-FLL when a step of frequency from 50Hz to 60Hz is exerted and harmonic pollution is present in the utility grid. (b) Real-time evolution of the voltage and grid current at phase 1 when a step of frequency from 50Hz to 60Hz is exerted.

Figure 5.9, 5.10, and 5.11 displays the real-time evolution of the utility grid voltage and current at phase 1 for the same three scenarios mentioned in Section 5.2, together with its corresponding frequency spectrum for the utility grid current.

1. PR controller with no harmonic compensation: The frequency spectrum of the grid current at phase 1 (60Hz) is displayed in Figure 5.9b, where the fundamental component has a magnitude of 57dB, meanwhile the 5th and 7th harmonics have 38dB (7.94% pollution in the amplitude) and 39.5dB (9.41% pollution in the amplitude), respectively. In this case, the Total Harmonic Distortion (THD) is 12.31%.

2. PR controller with harmonic compensation: The frequency spectrum of the utility grid current at phase 1 is shown in Figure 5.10b, where the fundamental frequency of the current at phase 1 (60Hz) has a magnitude of 57dB, and the 5th and 7th harmonics have a magnitude of 36dB (6.31% pollution in the amplitude) and 35dB (5.62% pollution in the amplitude), respectively, yielding a THD=8.44%. In this case, some attenuation of the harmonic contamination is attained, but the THD of the current is still high.

3. Adaptive-frequency PR controller + HC: The frequency spectrum of the grid current at phase 1 displayed in Figure 5.11b, where the fundamental frequency of the current at phase 1 (60Hz) has a magnitude of 57dB, and an important attenuation of the harmonic contamination is attained: the 5th and 7th harmonics have a magnitude of 16dB (0.62% pollution in the amplitude) and 21dB (1.12% pollution in the amplitude), respectively, yielding to a THD=1.28%.

A summary of the distortions achieved in the amplitude of 5th and 7th harmonics in the utility grid current at phase 1, the total harmonic distortion, as well as the comparison with the normative [38] is shown in Table 5.1.

Table 5.1. Harmonic Distortions of the grid current (THD$_I$) at phase 1.

Odd harmonics	PR controller with no harmonic compensation	PR controller with harmonic compensation	Adaptive-frequency PR controller + HC	Distortion limit
5th	7.94%	6.31%	0.62%	$< 4.0\%$
7th	9.41%	5.62%	1.12%	$< 4.0\%$
	THD$_I$	THD$_I$	THD$_I$	THD$_I$ limit
	12.31%	8.44%	1.28%	$< 5.0\%$

(a)   (b)
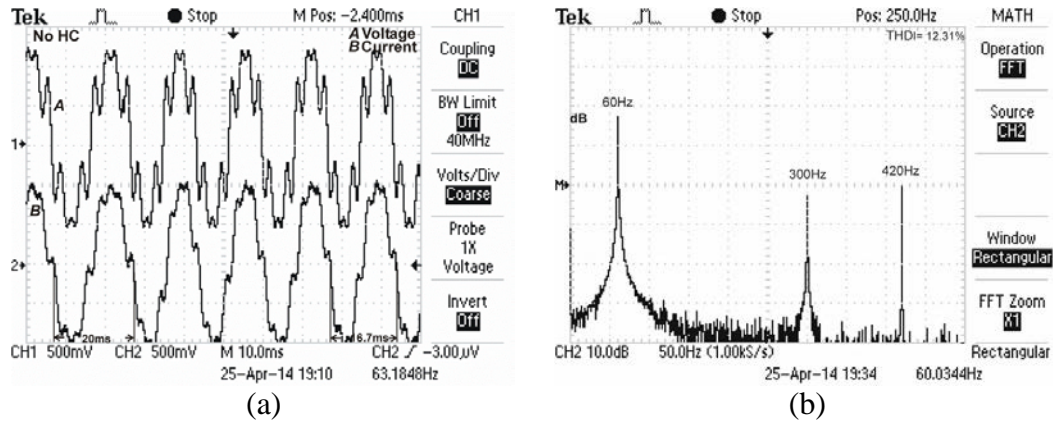
Figure 5.9. PR controller with no harmonic compensation. (a) Real-time evolution of the grid voltage and current at phase 1. (b) Frequency spectrum of the grid current at phase 1.

(a)   (b)
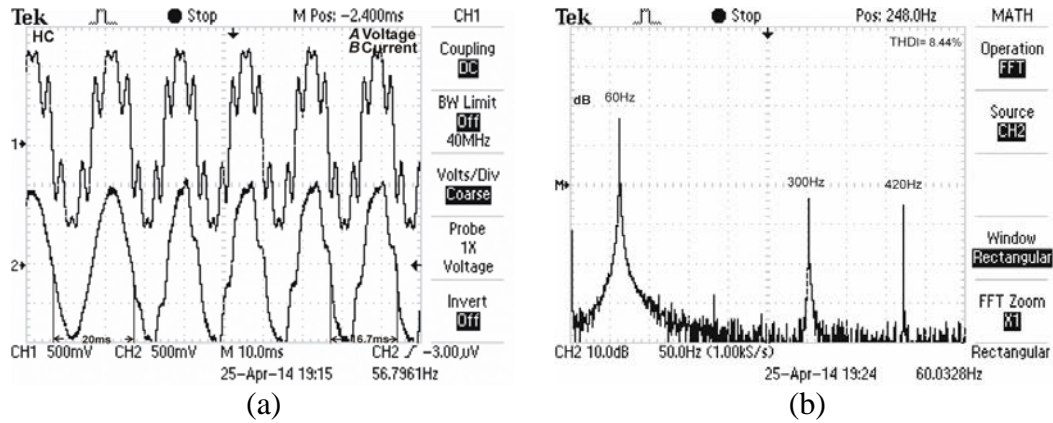
Figure 5.10. PR controller with harmonic compensation. (a) Real-time evolution of the grid voltage and current at phase 1. (b) Frequency spectrum of the grid current at phase 1.

(a)   (b)
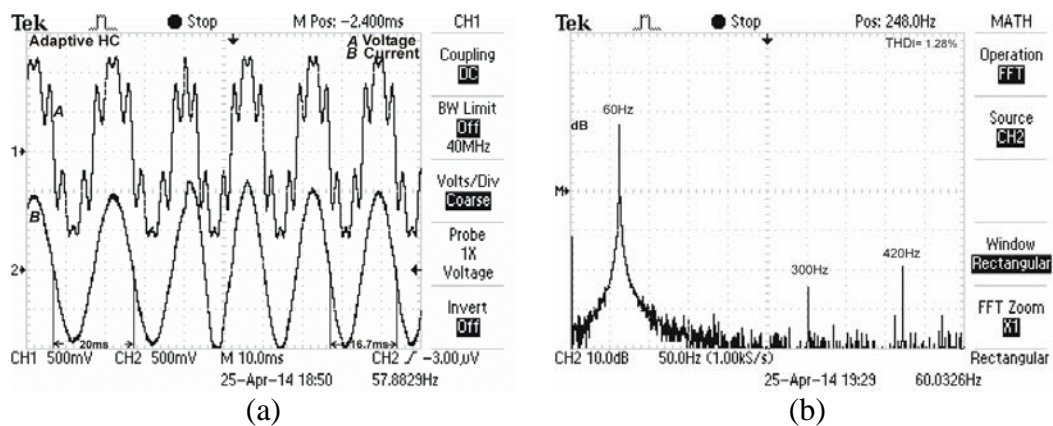
Figure 5.11. Adaptive-frequency PR controller + harmonic compensation. (a) Real-time evolution of the grid voltage and current at phase 1. (b) Frequency spectrum of the grid current at phase 1.

5.4 Conclusions

In this Chapter, an adaptive-frequency Harmonic-Compensator (HC) structure has been used to improve the quality of the grid currents of a grid-connected PV system when harmonic pollutions and frequency variations in the 3-phase utility grid voltage occur.

The reliability of the adaptive-frequency Harmonic-Compensator has been tested by introducing 25% pollution in the magnitude of the 5th and 7th harmonics of the utility grid voltages and exerting a step of frequency from 50Hz to 60Hz. It must be mentioned that, in order to obtain a good performance of the adaptive-frequency HC, a synchronization algorithm capable of accurately detecting the frequency of utility grid under any type of disturbance should be used.

The power quality level is investigated by measuring the individual and total harmonic distortions of the amplitude of the utility grid current under different Harmonic-Compensator conditions, resulting the higher level when the adaptive-frequency harmonic-compensator is used.

Finally, the adaptive-frequency Harmonic-Compensator structure is a good alternative for grid-connected Photovoltaic systems when the utility grid is under extreme conditions of disturbances and, as an extension, it can be used as a plug&play option in any country regardless its nominal frequency.

CHAPTER 6
Conclusions

In this thesis a study of several synchronization and control algorithms used in grid-connected 3-phase inverters for renewable agents was carried out in the framework of a Distributed Generation (GD) environment. Special emphasis was considered when the utility grid was affected by several disturbances, such as harmonic pollution, voltage unbalances and frequency variations.

An overview of grid-connected renewable agents was shown in Chapter 2 where the global system was divided into the power and control subsystems and its main parts were explained in order to make easier its global comprehension.

Several synchronization algorithms for grid-connected inverters were studied in Chapter 3. The performance of these algorithms was analyzed when the 3-phase utility grid voltage was affected by frequency variations, harmonic distortions and when voltage unbalances occur and a comparative summary of the strong and weak points of each one was shown. After a detailed analysis it can be said that the most complete and reliable synchronization algorithm is the MSOGI-FLL, although a sophisticated structure is necessary yielding to a higher computational burden.

In Chapter 4, two current-control strategies were analyzed: the d-q control and the PR control. Both strategies behave in a similar manner when the utility grid is not affected by any of the disturbances mentioned above. On the contrary, when low-

frequency harmonic pollution appears in the 3-phase utility grid voltages, the PR current controller together with the Harmonic-Compensator structure avoids the introduction of these harmonics in the current loop, decreasing its individual and total harmonic distortions, helping to fulfil with the international standards.

Finally, in Chapter 5 of this thesis, an adaptive-frequency HC structure was presented to improve the quality of the grid currents of a grid-connected PV system when harmonic pollutions and frequency variations occur. For this, a synchronization algorithm capable of accurately detecting the frequency of the utility grid under any type of disturbance must be used to obtain a good performance of the adaptive-frequency HC.

After several investigations, it can be concluded that the adaptive-frequency HC structure is a good alternative for grid-connected renewable systems when the utility grid is under extreme conditions of disturbances and, as an extension, it can be used as a plug&play option in any country regardless its nominal frequency. Then, the highest power quality level according to the individual and the total harmonic distortions of the amplitude of the 3-phase utility grid currents is yield, fulfilling with the international standards. This achievement is the main contribution of this thesis.

Future and Outlook

In this thesis, the main results have been validated doing real-time digital simulations, but due to technical drawbacks and the lack of financial resources, experimentation with a real platform was not possible. Nevertheless, the achieved results promise to be very robust when compared with international works in the same direction.

Special care must be taken when dealing with delay computation and the PWM sampling period in the control of grid-connected inverters. So, discrete models must be used in future works so as to be able to adjust a little bit the control parameters.

As a first step towards the final experimentation, Hardware-in-the-loop (HIL) simulation technique emerges as a promising tool for testing control algorithms in this field at a reduced cost. In addition, the utility grid perturbations can be easily performed in a real-time digital simulation platform, avoiding a real plant.

So, the following tasks are suggested for future works:

- Generation of the embedded algorithms code into a DSP or/and a FPGA in order to carry out the HIL simulation technique.
- Implementation of the control and synchronization algorithms discussed in this thesis in a real grid-connected PV system.

List of scientific contributions

JCR publications

1. N.F. Guerrero-Rodríguez and A.B. Rey-Boué, Adaptive-frequency Resonant Harmonic-Compensator structure for a 3-phase grid-connected photovoltaic system, Energy Conversion and Management, Elsevier, ISSN 0196-8904, Impact factor (WOS-JCR): 3.59 (Q1), 87 (2014) 328-337.

2. N.F. Guerrero-Rodriguez, L.C. Herrero-de Lucas, S. de Pablo-Gomez and A.B. Rey-Boué, Performance study of a synchronization algorithm for a 3-phase photovoltaic grid-connected system under harmonic distortions and unbalances, Electric Power Systems Research, Elsevier, ISSN 0378-7796, Impact factor (WOS-JCR):1.595 (Q2), 116 (2014) 252-265.

3. N.F. Guerrero-Rodríguez and A.B. Rey-Boué, Modelling, simulation and experimental verification for renewable agents connected to a distorted utility grid using a Real-Time Digital Simulation Platform, Energy Conversion and Management, Elsevier, ISSN 0196-8904, Impact factor (WOS-JCR): 3.59 (Q1), 84 (2014) 108-121.

4. N.F. Guerrero-Rodríguez, A.B. Rey-Boué, L.C. Herrero-de Lucas and Fernando Martinez, Control and Synchronization Algorithms for a Grid-Connected Renewable Agent under Harmonics distortions, Frequency

variations and Unbalances, Renewable Energy, Elsevier, ISSN 0960-1481, Impact factor (WOS-JCR): 3.361 (Q2), [Under Review].

International conference contributions

5. N.F. Guerrero-Rodríguez, A.B. Rey-Boué, A. Rigas and V. kleftakis, Review of Synchronization Algorithms used in Grid-Connected Renewable Agents, Oral Presentation at the International Conference on Renewable Energies and Power Quality (ICREPQ'14), 2014, Cordoba, Spain.

6. N.F. Guerrero-Rodríguez, A.B. Rey-Boué and S. de Pablo-Gomez, Design of the Control Algorithms for Photovoltaic Grid-Connected Renewable Agents using the Hardware-in-the-loop Simulation Technique, Oral Presentation at the International Conference on Power Systems Transients (IPST2013), 2013, Vancouver, Canada.

7. N.F. Guerrero-Rodríguez, Gino de J**.** Roa and A.B. Rey-Boué, Implementation of a vector control for grid-connected renewable agent systems, Oral Presentation at the RESOUK, 2012, Murcia, Spain.

Non-JCR publications

8. N.F. Guerrero-Rodríguez, A.B. Rey-Boué, A. Rigas and V. kleftakis, Review of Synchronization Algorithms used in Grid-Connected Renewable Agents, Renewable Energy & Power Quality Journal, ISSN 2172-038X, Paper no. 300.

Reference List

[1] Energy Information Administration (EIA), International Energy Outlook 2013. www.eia.gov/forecasts/ieo/pdf/0484(2013).pdf.

[2] European Commission, eurostat, Statiscal books. 2013. Luxembourg.

[3] A.McCrone, E.Usher, V.Sonntag-O'Brien, U.Moslener, and C.Grüning, Global Trends in Renewable Energy Investment 2012. 2012. Frankfurt School of Finance and Management, commissioned by UNEP's Division of Technology, Industry and Economics (DTIE) and endorsed by REN21.

[4] Directive 2009/28/EC on the promotion of the use of energy from renewable sources. 2009.

[5] L.Freris and D.Infield, Renewable Energy in Power Systems, John Wiley & Sons, Ltd, Publication, United Kingdom , 2008.

[6] D.McGinn et al, Renewables 2013, Global Status Report (REN21). 2013. Paris.

[7] European Photovoltaic Industry Association (EPIA) 2014. Amsterdam.

[8] J.M Martin and J.C Posadas, Central America's Electric Sector: The Path to Interconnection and a Regional Market, Journal of Energy Security, (2012).

[9] GWEC Global Wind Report, Annual Market Update 2013. Brussels.

[10] MATLAB/SIMULINK. The MathWorks, Inc. <http://www.mathworks.com/>. 2008.

[11] OPAL-RT Technologies. http://www.opal-rt.com/.

[12] TYPHOON. http://www.typhoon-hil.com/products/.

[13] DSPACE. http://www.dspace.com/en/ltd/home.cfm.

[14] M.Rakotozafy, P.Poure, S.Saadate, C.Bordas, and L.C.Leclere, Real-time digital simulation of power electronics systems with Neutral Point Piloted multilevel inverter using FPGA, Electric Power Systems Research, 81 (2011) 687-698.

[15] L.Wei, G.Joos, and J.Belanger, Real-Time Simulation of a Wind Turbine Generator Coupled With a Battery Supercapacitor Energy Storage System, IEEE Transactions on Industrial Electronics, 57 (2010) 1137-1145.

[16] A.V.Timbus, M.Liserre, R.Teodorescu, P.Rodriguez, and F.Blaabjerg, Evaluation of Current Controllers for Distributed Power Generation Systems, IEEE Transactions on Power Electronics, 24 (2009) 654-664.

[17] A.B.Rey-Boué, R.García-Valverde, F.Ruz-Vila, and J.M.Torrelo-Ponce, An integrative approach to the design methodology for 3-phase power conditioners in Photovoltaic Grid-Connected systems, Energy Conversion and Management, 56 (2012) 80-95.

[18] H.Akagi, E.Hirokazu Watanabe, and M.Aredes, Instantaneous Power Theory and Applications to Power Conditioning, John Wiley & Sons, 2007.

[19] G.Tsengenes and G.Adamidis, Investigation of the behavior of a three phase grid-connected photovoltaic system to control active and reactive power, Electric Power Systems Research, 81 (2011) 177-184.

[20] J.W.Pratt, L.E.Klebanoff, K.Munoz-Ramos, A.A.Akhil, D.B.Curgus, and B.L.Schenkman, Proton exchange membrane fuel cells for electrical power generation on-board commercial airplanes, Applied Energy, 101 (2013) 776-796.

[21] V.Boscaino, R.Miceli, and G.Capponi, MATLAB-based simulator of a 5 kW fuel cell for power electronics design, International Journal of Hydrogen Energy, 38 (2013) 7924-7934.

[22] C.Wang, M.H.Nehrir, and H.Gao, Control of PEM Fuel Cell Distributed Generation Systems, IEEE Transactions on Energy Conversion, 21 (2006) 586-595.

[23] H.Jenn-Jiang, Sustainability study of hydrogen pathways for fuel cell vehicle applications, Renewable and Sustainable Energy Reviews, 19 (2013) 220-229.

[24] F.Blaabjerg, Z.Chen, and S.B.Kjaer, Power electronics as efficient interface in dispersed power generation systems, IEEE Transactions on Power Electronics, 19 (2004) 1184-1194.

[25] M.Hashem Nehrir and C.Wang, Modeling and Control of Fuel Cells: Distributed Generation Applications, John Wiley & Sons, Inc., New Jersey, 2009.

[26] L.An, Z.H.Chai, L.Zeng, P.Tan, and T.S.Zhao, Mathematical modeling of alkaline direct ethanol fuel cells, International Journal of Hydrogen Energy, 38 (2013) 14067-14075.

[27] Y.Hou, Z.Yang, and X.Fang, An experimental study on the dynamic process of PEM fuel cell stack voltage, Renewable Energy, 36 (2011) 325-329.

[28] V.Scarpa, S.Buso, and G.Spiazzi, Low-Complexity MPPT Technique Exploiting the PV Module MPP Locus Characterization, IEEE Transactions on Industrial Electronics, 56 (2009) 1531-1538.

[29] N.Mutoh, M.Ohno, and T.Inoue, A method for MPPT control while searching for parameters corresponding to weather conditions for PV generation systems. IECON 2004. 30th Annual Conference of IEEE. 3, 3094-3099. 2-11-2004.

[30] M.Boutoubat, L.Mokrani, and M.Machmoum, Control of a wind energy conversion system equipped by a DFIG for active power generation and power quality improvement, Renewable Energy, 50 (2013) 378-386.

[31] E.Kabalci, Design and analysis of a hybrid renewable energy plant with solar and wind power, Energy Conversion and Management, 72 (2013) 51-59.

[32] F.Blaabjerg and Z.Chen, Power Electronics for Modern Wind Turbines, Morgan & Claypool, United States of America, 2006.

[33] F.Blaabjerg, R.Teodorescu, M.Liserre, and A.V.Timbus, Overview of Control and Grid Synchronization for Distributed Power Generation Systems, IEEE Transactions on Industrial Electronics, 53 (2006) 1398-1409.

117

[34] Y.Abdel-Rady, I.Mohamed, and F.El-Saadany, A Robust Natural-Frame-Based Interfacing Scheme for Grid-Connected Distributed Generation Inverters, IEEE Transactions on Energy Conversion, 26 (2011) 728-736.

[35] D.Boroyevich, I.Cvetkovic, R.Burgos, and D.Dong, Intergrid: A Future Electronic Energy Network?, IEEE Journal of Emerging and Selected Topics in Power Electronics, 1 (2013).

[36] K.Zhou and D.Wang, Relationship between space-vector modulation and three-phase carrier-based PWM: a comprehensive analysis [three-phase inverters], IEEE Transactions on Industrial Electronics, 49 (2002) 186-196.

[37] R.Ekstrom and M.Leijon, Lower order grid current harmonics for a voltage-source inverter connected to a distorted grid, Electric Power Systems Research, 106 (2014) 226-231.

[38] Recommended Practices and Requirements of Harmonic Control in Electrical Power Systems. Standard ANSI/IEEE 519-1992. 1992.

[39] Standard for Interconnecting Distributed Resources with Electric Power Systems, 2003.

[40] J.C.Hernández, J.Ortega, .De la Cruz, and D.Vera, Guidelines for the technical assessment of harmonic, flicker and unbalance emission limits for PV-distributed generation, Electric Power Systems Research, 81 (2011) 1247-1257.

[41] E.J.Bueno, F.Espinosa, F.J.Rodriguez, J.Urefi, and S.Cobrece, Current control of voltage source converters connected to the grid through an LCL-filter, Power Electronics Specialists Conference, 2004 IEEE 35th Annual, 1 (2004) 68-73.

[42] D.Hamza, Q.Mei, and P.K.Jain, Implementation of an EMI active filter in grid-tied PV micro-inverter controller and stability verification. IECON. 477-482. 25-10-2012.

[43] S.Wang, C.Xu, and H.Qin, Design theory and implementation of planar EMI filter based on annular integrated inductor-capacitor unit. Electromagnetic Compatibility (APEMC). 129-132.

[44] C.Po-Shen and L.Yen-Shin, Effective EMI Filter Design Method for Three-Phase Inverter Based Upon Software Noise Separation, IEEE Transactions on Power Electronics, 25 (2010) 2797-2806.

[45] E.Clarke, Circuit Analysis of AC Power Systems, vol. I, Wiley, 1950.

[46] R.H.Park, Two reaction theory of synchronous machines. Generalized method of analysis-Part I. Proc. Winter Convention of AIEE . 716-730. 1929.

[47] A.Ferrero and G.Superti-Furga, A New Approach to the Definition of Power Components in Three-Phase Systems Under Nonsinusoidal Conditions, IEEE Transactions on Instrumentation and Measurement, 40 (1991) 568-577.

[48] H.Akagi, Y.Kanazawa, and A.Nabae, Instantaneous Reactive Power Compensators Comprising Switching Devices without Energy Storage Components. IEEE Transactions on Industry Applications IA-20[3], 625-630. 1984.

[49] MP.Kazmierkowski, R.Krishnan, and F.Blaabjerg, Control in Power Electronics, Selected Problems, 2002.

[50] S.Buso and P.Mattavelli, Digital Control in Power Electronics, Morgan & Claypool, 2006.

[51] V.Kaura and V.Blasko, Operation of a phase locked loop system under distorted utility conditions, IEEE Transactions on Industry Applications, 33 (1997) 58-63.

[52] M.Karimi-Ghartemani and M.R.Iravani, A method for synchronization of power electronic converters in polluted and variable-frequency environments, IEEE Transactions on Power Systems, 19 (2004) 1263-1270.

[53] P.Rodriguez, R.Teodorescu, I.Candela, A.V.Timbus, M.Liserre, and F.Blaabjerg, New Positive-sequence Voltage Detector for Grid Synchronization of Power Converters under Faulty Grid Conditions. Power Electronics Specialists Conference, 2006. PESC '06. 37th IEEE. 1-7. 18-6-2006.

[54] P.Rodriguez, A.Luna, M.Ciobotaru, R.Teodorescu, and F.Blaabjerg, Multiresonant Frequency-Locked Loop for Grid Synchronization of Power

Converters Under Distorted Grid Conditions, IEEE Transactions on Industry Electronics, 58 (2011) 127-138.

[55] N.S.D'Souza, L.A.C.Lopes, and X.Liu, Comparative study of variable size perturbation and observation maximum power point trackers for PV systems, Electric Power Systems Research, 80 (2010) 296-305.

[56] R.Kadri, J.P.Gaubert, and G.Champenois, An Improved Maximum Power Point Tracking for Photovoltaic Grid-Connected Inverter Based on Voltage-Oriented Control, IEEE Transactions on Industrial Electronics, 58 (2011) 66-75.

[57] K.Ishaque and Z.Salam, A review of maximum power point tracking techniques of PV system for uniform insolation and partial shading condition, Renewable and Sustainable Energy Reviews, 19 (2013) 475-488.

[58] H.M.Farh and A.M.Eltamaly, Maximum power extraction from wind energy system based on fuzzy logic control, Electric Power Systems Research, 97 (2013) 144-150.

[59] N.F.Guerrero-Rodríguez, L.C.Herrero-de Lucas, S.de Pablo-Gómez, and A.B.Rey-Boué, Performance study of a synchronization algorithm for a 3-phasephotovoltaic grid-connected system under harmonic distortionsand unbalances, Electric Power Systems Research, 116 (2014) 252-265.

[60] R.Teodorescu, M.Liserre, and P.Rodriguez, Grid Converters for Photovoltaic and Wind Power Systems. 2011. United Kingdom, John Wiley & Sons, Ltd.

[61] P.Rodriguez, A.Luna, M.Ciobotaru, R.Teodorescu, and F.Blaabjerg, Advanced Grid Synchronization System for Power Converters under Unbalanced and Distorted Operating Conditions. IEEE Industrial Electronics, IECON. 5173-5178. 6-11-2006.

[62] P.Rodriguez, A.Luna, R.S.Muñoz-Aguilar, I.Etxeberria-Otadui, R.Teodorescu, and F.Blaabjerg, A Stationary Reference Frame Grid Synchronization System for Three-Phase Grid-Connected Power Converters Under Adverse Grid Conditions, IEEE Transactions on Industrial Electronics, 27 (2012) 99-112.

120

[63] Park RH, Two reaction theory of synchronous machines. Generalized method of analysis-Part I. Proc. Winter Convention of AIEE . 716-730. 1929.

[64] F.Ruz, A.B.Rey-Boué, J.M Torrelo, A.Nieto, and F.J.Canovas, Real time test benchmark design for photovoltaic grid-connected control systems, Electric Power Systems Research, 81 (2011) 907-914.

[65] F.D.Freijedo, J.Doval-Gandoy, O.Lopez, and E.Acha, Tuning of Phase-Locked Loops for Power Converters Under Distorted Utility Conditions, IEEE Transactions on Industry Applications, 45 (2009) 2039-2047.

[66] A.V.Timbus, M.Liserre, R.Teodorescu, and F.Blaabjerg, Synchronization methods for three phase distributed power generation systems - An overview and evaluation. Power Electronics Specialists Conference. 2474-2481. 16-6-2005.

[67] C.L.Fortescue, Method of Symmetrical Co-Ordinates Applied to the Solution of Polyphase Networks, American Institute of Electrical Engineers, XXXVII (1918) 1027-1140.

[68] Y.Xiaoming, W.Merk, H.Stemmler, and J.Allmeling, Stationary-frame generalized integrators for current control of active power filters with zero steady-state error for current harmonics of concern under unbalanced and distorted operating conditions, IEEE Transactions on Industry Applications, 38 (2002) 523-532.

[69] G.F.Franklin, J.D.Powell, and A.Emami-Naeini, Feedback Control of Dynamic Systems, Prentice-Hall,Inc., New Jersey, 2002.

[70] W.V Lyon, Applications of the method of symmetrical components, McGraw-Hill, New York, 1937.

[71] T.Ackermann, Wind Power in Power Systems , John Wiley & Sons, Ltd., England, 2005.

[72] European Committee for Electrotechnical Standardization (CENELEC), EN 50160, Voltage characteristics of electricity supplied by public distribution systems. 1999.

[73] IEEE Recommended Practice for Utility Interface of Photovoltaic (PV) Systems. IEEE Std 929-2000 . 2000.

[74] R.Teodorescu, F.Blaabjerg, M.Liserre, and PC.Loh, Proportional-resonant controllers and filters for grid-connected voltage-source converters, IEE Procedings Electric Power Applications, 153 (2006) 750-762.

[75] D.N.Zmood and D.G.Holmes, Stationary frame current regulation of PWM inverters with zero steady-state error, IEEE Transactions on Power Electronics, 18 (2003) 814-822.

[76] T.Ohnishi, M Hojo, and N.Matsui, Instantaneous line voltage controlled harmonics compensator. IECON. Industrial Electronics Society 2, 754-759. 2000.

[77] T.Ohnishi and M.Hojo, Harmonics compensator by connecting sinusoidal voltage PWM converters. Power Conversion Conference. 3, 1399-1404. 2002.

[78] P.Mattavelli, A closed-loop selective harmonic compensation for active filters, IEEE Transactions on Industry Applications, 37 (2001) 81-89.

[79] M.J.Newman, D.N.Zmood, and D.G.Holmes, Stationary frame harmonic reference generation for active filter systems, IEEE Transactions on Industry Applications, 38 (2002) 1591-1599.

[80] K.Himoura, K.Ghedamsia, and E.M.Berkoukb, Supervision and control of grid connected PV-Storage systems with the five level diode clamped inverter, Energy Conversion and Management, 77 (2014) 98-107.

[81] N.F.Guerrero-Rodríguez and A.B.Rey-Boué, Modelling, simulation and experimental verification for renewable agents connected to a distorted utility grid using a Real-Time Digital Simulation Platform, Energy Conversion and Management, 84 (2014) 108-121.

[82] A.V.Timbus, M.Ciobotaru, R.Teodorescu, and F.Blaabjerg, Adaptive resonant controller for grid connected converters in distributed power generation systems, 2006, pp. 1601-1606.

[83] M.Karimi-Ghartemani, M.Mojiri, A.Safaee, J.Age Walseth, S.Ali Khajehoddin, P.Jain, and A.Bakhshai, A New Phase-Locked Loop System for Three-Phase Applications, IEEE Transactions on Power Electronics, 28 (2013) 1208-1218.

[84] IEC 61727 Ed. 2, Photovoltaic (PV) Systems-Characteristics of the Utility Interface, 2004.